

**ELEVATED TEMPERATURE SLIDING WEAR  
BEHAVIOR OF  $\text{CoCrNiTiMo}_x$  AND  $\text{CoCrNiTiW}_x$  HIGH  
ENTROPY ALLOYS PROCESSED USING  
MECHANICAL ALLOYING AND HIGH-VELOCITY  
OXY-FUEL SPRAY**

Thesis

Submitted in partial fulfillment of the requirements for the degree of

**DOCTOR OF PHILOSOPHY**

by

**SYAM NARAYANA ADDEPALLI**



**DEPARTMENT OF MECHANICAL ENGINEERING  
NATIONAL INSTITUTE OF TECHNOLOGY KARNATAKA,  
SURATHKAL, MANGALORE – 575025**

**June, 2024**

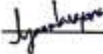


## DECLARATION

I hereby *declare* that the Research Thesis entitled "ELEVATED TEMPERATURE SLIDING WEAR BEHAVIOR OF CoCrNiTiMo<sub>x</sub> AND CoCrNiTiW<sub>x</sub> HIGH ENTROPY ALLOYS PROCESSED USING MECHANICAL ALLOYING AND HIGH-VELOCITY OXY-FUEL SPRAY" which is being submitted to the *National Institute of Technology Karnataka, Surathkal* in partial fulfilment of the requirements for the award of the Degree of *Doctor of Philosophy* in *Department of Mechanical Engineering* is a *bonafide report of the research work carried out by me*. The material contained in this Research Thesis has not been submitted to any University or Institution for the award of any degree.

Register Number: 187012ME014

Name of the Research Scholar: SYAM NARAYANA ADDEPALLI

Signature of the Research Scholar:  \_\_\_\_\_

Department of Mechanical Engineering,

Place. NITK, Surathkal

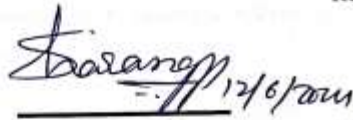
Date. 12/06/2024



## CERTIFICATE

This is to *certify* that the Research Thesis entitled “ELEVATED TEMPERATURE SLIDING WEAR BEHAVIOR OF CoCrNiTiMo<sub>x</sub> AND CoCrNiTiW<sub>x</sub> HIGH ENTROPY ALLOYS PROCESSED USING MECHANICAL ALLOYING AND HIGH-VELOCITY OXY-FUEL SPRAY” submitted by Mr. SYAM NARAYANA ADDEPALLI (Register Number. 187012ME014) as the record of the research work carried out by him, is *accepted as the Research Thesis submission* in partial fulfilment of the requirements for the award of degree of **Doctor of Philosophy**.

### Research Guides



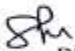
Dr. Sharnappa  
Joladarashi  
Professor



Dr. Ramesh M.R  
Professor



Department of Mechanical Engineering  
NITK, Surathkal

  
Chairman - DRPC  
Date 12/6/2024



## ACKNOWLEDGMENTS

It is my great pleasure and privilege to thank to **Dr. Sharnappa Joladarashi**, Professor, Department of Mechanical Engineering, National Institute of Technology, Karnataka, Surathkal for his exemplary guidance, inspiration and constructive criticism during the course of this work. I would like to express my immense sense of gratitude to **Dr. Ramesh M.R**, Professor, Department of Mechanical Engineering, National Institute of Technology, Karnataka, for always expressing his willingness to support and allowed me tremendous freedom to explore the project with valuable research ideas.

I wish to express my sincere thanks to **Prof. S. M. Murigendrappa**, Head, Department of Mechanical Engineering, and all former HOD's, faculty members, technical and administrative staff of the Mechanical Engineering Department, National Institute of Technology, Karnataka, for their kind help in providing the facilities as and when needed. I extend my sincere thanks to my thesis referees, **Prof. A. Arockiarajan**, IIT Madras & **Prof. Ramji. M**, IIT Hyderabad, for reviewing the thesis and enhancing the quality of work. I would like to extend my gratefulness to DTAC members, **Dr. Sudhakar C Jambagi** & **Prof. Shashidhar G Koolagudi**, NITK Surathkal for their valuable suggestions.

I sincerely thank my RPAC members, **Dr Ranjith M**, Associate Professor, Department of Mechanical Engineering, National Institute of Technology, Karnataka and **Dr. Nagendrappa H**, Associate Professor, Department of Electrical and Electronics Engineering, National Institute of Technology, Karnataka, for providing valuable suggestions and supporting me in multiple occasions. I am grateful to **Dr. Shashi Bhushan Arya**, Associate professor, Department of Metallurgical and Materials Engineering, NITK Surathkal for his immense support in granting access to perform experiments in his laboratory. I also take this opportunity to express my gratitude to **Mr. R. K. Bisen**, MD, Insmart Systems, Hyderabad, for generously providing access to the ball milling facility used in this research.

I would like to thank **Mr. Jagadeesh C**, research scholar in the department of mechanical engineering for his everlasting support, optimism and all the brainstorming sessions we had during the course of this work. I also take this opportunity to

acknowledge **Dr. Ujwal kiran rokkala and Dr. Durga Prasad** for their brilliant ideas and assistance during my challenging situations. I must say a special thank you to **Dr. Surya Rao**, who never failed to help me in times of need. I also extend my gratitude to my fellow research scholars **Mr. Chandramouli, Mr. Netrananda behera, and Mr. Ramprasad** for their continuous help and encouragement during the research work. Above all, I am short of words to thank my friend, **Phani Kumar PVS**, research scholar in the department of mechanical engineering for his unwavering support during the course of this work.

I am thankful to the Director and administration of the National Institute of Technology, Karnataka, for providing all the necessary facilities and funds to carry out my work. I also acknowledge financial support provided by the Ministry of Education, Government of India. I would also thank Central Research Facility, NIT Karnataka for providing access to various characterization and testing facilities. Finally, I am extremely grateful to my dear parents, **Sri Shesha Charyulu** and **Smt Vasantha Lakshmi** for their undying love and support in every phase of my life.

**(SYAM NARAYANA ADDEPALLI)**

## ABSTRACT

Maraging steels, widely used in the aircraft landing gear components were subjected to wear due to the harsh working conditions. Surface modification of these components by the deposition of advanced coating materials prolong their life. High entropy alloys (HEA) are a contemporary class of materials with multiple primary elements having applications in different fields, owing to their exceptional mechanical and physical properties. Therefore the current research is aimed at enhancing the wear performance of maraging steels, by the deposition of HEA coatings.

CoCrNiTiMo<sub>x</sub> and CoCrNiTiW<sub>x</sub> (x: molar ratio; x= 0.5, 1, 1.5) HEAs were processed by mechanical alloying of pure metal powders for further application as feedstock in the High velocity oxy-fuel (HVOF) technique. The phase and microstructural transformation of the ball milled powders is investigated in detail by optimizing the milling time and speeds. The milling process is extended for 50 h and milled powder samples were collected at regular intervals of 10, 20, 30, 40 and 50 h to characterize the samples for their suitability to deposit using thermal spray techniques. The milled powders were characterized with respect to the phases, particle morphology, chemical homogeneity, particle size and crystallite sizes. Based on the characterization studies, the powders milled at a speed of 200 rpm for 10 h were selected as feedstock for HVOF deposition.

After the deposition of coatings, the microstructural and mechanical characterization of coatings were performed. The phases and microstructure of the deposited HEA coatings were determined by X-ray diffraction (XRD) and scanning electron microscope (SEM). The microhardness of the coating was determined by using a vickers indenter on the coatings cross-section, with a load of 300 g and a dwell time of 15 s. The deposited coatings fracture toughness was determined by using the Evans and Wilshaw's approach. The tribological behaviour of CoCrNiTiMo<sub>x</sub> and CoCrNiTiW<sub>x</sub> HEA coatings at elevated temperatures was studied extensively using a Pin-on-Disc tribometer. The deposited coatings exhibited a lamellar structure and good mechanical bonding with the substrate. The porosities of CoCrNiTiMo<sub>x</sub> and CoCrNiTiW<sub>x</sub> HEA coatings, as calculated using ImageJ software, were found to be in the range of 1-2%.

The mechanical performance of the CoCrNiTiMo<sub>x</sub> and CoCrNiTiW<sub>x</sub> HEA coatings revealed superior values, when compared to other HEA coatings. The microhardness of CoCrNiTiMo<sub>0.5</sub>, CoCrNiTiMo, and CoCrNiTiMo<sub>1.5</sub> HEA coatings were found to be 841±62 HV<sub>0.3</sub>, 927 ± 45 HV<sub>0.3</sub> and 952±23 HV<sub>0.3</sub>, respectively. On the other hand, the microhardness of CoCrNiTiW<sub>0.5</sub>, CoCrNiTiW, and CoCrNiTiW<sub>1.5</sub> HEA coatings were found to be 863±52 HV<sub>0.3</sub>, 951 ± 38 HV<sub>0.3</sub> and 1025±39 HV<sub>0.3</sub>, respectively. The fracture toughness of CoCrNiTiMo<sub>0.5</sub>, CoCrNiTiMo, and CoCrNiTiMo<sub>1.5</sub> HEA coatings were found to be 2.89 ± 0.31 (Mpa m<sup>1/2</sup>), 3.26 ± 0.25 (Mpa m<sup>1/2</sup>) and 3.79 ± 0.35 (Mpa m<sup>1/2</sup>) respectively. Likewise, the fracture toughness of CoCrNiTiW<sub>0.5</sub>, CoCrNiTiW, and CoCrNiTiW<sub>1.5</sub> HEA coatings, were found to be 3.22 ± 0.26 (Mpa m<sup>1/2</sup>), 3.54 ± 0.32 (Mpa m<sup>1/2</sup>) and 3.87 ± 0.3 (Mpa m<sup>1/2</sup>) respectively. Further, it can be witnessed that the as-sprayed HEA coatings exhibited a steady increment in the mechanical properties with an increment in the molar fraction of Molybdenum and Tungsten.

The specific wear rate of CoCrNiTiMo HEA coating dropped by 70.5%, declining from 17.34 ± 2.8 x10<sup>-6</sup> mm<sup>3</sup>/N-m to 5.1 ± 1.6 x10<sup>-6</sup> mm<sup>3</sup>/N-m, while CoCrNiTiW dropped by 76.3%, decreasing from 15.8 ± 3.7 x10<sup>-6</sup> mm<sup>3</sup>/N-m to 3.73 ± 2.1 x10<sup>-6</sup> mm<sup>3</sup>/N-m, with an increase in the temperature from RT to 600 °C. The wear rates of coatings exhibited a significant reduction at elevated temperatures, owing to the formation of TiO<sub>2</sub>, CoMoO<sub>4</sub>, NiO tribofilms for CoCrNiTiMo, and TiO<sub>2</sub>, CoWO<sub>4</sub>, WO<sub>3</sub> oxides for CoCrNiTiW. Further, the CoCrNiTiMo<sub>1.5</sub> HEA coatings offered better wear resistance, as compared to CoCrNiTiMo<sub>0.5</sub> HEA coatings, at any temperature and loading condition, due to the increment in the molar fraction of Molybdenum. Additionally, the CoCrNiTiW<sub>1.5</sub> HEA coatings exhibited superior wear performance, when compared to all the six compositions in the current research. The investigation of worn surfaces showed a transformation in wear mechanisms from adhesive and abrasive wear at room temperature to oxidative wear at elevated temperatures.

**Keywords:** High entropy alloy, High-Velocity Oxy-fuel spray, Wear, Mechanical alloying, Microstructure.

# CONTENTS

*DECLARATION*

*CERTIFICATE*

*ACKNOWLEDGEMENTS*

**ABSTRACT..... I**

**CONTENTS..... III**

**LIST OF FIGURES .....IX**

**LIST OF TABLES ..... XIII**

**ABBREVIATIONS ..... XV**

**NOMENCLATURE..... XVII**

**CHAPTER 1 INTRODUCTION ..... 1**

1.1 Background of study ..... 1

1.2 High Entropy Alloys ..... 3

1.3 Core effects of HEAs ..... 4

1.3.1 High entropy effect ..... 4

1.3.2 Lattice distortion effect ..... 4

1.3.3 Sluggish diffusion effect ..... 5

1.3.4 Cocktail effect ..... 6

1.4 Mechanical alloying ..... 7

1.4.1 Mechanism of alloying ..... 8

1.4.2 Nanocrystalline materials ..... 9

1.5 Thermal spray Coatings ..... 10

1.5.1 High Velocity Oxy-Fuel (HVOF) technique ..... 11

**CHAPTER 2 LITERATURE REVIEW ..... 13**

2.1 Processing of High Entropy Alloys (HEAs) ..... 13

2.1.1 Mechanical Alloying.....	13
2.1.2 Spark plasma sintering.....	16
2.1.3 Vacuum arc melting.....	17
2.2 Deposition of HEA coatings.....	18
2.2.1 Thin coatings.....	18
2.2.2 Laser cladding.....	20
2.2.3 Thermal spray coating.....	21
2.3 Functional performance of HEA coatings.....	23
2.3.1 Mechanical performance.....	23
2.3.2 Tribological performance.....	24
2.3.3 Corrosion resistance.....	27
2.4 Research gaps.....	28
2.5 Objectives of the study.....	29
2.6 Scope of the research work.....	29
2.7 Outline of the thesis.....	30
<b>CHAPTER 3 MATERIALS AND METHODOLOGY.....</b>	<b>33</b>
3.1 Selection of substrate material.....	33
3.2 Selection of feedstock powders.....	33
3.3 Processing of HEAs by MA.....	35
3.4 Deposition of HEA coatings using HVOF technique.....	36
3.5 High temperature tribological performance.....	38
3.6 Characterization of milled powders.....	40
3.6.1 XRF analysis of elemental powders.....	40
3.6.2 SEM and EDAX analysis.....	40
3.6.3 XRD analysis.....	40
3.6.4 Particle size analysis.....	40

3.7 Characterization of deposited coatings .....	41
3.7.1 Specimen preparation for cross-sectional analysis .....	41
3.7.2 Microstructural analysis.....	41
3.7.3 XRD analysis .....	41
3.7.4 Coating thickness .....	41
3.7.5 Porosity and density .....	41
3.7.6 Micro hardness.....	42
3.7.7 Fracture toughness .....	42
3.7.8 Surface Roughness.....	42
3.8 Characterization of worn samples.....	43
3.8.1 SEM analysis .....	43
3.8.2 XRD analysis .....	43
3.8.3 Raman spectroscopy .....	43
3.9 Summary .....	43
<b>CHAPTER 4 PROCESSING OF HIGH ENTROPY ALLOYS .....</b>	<b>45</b>
4.1 Characterization of pure metal powders .....	45
4.2 Processing of CoCrNiTiMo HEAs by Mechanical Alloying .....	48
4.2.1 Phase evolution of ball milled powders .....	48
4.2.2 Calculation of crystallite size and lattice strain .....	51
4.2.3 Microstructural evolution of milled powders .....	53
4.2.4 Particle size analysis .....	55
4.3 Processing of CoCrNiTiW HEAs by Mechanical Alloying .....	56
4.3.1 Phase evolution of ball milled powders .....	56
4.3.2 Calculation of crystallite size and lattice strain .....	58
4.3.3 Microstructural evolution.....	58
4.3.4 Particle size analysis .....	60

4.4 Solid Solution formation criteria in High entropy alloys.....	61
4.5 Summary .....	63
<b>CHAPTER 5 CHARACTERIZATION OF HEA COATINGS .....</b>	<b>65</b>
5.1 Characterization of CoCrNiTiMo <sub>x</sub> HEA coatings .....	65
5.1.1 Surface morphology.....	65
5.1.2 Cross-sectional microstructure.....	66
5.1.3 XRD studies .....	69
5.1.4 Microhardness.....	71
5.1.5 Fracture toughness .....	73
5.1.6 Surface Roughness and density .....	74
5.2 Characterization of CoCrNiTiW <sub>x</sub> HEA coatings.....	76
5.2.1 Surface morphology.....	76
5.2.2 Cross-sectional microstructure.....	77
5.2.3 XRD studies .....	81
5.2.4 Microhardness.....	82
5.2.5 Fracture toughness .....	84
5.2.6 Surface roughness and density.....	85
5.3 Summary .....	86
<b>CHAPTER 6 TRIBOLOGICAL STUDIES .....</b>	<b>87</b>
6.1 High Temperature tribological behaviour of CoCrNiTiMo <sub>x</sub> HEA Coatings.....	87
6.1.1 Frictional coefficient plots .....	87
6.1.2 Specific wear rate.....	89
6.1.3 Wear mechanisms .....	91
6.1.4 X-Ray diffraction .....	96
6.1.5 Raman Spectroscopy.....	99
6.2 High Temperature tribological behaviour of CoCrNiTiW <sub>x</sub> HEA Coatings.....	101

6.2.1 Frictional coefficient plots .....	101
6.2.2 Specific wear rate.....	104
6.2.3 Wear mechanisms .....	106
6.2.4 X-Ray diffraction .....	112
6.2.5 Raman Spectroscopy.....	115
6.3 Wear mechanisms of substrate.....	117
6.4 Summary .....	118
<b>CHAPTER 7 CONCLUSIONS AND FUTURE WORK .....</b>	<b>121</b>
7.1 Conclusions.....	121
7.2 Scope of future work.....	123
<b>REFERENCES.....</b>	<b>125</b>
<b>BIO-DATA.....</b>	<b>144</b>



## LIST OF FIGURES

Figure 1.1 Schematic depicting the lattice distortion effect in HEAs (José et al. 2019)	5
Figure 1.2 Schematic showing the mean potential energy difference for pure metals and alloys (Zhang et al. 2014). .....	6
Figure 1.3 Collisions between balls and powders during MA (Suryanarayana 2019). .	8
Figure 1.4 Schematic showing the mechanism of coating build-up in thermal spray deposition techniques (Matthews, 2004). .....	11
Figure 3.1 Planetary Ball mill.....	35
Figure 3.2 Schematic of HVOF spray (Harith et al. 2018).....	36
Figure 3.3 Pin-on-disc tribometer used for tribological testing.....	38
Figure 3.4 Methodology of the research work.....	44
Figure 4.1 Surface morphology of metal powders; (a) Cobalt (b) Chromium, (c) Nickel, (d) Titanium, (e) Molybdenum and (f) Tungsten.....	46
Figure 4.2 X-ray Diffraction of pure metal powders; (a) Cobalt (b) Chromium, (c) Nickel, (d) Titanium, (e) Molybdenum and (f) Tungsten.....	47
Figure 4.3. XRD of CoCrNiTiMo HEA powders at different milling times using a speed of (a) 200 rpm and (b) 300 rpm. ....	50
Figure 4.4 Williamson- Hall plots of CoCrNiTiMo ball milled powders at 200 rpm (a) 10 h and (b) 50 h.....	52
Figure 4.5 Microstructural evolution of CoCrNiTiMo HEA powders after milling for a) 0 h b) 10 h c) 20 h d) 30 h, e) 40 h, and f) 50 h. ....	54
Figure 4.6 Chemical composition of CoCrNiTiMo milled at 200 rpm for 50 hours...55	55
Figure 4.7 Particle size distribution of CoCrNiTiMo HEA powders milled for a) 10 h and b) 50 h at a milling speed of 200 rpm. ....	56
Figure 4.8 Particle size distribution of CoCrNiTiMo HEA powders milled for a) 10 h and b) 30 h at a milling speed of 300 rpm. ....	56
Figure 4.9 XRD of CoCrNiTiW HEA powders at different milling times.....	57
Figure 4.10 Microstructural evolution of CoCrNiTiW HEA powders after milling for a) 0 h b) 10 h c) 20 h d) 30 h, e) 40 h, and f) 50 h. ....	59

Figure 4.11 Chemical composition of CoCrNiTiW HEA powders milled at 200 rpm for 50 hours.....	60
Figure 4.12 Particle size distribution of CoCrNiTiW HEA powders milled for (a) 10 h and (b) 50 h at a milling speed of 200 rpm. ....	61
Figure 5.1 Surface morphology of (a) CoCrNiTiMo <sub>0.5</sub> , (c) CoCrNiTiMo and (e) CoCrNiTiMo <sub>1.5</sub> HEA coatings deposited by HVOF spray. (b), (d), (f) shows the EDS analysis of corresponding HEA coated surfaces respectively. ....	65
Figure 5.2. Cross-sectional microstructure of (a), (b) CoCrNiTiMo <sub>0.5</sub> (c), (d) CoCrNiTiMo, (e), (f) CoCrNiTiMo <sub>1.5</sub> HEA coatings in backscattered electron mode, showing coating thickness and lamellar structure. ....	67
Figure 5.3. Interfacial bonding of (a) CoCrNiTiMo <sub>0.5</sub> , (b) CoCrNiTiMo, and (c) CoCrNiTiMo <sub>1.5</sub> HEA coatings with the Substrate. ....	68
Figure 5.4 Elemental mapping of (a) CoCrNiTiMo <sub>0.5</sub> , (b) CoCrNiTiMo, and (c) CoCrNiTiMo <sub>1.5</sub> HEA coating cross-section.....	69
Figure 5.5 X-ray diffraction studies of HVOF sprayed (i) CoCrNiTiMo <sub>0.5</sub> , (ii) CoCrNiTiMo, and (iii) CoCrNiTiMo <sub>1.5</sub> HEA coating.....	70
Figure 5.6 Vickers microhardness of (a) CoCrNiTiMo <sub>0.5</sub> , (b) CoCrNiTiMo, and (c) CoCrNiTiMo <sub>1.5</sub> HEA coatings.....	72
Figure 5.7 Optical microscope image showing the crack propagation for (a) CoCrNiTiMo <sub>0.5</sub> , (b) CoCrNiTiMo, and (c) CoCrNiTiMo <sub>1.5</sub> HEA coatings under a Vickers indenter.....	74
Figure 5.8 Profilometry studies showing the 3-dimensional roughness plot of (a) CoCrNiTiMo <sub>0.5</sub> , (c) CoCrNiTiMo, and (e) CoCrNiTiMo <sub>1.5</sub> HEA Coatings. Corresponding 2D line profiles can be seen in (b), (d), (f) respectively. ....	75
Figure 5.9 Surface morphology of (a) CoCrNiTiW <sub>0.5</sub> , (c) CoCrNiTiW and (e) CoCrNiTiW <sub>1.5</sub> HEA coatings deposited by HVOF spray. (b), (d), (f) shows the EDS analysis of corresponding HEA coated surfaces respectively. ....	76
Figure 5.10 Cross-sectional microstructure of (a), (b) CoCrNiTiW <sub>0.5</sub> and (c), (d) CoCrNiTiW and (e), (f) CoCrNiTiW <sub>1.5</sub> HEA coatings. ....	78
Figure 5.11 Interfacial bonding of (a) CoCrNiTiW <sub>0.5</sub> and (b) CoCrNiTiW and (c) CoCrNiTiW <sub>1.5</sub> HEA coating with the substrate. ....	79

Figure 5.12 Elemental mapping of (a) CoCrNiTiW <sub>0.5</sub> , (b) CoCrNiTiW and (c) CoCrNiTiW <sub>1.5</sub> HEA Coating cross-section. ....	80
Figure 5.13 XRD analysis of HVOF sprayed (i) CoCrNiTiW <sub>0.5</sub> and (ii) CoCrNiTiW and (iii) CoCrNiTiW <sub>1.5</sub> HEA coatings. ....	81
Figure 5.14 Vickers microhardness of (a) CoCrNiTiW <sub>0.5</sub> , (b) CoCrNiTiW and (c) CoCrNiTiW <sub>1.5</sub> HEA coating. ....	83
Figure 5.15 Optical microscopy showing the cracks generated for (a) CoCrNiTiW <sub>0.5</sub> , (b) CoCrNiTiW and (c) CoCrNiTiW <sub>1.5</sub> HEA coatings during the indentation fracture toughness test. ....	84
Figure 5.16 Profilometry studies showing the 3-dimensional roughness plot of (a) CoCrNiTiMo <sub>0.5</sub> , (c) CoCrNiTiMo, and (e) CoCrNiTiMo <sub>1.5</sub> HEA coatings. Corresponding 2D line profiles can be seen in (b), (d), (f) respectively. ....	85
Figure 6.1 Friction coefficient plots of worn-out samples at different temperatures for CoCrNiTiMo <sub>0.5</sub> at (a) 2kg (b) 4kg, CoCrNiTiMo at (c) 2 kg (d) 4 kg and CoCrNiTiMo <sub>1.5</sub> at (e) 2 kg (f) 4 kg loading condition. ....	88
Figure 6.2 Specific wear rate plots of Substrate and CoCrNiTiMo <sub>x</sub> HEA coatings at (a) 2kg normal load and (b) 4kg normal load. ....	90
Figure 6.3 SEM images showing the wear mechanisms of CoCrNiTiMo <sub>0.5</sub> HEA worn surfaces at a) RT b) 200 °C c) 400 °C d) 600 °C in secondary electron imaging mode. ....	92
Figure 6.4 SEM images showing the wear mechanisms of CoCrNiTiMo HEA worn surfaces at a) RT, b) 200°C, c) 400°C, d) 600°C in secondary electron imaging mode. ....	94
Figure 6.5 SEM images showing the wear mechanisms of CoCrNiTiMo <sub>1.5</sub> HEA worn surfaces at a) RT, b) 200°C, c) 400°C, and d) 600°C in secondary electron mode. ....	95
Figure 6.6 XRD analysis of CoCrNiTiMo <sub>0.5</sub> HEA Coatings after wear testing at (i) RT, (ii) 200°C, (iii) 400°C, and (iv) 600°C. ....	97
Figure 6.7 XRD analysis of CoCrNiTiMo HEA Coatings after wear testing at (i) RT, (ii) 200°C, (iii) 400°C, and (iv) 600°C. ....	98
Figure 6.8 XRD analysis of CoCrNiTiMo <sub>1.5</sub> HEA Coatings after wear testing at (i) RT, (ii) 200°C, (iii) 400°C, and (iv) 600°C. ....	99

Figure 6.9 Raman spectroscopy of (a) CoCrNiTiMo <sub>0.5</sub> (b) CoCrNiTiMo, and (c) CoCrNiTiMo <sub>1.5</sub> HEA coating's after wear testing at 600 °C.....	100
Figure 6.10 Frictional coefficient plots of (a) CoCrNiTiW <sub>0.5</sub> , (c) CoCrNiTiW and (e) CoCrNiTiW <sub>1.5</sub> , at different temperatures under a load of 2 kg. (b), (d), (f) represents the frictional plots of CoCrNiTiW <sub>0.5</sub> , CoCrNiTiW and CoCrNiTiW <sub>1.5</sub> HEA coatings respectively, at a load of 4kg. ....	102
Figure 6.11 Specific wear rates of the substrate and CoCrNiTiW <sub>x</sub> HEA coatings at (a) 2kg load and (b) 4kg load. ....	105
Figure 6.12 SEM images showing the wear mechanisms of CoCrNiTiW <sub>0.5</sub> HEA worn surfaces at a) RT b) 200 °C c) 400 °C d) 600 °C in Secondary electron imaging mode. ....	108
Figure 6.13 SEM images showing the wear mechanisms of CoCrNiTiW HEA worn surfaces at a) RT b) 200°C c) 400°C d) 600°C in Secondary electron imaging mode. ....	109
Figure 6.14 SEM images showing the wear mechanisms of CoCrNiTiW <sub>1.5</sub> HEA worn surfaces at a) RT b) 200°C c) 400°C d) 600°C in Secondary electron imaging mode. ....	111
Figure 6.15 X-ray diffraction of worn surfaces of CoCrNiTiW <sub>0.5</sub> HEA coatings after wear testing at (i) RT, (ii) 200 °C, (iii) 400 °C, and (iv) 600 °C. ....	113
Figure 6.16 X-ray diffraction of worn surfaces of CoCrNiTiW HEA coatings after wear testing at (i) RT, (ii) 200 °C, (iii) 400 °C, and (iv) 600 °C.....	114
Figure 6.17 X-ray diffraction of worn surfaces of CoCrNiTiW <sub>1.5</sub> HEA coatings after wear testing at (i) RT, (ii) 200 °C, (iii) 400 °C, and (iv) 600 °C. ....	115
Figure 6.18 Raman spectroscopy of (a) CoCrNiTiW <sub>0.5</sub> (b) CoCrNiTiW, and (c) CoCrNiTiW <sub>1.5</sub> HEA coating's after wear testing at 600 °C. ....	116
Figure 6.19 SEM images showing the wear mechanisms of maraging steel substrate after wear testing at (a) RT, (b) 200 °C (c) 400 °C, and (d) 600 °C. ....	118

## LIST OF TABLES

Table 3.1 Chemical composition (wt. %) of maraging steel 250.....	33
Table 3.2 Composition of HEAs used in the current study .....	34
Table 3.3 Properties of the Elemental metal powders .....	34
Table 3.4 Process parameters used in HVOF .....	37
Table 3.5 Parameters used for Pin-On-disc tribometer.....	39
Table 4.1 Characterization of as-received metal powders .....	46
Table 4.2 Crystallite size and lattice strain of CoCrNiTiMo Ball milled powders.....	52
Table 4.3 Calculation of crystallite size and lattice strain for CoCrNiTiW HEA .....	58
Table 4.4 Thermodynamic parameters of processed High entropy alloy: .....	63
Table 5.1 Chemical composition of highlighted points in Figure 5.2 (at %).....	67
Table 5.2 Chemical composition of highlighted points in Figure 5.10 (at %).....	79
Table 6.1 EDS analysis of specified points in Figure 6.3 showing the chemical compositions in at% .....	93
Table 6.2 EDS analysis of specified points in Figure 6.4 showing the chemical compositions in at% .....	94
Table 6.3 EDS analysis of specified points in Figure 6.5 showing the chemical compositions in at% .....	95
Table 6.4 EDS analysis of specified points in Figure 6.12 showing the chemical compositions in at% .....	108
Table 6.5 EDS analysis of specified points in Figure 6.13 showing the chemical compositions in at% .....	110
Table 6.6 EDS analysis of specified points in Figure 6.14 showing the chemical compositions in at% .....	111



## **ABBREVIATIONS**

HEA	High Entropy Alloy
HVOF	High Velocity Oxy Fuel
MA	Mechanical Alloying
SEM	Scanning Electron Microscopy
EDS	Energy Dispersive Spectroscopy
XRD	X-Ray Diffraction
XRF	X-Ray Fluorescence
OM	Optical Microscope
COF	Coefficient of Friction
FCC	Face Centred Cubic
BCC	Body Centred Cubic
HCP	Hexagonal Close Packed
VEC	Valence Electron Concentration
ASTM	American Society for Testing and Materials



## NOMENCLATURE

W	Specific wear rate	$\text{mm}^3/\text{N}\cdot\text{m}$
V	Volumetric wear	$\text{mm}^3$
L	Normal load	N
S	Sliding distance	m
$\rho$	Density of coating	$\text{g}/\text{cm}^3$
m	Mass loss of the coated sample before and after wear testing	g
$m_a$	mass of the coating in air	g
$m_1$	mass of the coating in water	g
$\Delta S_{mix}$	Entropy of mixing	J/mol. K
$\Delta H_{mix}$	Enthalpy of mixing	KJ/mol



# CHAPTER 1

## INTRODUCTION

### 1.1 Background of study

Wear refers to the progressive damage or deterioration that occurs when surfaces come into contact and experience relative motion. There are several types of wear, each characterized by specific mechanism and contributing factors. The classification of wear includes abrasive wear, erosive wear, sliding wear and corrosive wear. Among the different types of wear, sliding wear is a common phenomenon, which is widely responsible for the failure of multiple engineering components. Some notable applications of sliding wear include automotive brake systems and engine components, bearings, shafts, couplings, and aircraft landing gear components. The wear rate of these components is affected by several factors including the nature of interacting surfaces, loading, environmental condition and sliding speed. Frictional forces play a crucial role in the material removal from the surfaces during sliding wear.

The tribological performance of sliding parts is crucial in specific applications, to safeguard the engineering components against the harsh working conditions and enable their proper functioning. Therefore, understanding the nuances of sliding wear is essential to mitigate the wear rates. Surface modification techniques seems to be a promising approach, in order to retain the bulk properties of the underlying substrate and reduce the degradation at the surface. Several surface modification techniques including carburizing, nitriding, thermal spray coatings, laser cladding, thin films were widely utilised in order to augment the surface characteristics of the material.

Carburizing and Nitriding surface hardening techniques may cause distortion in the shape of the treated components and induce brittleness. Laser cladding forms thick coatings with excellent metallurgical bonding but induces high thermal stresses and deformation in the system. Physical and chemical vapour deposition techniques were specifically used to develop thin films to enhance the coatings' electrical and corrosive performance. Therefore, various thermal spray techniques, including plasma spray (Purushotham et al. 2023; Xiao et al. 2020a), high-velocity oxy-fuel spray (HVOF)

(Srivastava et al. 2019), cold spray (Yin et al. 2019; Yurkova i Bilyk 2020), and flame spray (Pal et al. 2023), were investigated to explore its application in different areas. Thermal spray deposition methods were widely preferred due to their versatility in depositing different materials without deteriorating the properties of the substrate. Among the thermal spray deposition techniques, HVOF spray forms dense coatings with lamellar microstructures, possessing minimum porosity and good mechanical bonding with the substrate (Löbel et al. 2017; Srivastava et al. 2019).

Maraging steels, frequently employed in the aerospace industries for high-stress applications such as landing gear and rocket engine components, were prone to wear due to repeated impact and sliding contacts. Therefore, enhancing the functional performance of these components using surface modification techniques seems to be a viable alternative. Researchers and engineers continually explore new materials, coatings, and lubrication techniques to improve the resistance of components to sliding wear. In the current study, high entropy alloy (HEA) coatings were deposited onto maraging steels using HVOF technique to enhance the tribological performance.

HEA coatings find their applications in numerous fields, including aerospace, automotive, energy sector and industrial machinery. In aerospace industry, landing gear components experiences significant wear and tear during take-off and landing. HEA coatings can enhance the wear resistance of landing gear components, increasing their lifespan. Further, the superior resistance of HEAs to oxidation and corrosion makes them ideal for certain aircraft parts including combustion chambers, nozzles, bearings and shafts. HEA coatings can significantly reduce wear and friction in automobile engine components such as pistons, cylinder liners, and valves resulting in an enhancement in engine efficiency and longevity. HEA coatings can also be used as radiation shielding materials in nuclear reactors and help in protecting components from radiation damage. Wind turbine components, particularly those exposed to harsh weather conditions, can benefit from the enhanced wear and corrosion resistance provided by HEA coatings.

HEA coatings offer several advantages over traditional coatings, making them an attractive option for various applications, particularly in demanding environments. HEA coatings generally exhibit higher hardness and strength due to their multi-

principal element composition, resulting in better resistance to mechanical wear and deformation. HEAs often have higher fracture toughness, making them less prone to cracking under stress compared to traditional coatings. The unique microstructure of HEA coatings can lead to lower friction coefficients, reducing wear in high-friction environments. HEA coatings maintain their structural integrity and performance at higher temperatures compared to many traditional coatings, making them suitable for several high temperature applications.

## 1.2 High Entropy Alloys

HEAs are a contemporary class of materials characterized by five or more primary elements in approximately equal amounts. HEAs were quite different from the conventional alloying approach, which usually contains one or two principal elements. HEAs intentionally incorporate multiple principal elements to introduce a high level of disorder or entropy in their structure. The content of individual elements in a HEA can vary within the range of 5-35 at. % (Cantor et al. 2004). HEAs exhibit a wide range of desirable properties, including exceptional hardness (Chen i Suprianto 2020), thermal stability (Shivam 2020), tensile strength (Zhang et al. 2020), corrosion resistance (Wang et al. s.d.), and wear resistance (Chen et al. 2019c). These exceptional properties emerge as a result of their distinctive attributes, which encompass high mixing entropy, sluggish diffusion kinetics, and lattice distortion. According to Gibb's free energy rule, the compounds with higher mixing entropies possess lower free energies, restricting the formation of multiple intermetallic compounds. Therefore, many HEAs were seen to form stable solid solutions with simple FCC or BCC phases (Tsai i Yeh 2014; Zhang et al. 2014). The main fundamental in the design of HEA is that the entropy of the system is maximum at equimolar composition. Further, the entropy of the system increases with the inclusion of more elements to the system. Gibbs free energy rule states that the systems free energy decreases with a rise in the entropy of the system ( $\Delta G_{mix} = \Delta H_{mix} - T\Delta S_{mix}$ ). The drop in the free energy of the system restricts the formation of multiple intermetallic compounds, thereby enabling the formation of solid solutions. (Tsai et al. 2014; Zhang et al. 2014)

HEAs were widely synthesised as bulk materials using arc melting (Ghassemali et al. 2017; Sathiaraj i Bhattacharjee 2015), mechanical alloying (Shivam et al. 2020) and

spark plasma sintering techniques (Alvi i Akhtar 2019; Zhang et al. 2016). The main drawbacks associated with melting and casting routes are segregation of the constituents and inhomogeneity in the microstructure. However, producing HEAs in large quantities presents a significant cost challenge due to the expensive nature of the pure metal powders. The application of HEAs as coatings offers several advantages, including cost reduction and improvement in the functional properties of the substrate.

### **1.3 Core effects of HEAs**

HEAs possess four core effects, namely high entropy effect, lattice distortion effect, sluggish diffusion, and cocktail effect. High entropy effect is crucial in the thermodynamics of phase formation, Sluggish diffusion is responsible for slowing down the kinetics of phase formation and favours the formation of nanostructures. Lattice distortion determines the mechanical and physical properties of the alloy. Cocktail effect is responsible for achieving composite effect on properties.

#### **1.3.1 High entropy effect**

In thermodynamics, entropy refers to the measure of disorder or randomness in a system. In traditional alloys, there is a relatively ordered arrangement of atoms in the lattice structure. In the context of HEAs, the high entropy effect is a consequence of the increased disorder introduced by the presence of multiple elements. This disorder arises because the atoms of different elements are distributed randomly throughout the crystalline structure of the alloy, rather than forming a more ordered and predictable pattern. In line with the Gibbs free energy rule, the systems with higher entropies possess lower free energies. The lower free energy of the system constrains the emergence of several intermetallic compounds, thereby facilitating the formation of solid-solution phases (Chen et al. 2018).

#### **1.3.2 Lattice distortion effect**

Lattice distortion refers to the alteration or deformation of the regular crystal lattice structure in a material. It can be seen that in a pure metal, all the lattice sites are occupied by the same element (Figure 1.1). However, in case of multiple principal elements, the different lattice sites were occupied by different elements possessing distinct atomic sizes. The elements bigger in size induce compressive stresses, whereas the elements smaller in size induce tensile stresses. The existence of compressive and tensile stresses

distorts the lattice, as can be seen in Figure 1.1. Lattice distortion can be a hindrance to the movement of dislocations, which thereby leads to an enhancement in the strength of material (Zhang et al. 2014).

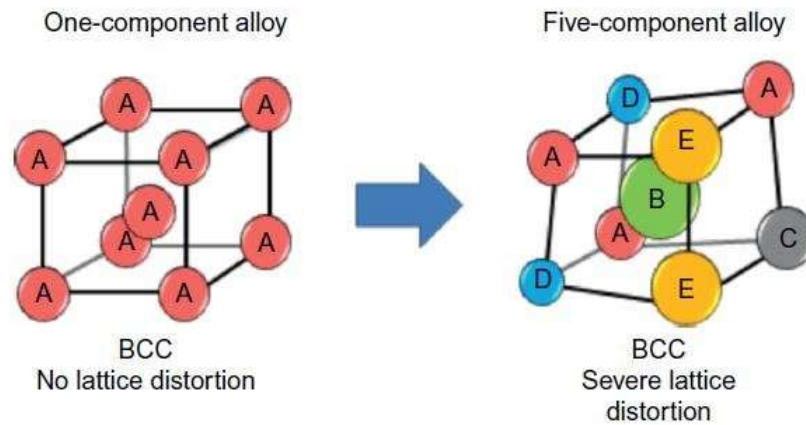


Figure 1.1 Schematic depicting the lattice distortion effect in HEAs (José et al. 2019)

### 1.3.3 Sluggish diffusion effect

Sluggish diffusion refers to the slow or limited movement of atoms or particles within a material. In the context of materials science, diffusion is the phenomenon where atoms migrate from areas of greater concentration to those of lesser concentration. This movement is essential for various processes, such as phase transformations, heat treatment, and the development of microstructures in materials.

The kinetics of diffusion and phase transformation in HEAs exhibit a notably slower pace compared to pure metals or conventional alloys. In HEA's, the existence of multiple primary elements leads to a variety of neighbouring atoms at each lattice site. Therefore, the mean potential energy difference between lattice sites is predominantly high. On the other hand for pure metals, where all the lattice sites were occupied by the same element, the value of mean potential energy difference is zero. So this variation in the mean potential energy at different lattice sites makes the diffusion of the atoms very difficult (Tsai et al. 2014). Additionally, the diffusion coefficients of individual elements within a HEA were distinct. For example the elements with High melting point have very lesser diffusion coefficients. Phase transformations occur only when there is coordinated diffusion among the constituent elements. So the slow diffusion of certain elements obstructs the phase transformation. From Figure 1.2, it can be seen that

the mean potential energy difference is highest for HEAs and zero for pure metals. Further, the diverse mix of elements can result in higher activation energies, making it more challenging for atoms to move through the material.

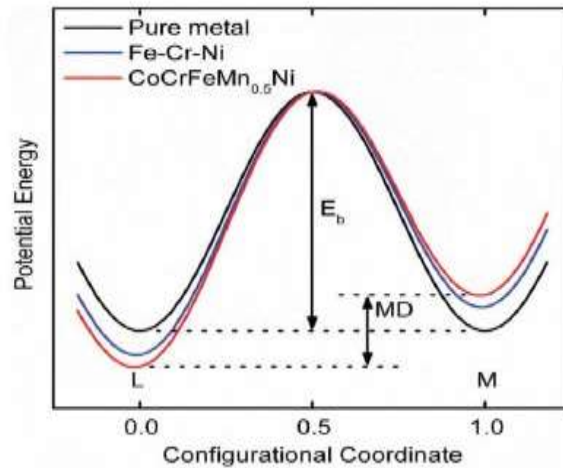


Figure 1.2 Schematic showing the mean potential energy difference for pure metals and alloys (Zhang et al. 2014).

Sluggish diffusion can contribute to the thermal stability of HEAs. The disorderly arrangement of atoms and limited mobility of certain elements can hinder significant changes, leading to thermal stability, even at elevated temperatures. Further, the disorderly arrangement of atoms and slow diffusion kinetics may lead to the persistence of specific phases or structures, influencing the material's properties over time.

### 1.3.4 Cocktail effect

The "cocktail effect" in the context of HEAs refers to the unique and beneficial combination of properties that arise from the diverse mixture of multiple elements in these alloys. In HEAs, the inclusion of multiple elements in roughly equal proportions leads to a synergistic effect, resulting in a combination of properties that can be superior to those of traditional alloys.

The characteristics of HEAs were determined not solely by the individual attributes of their constituent elements but also by the interactions among these elements. In addition to examining the isolated properties of each component, it is crucial to consider how these elements interact with each other, as these interactions play an important role in determining the overall behaviour and performance of the alloy. For instance,

Aluminium is a malleable metal with a relatively low melting point and a FCC crystal structure. However, incorporating aluminium into a HEA enables the formation of BCC solid solution, thereby elevating the alloy's hardness (Sriharitha et al. 2013; Wang et al. 2014b).

#### **1.4 Mechanical alloying**

MA is a solid-state non-equilibrium processing technique that produces materials with good chemical homogeneity. The main objective for exploring the MA technique is its inherent nature of processing elements with different melting points and vapor pressures (Suryanarayana et al. 2001). Almost every material, ranging from ductile, brittle and composite materials can be easily milled (Dwivedi et al. 2016; Koch 2017).

The mechanical performance of the material can be enhanced by processing them under non-equilibrium conditions. Non-equilibrium processing techniques refer to fabrication methods that deviate from thermodynamic equilibrium. In traditional equilibrium processing, materials reach a stable state dictated by thermodynamic principles. Non-equilibrium processing imparts high energy to the materials, enabling them to achieve the targeted microstructure and properties. Traditionally, researchers have employed temperature, pressure, light, or electricity to induce a transformation in the material from its equilibrium state to an energized condition. Mechanical alloying is a means of achieving the energized state by plastic deformation of powders using brute force. Some common non-equilibrium processing techniques include rapid solidification, mechanical alloying, severe plastic deformation, pulsed laser deposition, ion implantation and spark plasma sintering.

MA process involves the mechanical mixing or blending of powder particles of different metals or compounds in a ball mill, followed by a series of milling-induced reactions. The procedure includes the repetitive cycles of cold welding and fracturing of powder particles. The primary objective of mechanical alloying include achieving a homogeneous distribution of elements at the atomic level and refining the microstructure of the resulting material. The particle size and the alloying rate can be controlled by varying the milling speed and time during the mechanical alloying process.

Tungsten Carbide vial and balls were utilized in performing the milling process owing to their exceptional hardness and thermal stability. In order to mitigate the agglomeration of powders during the alloying process, a process control agent (PCA) is used in the milling media. Commonly used PCAs include sodium stearate, toluene and acetone. Mechanical alloying is performed in a controlled environment, under inert atmosphere using Argon gas, to limit the interaction with the external environment (Suryanarayana 2019). The collision and entrapment of the powders in between the balls can be seen in Figure 1.3.

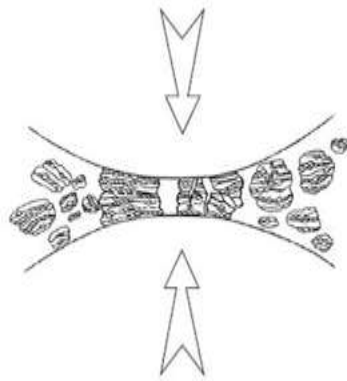


Figure 1.3 Collisions between balls and powders during MA (Suryanarayana 2019).

#### 1.4.1 Mechanism of alloying

The mechanical alloying (MA) process entails the cyclic process of, flattening, cold welding and fracturing of powders inside a ball mill. The initial interaction with the grinding balls results in the flattening and work hardening of the ductile metal powders. On the other hand, the brittle particles experience fragmentation, leading to a reduction in size. The various mechanisms during MA include:

**Cold Welding:** Powder particles are initially mixed and loaded into a ball mill. The high-energy collisions between the balls and powder particles result in cold welding, where the surfaces of the particles adhere to each other without the need for high temperatures.

**Fracturing:** As milling continues, the particles experience deformation due to the impact and shear forces. This leads to the fragmentation or fracturing of the particles into smaller sizes.

**Rewelding:** The newly formed smaller particles are again subjected to cold welding as they come into contact with each other. This promotes the intimate mixing of the different components, creating a finely dispersed alloyed powder.

**Steady state:** The process is repeated for a sufficient duration until a homogeneous alloyed powder is obtained.

The key to mechanical alloying lies in achieving a equilibrium between cold welding and fracturing. The repeated cycles of cold welding and fracturing enable the mixing of different components at the atomic level, resulting in a finely dispersed alloy with enhanced properties. The process is particularly valuable for creating alloys that may be difficult or impossible to produce through conventional melting and casting methods.

#### **1.4.2 Nanocrystalline materials**

Nanocrystalline materials refer to materials that have a nanoscale crystalline structure, meaning that the individual crystallites or grains within the material have dimensions in the order of nanometers. The term is often used to describe polycrystalline materials where the grain size is in the nanometer range. Nanocrystalline materials are often produced using techniques like ball milling, mechanical alloying, or other high-energy methods. These processes help in breaking down larger crystallites into smaller ones. Numerous studies have consistently shown that materials subjected to mechanical alloying exhibit a reduction in both powder particle size and grain size over milling time. The sizes diminish rapidly in the initial milling stages and undergo a more gradual decrease in the subsequent stages.

In traditional materials, the grain size typically lies in the micrometre range or above. However, in nanocrystalline materials, the grain size is observed to be in the nanometre scale, usually less than 100 nanometres. Nanocrystalline materials have a high surface area per unit volume, owing to the smaller grain size. This increased surface area can lead to enhanced reactivity and improvement in the mechanical properties, compared to their coarse-grained counterparts. It's important to note that the properties of nanocrystalline materials can be highly dependent on the specific material, processing techniques, and intended applications. The ability to control and tailor the grain size at

the nanoscale allows for the optimization of material properties for specific purposes, opening up new possibilities for innovation in various industries.

### **1.5 Thermal spray Coatings**

Thermal spray coatings are a class of surface engineering techniques used to apply coatings to substrates for various purposes, including enhancing wear resistance, corrosion protection, thermal insulation, and more. The process involves melting or partially melting coating materials and projecting them onto a prepared surface, where they solidify to form a coating. There are several methods of thermal spraying, with common techniques including flame spraying, plasma spraying, and high-velocity oxygen fuel (HVOF) spraying.

The mechanism of thermal spray coatings involves the meticulous application of a coating material onto a substrate through a series of well-coordinated steps. Initially, the chosen coating material, often in powdered form, is fed into a thermal spray gun. Subsequently, a high-temperature flame or plasma is generated within the gun, igniting and melting the powder particles. These molten or partially molten particles are then propelled towards the substrate at high velocities, where they impact and solidify, forming a layer. The rapid cooling and solidification contribute to the creation of a dense and adherent coating. The resulting coating mechanically bonds to the substrate, providing enhanced mechanical and tribological properties. The versatility of the thermal spray process allows for the application of coatings on diverse materials and surfaces, making it a widely employed technique in industries requiring surface modification and protection. The distinctive characteristic of thermal spray lies in its ability to cause minimal temperature rise of the substrate during the coating process, ensuring that the metallurgical properties of the substrate remain unaltered. The schematic of the coating deposition during thermal spray can be seen in Figure 1.4.

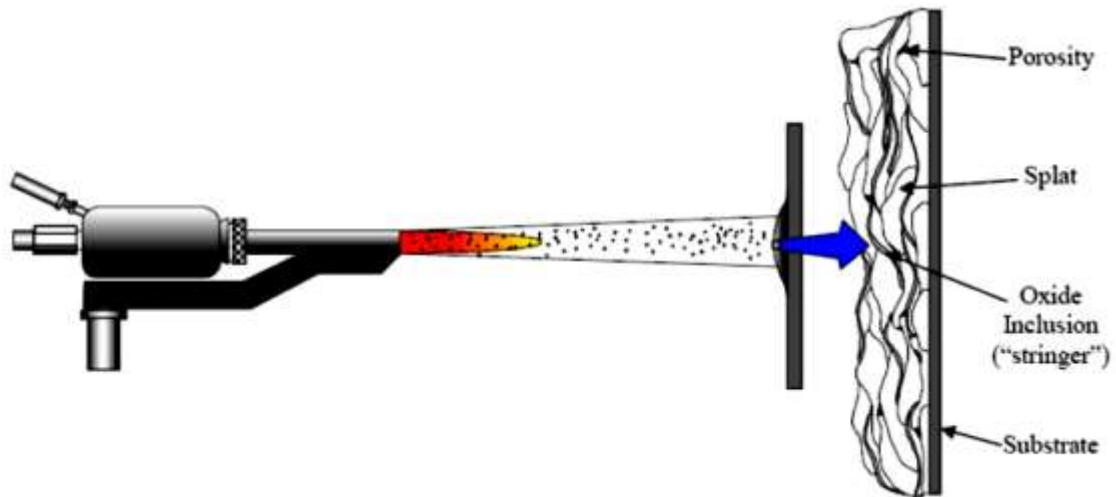


Figure 1.4 Schematic showing the mechanism of coating build-up in thermal spray deposition techniques (Matthews, 2004).

### 1.5.1 High Velocity Oxy-Fuel (HVOF) technique

HVOF technique operates through a controlled combustion process, where a mixture of fuel gas and oxygen ignites in a high-pressure chamber, generating a high-velocity and high-temperature flame. Fine powders in the particle size range of 15- 45 microns, comprising metals, ceramics, or carbides, are then injected into this flame. The intense heat causes the powder particles to melt or partially melt, and they are accelerated to high velocities. These molten particles impact the substrate, flattening and solidifying to form a dense coating. The porosity of the deposited coatings in HVOF technique were usually lesser than 2%. Notably, the HVOF process minimizes heat transfer to the substrate, preserving the metallurgical properties of the material. The repeated application of this process builds up a coating with enhanced mechanical and metallurgical characteristics, making HVOF a widely used technique for applications requiring wear resistance, corrosion protection, and thermal barriers.



## CHAPTER 2

### LITERATURE REVIEW

#### 2.1 Processing of High Entropy Alloys (HEAs)

HEAs have become popular in the recent days, due to their exceptional mechanical and functional properties. Nevertheless, processing of HEAs is a challenge owing to the difference in atomic sizes and melting points. Researches have processed HEA's using several techniques, such as vacuum arc melting (Sathiaraj and Bhattacharjee 2015), mechanical alloying (MA), and spark plasma sintering (SPS) (Raman et al. 2018).

##### 2.1.1 Mechanical Alloying

MA is a solid state processing technique and has the ability to process materials with distinct melting points and vapor pressures (Suryanarayana et al. 2001). Almost every material, ranging from ductile, brittle and composite materials can be easily milled (Dwivedi et al. 2016; Koch 2017). The development of nanocrystalline HEAs further enhanced the scope of high entropy alloys. It was observed that because of the extremely small dimension of the grains, most of the atoms in these materials are present near the grain boundaries and thus the materials exhibit better mechanical, physical and magnetic properties (Suryanarayana 2001).

Varalakshmi et al. (2008) synthesized nanocrystalline AlFeTiCrZnCu HEA by MA and reported the formation of BCC structure with a crystallite size of 10 nm. The hardness of the processed HEA was observed to be 2 GPa. Further, the authors reported that the AlFeTiCrZnCu HEA is thermally stable even after sintering at 800°C.

The thermal stability of the HEA's has been studied by various researchers after prolonged heat treatments using Differential Scanning Calorimetry (DSC), Thermo Gravimetric Analyzer (TGA), and X-ray Diffraction techniques. Mridha et al. (2013) studied the thermal stability of spark plasma sintered HEA upto 900°C and reported a better hardness of 6 GPa and relative density of 95 percent after sintering at 900°C

Babu et al. (2014) scrutinized the thermal stability of AlCoCrCuNiFeZn high-entropy alloy (HEA) produced through mechanical alloying. They employed DSC/TGA curves

with a heating rate of 20°C/min, reaching up to 1000°C. The mechanically alloyed powder displayed exothermic behaviour between 30-960°C, attributed primarily to the release of internal stresses and lattice strain induced during ball milling. Beyond 960°C, an endothermic peak emerged, indicative of the evolution of new phases. The AlFeCuCrMg<sub>x</sub> HEA synthesized by MA also possesses a exothermic curve in the range of 25- 450°C, associated to the release of internal stress during ball milling (Maulik i Kumar 2015).

Chen et al. (2015) synthesized Al<sub>0.75</sub>FeNiCrCo, Al<sub>0.75</sub>FeNiCr and Al<sub>0.75</sub>FeNiCrCoTi<sub>0.25</sub> HEA's by MA and reported the formation of BCC and FCC solid solutions in all the three alloys after milling for 30 hours. The solid solution phase formation has been validated by using TEM- Selective area electron diffraction studies. The authors reported that the Al<sub>0.75</sub>FeNiCrCo alloy depicted high strength, due to the solid-solution strengthening.

Murali et al. (2016) synthesized the AlCoCrCuFeZn<sub>x</sub> HEA by MA and investigated the effect of Zn variation on the phase formation of the HEA. The results reveal the phase transformation of AlCoCrCuFeZn<sub>x</sub> alloy from BCC + FCC phase to two FCC phases, with the increase in Zn atomic fraction in the HEA.

Salemi et al. (2016) delved into how varying ball sizes impact the alloying rate within CuNiCoZnAl HEA. Their findings revealed that the onset of solid solution formation occurred significantly earlier when using balls of different diameters. Mechanical alloying parameters such as milling time, ball to powder ratio, milling speed affect the particle dissolution, microstructure and phase evolution of the powders (Atashin et al. 2015).

Fu et al. (2016) compared the bulk coarse grained CoNiFeAlCu High entropy alloy with that of nanocrystalline CoNiFeAlCu HEA and observed that the nanocrystalline samples depicted a substantial growth in yield strength and vickers hardness. The ultra-high strength of the nanocrystalline HEA is mainly ascribed to the grain boundary strengthening.

Bureš et al. (2017) studied the influence of high temperature sintering on the mechanical properties of FeSiBAlNiMo HEA. The authors reported a noticeable rise in both the

transverse rupture strength and Young's modulus values. Specifically, the transverse rupture strength rose to 340 MPa from its initial value of 5 MPa, while the Young's modulus increased to 87 GPa from 7.5 GPa.

Vaidya et al. (2017) synthesized the AlCoCrFeNi HEA by sequential alloying of pure metal powders. The progression of phases during this sequential alloying process is influenced by the selection of the initial binary alloy and the sequence in which other constituents are mixed. Notably, this approach has been noted for providing opportunities to customize the phase composition for a specific alloy composition.

Kang et al. (2018) synthesized the refractory WNbMoTaV HEA, by powder metallurgical process and demonstrated the emergence of BCC phase after milling for 6 h. The sintered samples showed better yield strength and plastic strain, due to the interstitial strengthening, and orowan strengthening.

Tian et al. (2019) evaluated the influence of heat treatment on the phase evolution of CoCrFeNiTiAl HEA milled powders and reported the transformation of eutectic phase to two BCC phases after annealing at 600°C. The authors used n-heptane as the process controlling agent (PCA) in order to mitigate the agglomeration during ball milling.

Rogal et al. (2019) processed the AlCoCrFeNi HEA by varying the atomic percentages of the constituent elements. The FCC and BCC solid solution phases started forming after 35 hours of ball milling and the alloy showed better yield strength and Vickers hardness values.

Wang et al. (2019) synthesized a nanostructured refractory MoNbTaTiV HEA possessing a bcc phase by mechanical alloying for 40 hours. Remarkably, the mechanically alloyed powder retained its nanocrystalline structure and bcc phase even after undergoing annealing at 1200 °C, demonstrating the exceptional thermal stability of the powders.

Shivam et al. (2020) synthesized AlCoCrFeNi HEA by MA and conventional sintering. The microstructure of the sintered HEA exhibited a uniform distribution of coarser and finer grains. The coarser grains were in the range of 18-22 microns, whereas the finer grains were in the range of 2-10 microns. The mechanical alloyed powders depicted a

phase transformation after sintering from BCC phase to intermetallic laves phase and sigma phases. The sintered samples showed a significant rise in the microhardness and saturation magnetization with values measuring at  $919 \pm 18 \text{ HV}_{0.3}$  and  $70.05 \text{ A m}^2/\text{kg}$  (emu/gm).

Suprianto and Chen (2023) studied the role of Cu and Y on the phase characteristics of FeCoNiCrCu HEAs, synthesized by MA and high temperature sintering. The elemental segregation of Cu around the Cr-rich oxide clusters was observed during the high temperature sintering. Further, the high content of yttrium addition stabilized the formation of in-situ yttrium dispersoids, leading to an enhancement in the mechanical properties.

### **2.1.2 Spark plasma sintering**

Fu et al. (2013) synthesized the nanocrystalline  $\text{Co}_{0.5}\text{FeNiCrTi}_{0.5}$  HEA by MA and SPS. The combination of FCC and BCC phases seen during the MA process, undergone transition after sintering, resulting in the emergence of a FCC phase and sigma phase.

Moravcik et al. (2016) synthesized the  $\text{AlCoCrFeNiTi}_{0.5}$  HEA by MA followed by consolidation using SPS at  $1100^\circ\text{C}$ . It was observed that the BCC phase formed during MA, undergone transformation to form FCC, ordered BCC and sigma phase after sintering at  $1100^\circ\text{C}$ . However, the hardness of the SPS HEA, which is about 762 HV, is retained even after heat treatment.

Zhang et al. (2016) synthesized the  $\text{AlCoCrFeNi}$  HEA by SPS and documented the emergence FCC, disordered BCC, ordered BCC solid solution phases in the alloy. Their observations indicated that the presence of a spinodal structure in the BCC phase played a pivotal role in enhancing the strength of the alloy.

Mohanty et al. (2017) reported the metastability in HEA's after spark plasma sintering the milled powders. It was observed that the FCC and BCC phases, detected in the milling stage have undergone eutectoid transformation to form a FCC, laves phase and sigma phase. The presence of decomposed microstructure and sigma phases, imparts high hardness and elastic modulus to the sintered alloy.

Kumar et al. (2019) prepared the CoCrCuFeNiSi<sub>x</sub> ( $x = 0, 0.3, 0.6$  and  $0.9$  atomic %) HEA by powder metallurgy route and investigated the phase evolution and wear performance. A combination of FCC and BCC phases formed during milling transformed to FCC and sigma phases after sintering. Further, the authors noticed a substantial rise in the wear resistance with the addition of Si content.

Thürlová and Průša (2022) prepared the CoCrFeNiMn<sub>x</sub>Al<sub>20-x</sub> HEA by a combination of MA and SPS. Their exploration into the influence of manganese variation on the HEA's mechanical properties revealed a noteworthy correlation. The study demonstrated that an augmentation in the aluminum molar fraction resulted in a substantial increase in both strength and hardness. Additionally, the introduction of higher aluminum content played a crucial role in improving the alloy's performance in high-temperature oxidation conditions.

### **2.1.3 Vacuum arc melting**

Many high entropy alloy systems such as AlCoCrFeNi, CoCrFeMnNi and refractory high entropy alloys such as NbMoTaWV, WMoCrTiAl have been synthesized by arc melting and casting routes (Ghassemali et al. 2017; Naser-zoshki and Vahdati-khaki 2020; Sathiaraj and Bhattacharjee 2015; Senkov et al. 2011). The main drawbacks associated with melting routes are separation of the alloying elements and inhomogeneity in the microstructure.

Wang et al. (2014) investigated the effect of Al addition to CoCrFeNi using vacuum melting technique and reported the formation of dual FCC + BCC phase. A significant increase in the hot hardness has been observed with the increase in Al molar fraction.

Pouliá et al. (2017) synthesized the MoTaWNbV refractory HEA by vacuum arc melting and conducted a wear resistance assessment in comparison to the commercial nickel super alloy, Inconel 718. The study unveiled a substantial 80% reduction in the wear rates of the synthesized HEA when subjected to an Al<sub>2</sub>O<sub>3</sub> counter body. This improvement was attributed to the microsegregation of vanadium (V) and niobium (Nb) in the interdendritic regions.

Hsu et al. (2017) synthesized the NiCoFeCrSiAlTi HEA by vacuum arc melting. Their findings indicated that the HEA coating exhibited an impressive hardness of

approximately 800 HV, and its wear resistance surpassed that of bearing steel by a factor of two.

Hou et al. (2019) prepared AlFeCoNiB<sub>x</sub> HEA using vacuum arc melting and explored the impact of varying the molar fraction of boron (B) on the alloy's mechanical properties. The study revealed that an increase in B molar fraction from 0 to 0.2 at% led to an elevation in both yield strength and plastic strain of the HEA. This improvement was attributed to the formation of an FCC eutectic structure.

Das and Robi (2021) fabricated the WMoVCrTa and WMoVCrTaFe HEAs by vacuum arc melting and studied their mechanical properties at room temperature and elevated temperature. The authors observed that both the HEAs depicted high yield strength and hardness at high temperatures, enabling their application in gas turbine blades and nuclear reactor walls.

## **2.2 Deposition of HEA coatings**

The processing of HEAs in bulk form is expensive, considering the high prices of pure metal powders. Therefore, to reduce the costs, and impart the desired properties, surface modification of the substrate using cathodic arc vapor deposition (Pogrebniak et al. 2014), magnetron sputtering (Obeydavi et al. 2020), laser cladding (Gu et al. 2020), and thermal spray techniques (Siao et al. 2014; Xiao et al. 2020b) have been explored. Arc deposition and magnetron sputtering techniques were widely used for developing thin films with lower deposition rates. The laser cladding technique induces high residual stresses in the material, which may initiate cracks and alter the material's properties. Therefore many researchers preferred thermal spray techniques such as plasma, HVOF, and flame spray for depositing dense coatings resulting in better mechanical properties (Meghwal et al. 2022).

### **2.2.1 Thin coatings**

Hung et al. (2019) utilized magnetron sputtering technique to deposit VNbMoTaW and VNbMoTaWCrB refractory HEA coatings and reported that the BCC phase observed in VNbMoTaW HEA transformed to amorphous phase in VNbMoTaWCrB refractory HEA. Further, the addition of Cr and B resulted in a significant increment in the hardness, corrosion resistance and thermal stability of the HEA

Kim et al. (2019) investigated the mechanical and electrical properties of NbMoTaW refractory HEA thin films deposited by magnetron sputtering technique. The research reported a hardness of 12 GPa and electrical resistivity of  $168\mu\Omega$  cm, due to the existence of nanoscale grains.

Tüten et al. (2019) analyzed the microstructure, mechanical and sliding wear behaviour of TiTaHfNbZr HEA thin films coated on titanium by magnetron sputtering. The findings demonstrate a good sliding wear resistance of the deposited coatings, enabling their application in specific orthopaedic implants that were subjected to dynamic loading.

Obeydavi et al. (2020) examined the microstructural, mechanical and corrosive behaviour of FeCrMoCoCBSi thin film metallic glasses (TFMG) deposited by DC magnetron sputtering at distinct currents. Notably, the authors noted that the TFMG produced at a sputtering current of 0.3A displayed outstanding corrosion resistance coupled with favourable mechanical properties.

Nagy et al. (2020) developed nanocrystalline CoCrFeNi HEA thin films by PVD technique and compared the microstructure and hardness of the deposited coatings with the bulk nanocrystalline samples prepared by high pressure torsion (HPT) technique. The PVD films exhibited an exceptional hardness of  $9.8\pm 0.3$  GPa, while the HPT samples showed a hardness of  $7.3\pm 0.3$  GPa

Ustinov et al. (2021) deposited CrFeCoNiCu HEA coatings using physical vapour deposition (PVD) and investigated the effect of structure on the strength and damping properties. It was observed that the HEAs showed dual FCC structure for coatings deposited above 925 K, and single FCC structure for coatings deposited under 925 K. The single FCC phase condensate possessed higher microhardness, as compared to the dual FCC phase condensate and cast alloy. Further, both the single and dual FCC phases exhibited higher damping capacity than the widely used damping materials.

Liao et al. (2022) studied the impact of laser shock peening (LSP) on the corrosion performance of FeCoCrNiAl HEA coatings deposited by Physical vapour deposition (PVD) techniques. The authors observed that the passive films and compressive residual stresses induced during LSP resulted in enhancing the corrosion resistance.

### 2.2.2 Laser cladding

Zhang et al. (2017) reported that the coating micro hardness increased enormously from 700 HV to 1300 HV after annealing heat treatment. The HEA coating primarily consisted of a dominant BCC phase and a minor presence of TiW phase. Notably, the BCC solid solution phases exhibited remarkable resilience, showing minimal alteration even after annealing at 1200 °C for 20 hours.

Cai et al. (2017) has employed CALPHAD approach to estimate the phases and mechanical properties of the FeCoNiAlCu HEA. The resultant HEA coating manifested a composition comprising two phases, FCC and BCC, each characterized by lattice parameters of 3.664 Å and 3.634 Å, and 2.872 Å, respectively.

Yu et al. (2019) synthesized the AlCoCrFeNiTi HEA coating by MA and laser cladding techniques. The influence of the laser power on the mechanical properties is studied by varying the power. The authors observed a substantial rise in the mechanical properties of the coatings, produced by using a laser power of 1000 watts. Also it is seen that the deposited coatings exhibited phase transformation from supersaturated BCC solid solution to stable BCC and FCC phases.

Chen et al. (2019) processed the refractory HEA coating using Laser cladding and reported an average hardness and Young's modulus of 11GPa and 219.2GPa, respectively. Sha et al. (2019).observed that phase transformation occurs from BCC, FCC phase to BCC and sigma phase, as the content of Al increases in the laser cladded  $Al_xCoCrFe_{2.7}MoNi$  HEA. A higher micro hardness of 1142 HV has been reported for the laser cladded HEA.

Zhang et al. (2019) has followed ball milling and laser cladding technique for coating the  $FeNiCoCrTi_{0.5}Nb_x$  HEA coating onto the substrate. The  $FeNiCoCrTi_{0.5}Nb_x$  coatings have BCC, FCC, Laves phase and it has been observed that the content of Laves phase increased with the addition of Nb content in the coating. Further, the cladded coatings exhibit highest average hardness of 852.5 HV. Qiu (2020) developed CoCrFeNiMo HEA coating onto 45 steel using laser cladding and reported an enhancement in the hardness and wear performance of the coating.

### 2.2.3 Thermal spray coating

Thermal spray deposition methods were widely preferred due to its versatility in depositing different materials without deteriorating the properties of the substrate. Therefore, various thermal spray techniques, including plasma spray, high-velocity oxy-fuel spray (HVOF), cold spray, and flame spray, were investigated to explore its application in different areas (Meghwal et al. 2020). Among the thermal spray deposition techniques, HVOF spray forms dense coatings with lamellar microstructures, possessing minimum porosity and good mechanical bonding with the substrate (Löbel et al. 2021).

Siao et al. (2015) prepared the nanostructured AlCoCrFeNi and MnCoCrFeNi HEAs through ball milling, subsequently utilizing the milled powders as feedstock in the plasma spray technique. The mechanical properties of both HEA coatings exhibited anisotropy, attributed to their lamellar, composite-type microstructure. Specifically, AlCoCrFeNi featured a predominant BCC phase with a minor FCC phase, while MnCoCrFeNi showcased a major FCC and a minor BCC phase.

Tian (2016) studied the phase evolution of the ball milled AlCoCrFeNiSi powders after deposition of coating using plasma spray. The BCC and FCC solid solution phases, as detected by the ball milled powders were transformed to ordered BCC phase after plasma coating. The crystallinity and the crystal structure of the HEA powder as determined by the XRD, is validated using TEM-SAED patterns and it is found that they are in good agreement with each other. The coating material showed a good micro hardness of 612 HV and shows a better wear resistance with a volume wear rate of  $0.38 \times 10^{-4} \text{ mm}^3/\text{N}\cdot\text{m}$ .

Löbel et al. (2017) processed the HEA by three different processing techniques namely MA, blending and gas atomization techniques. The authors explored the effect of processing route on the microstructure and phase composition of the thermal spray coatings. It was observed that the coatings deposited using the gas atomized powders exhibited minimal microstructural defects, thereby leading to better wear resistance.

Jin et al. (2018) applied plasma spray to coat stainless steel with the FeCoCrNiAl<sub>0.5</sub>Si<sub>6</sub> high-entropy alloy (HEA), examining the influence of silicon concentration on the

alloy's microstructure, phase composition, and mechanical properties. The study revealed that as the molar fraction of silicon increased from 0 to 2%, the FCC phase decomposed, giving rise to the formation of BCC and Cr<sub>3</sub>Si phases. Moreover, the rise in silicon content corresponded to an improvement in both hardness and wear resistance of the alloy.

Tian et al. (2019) synthesized the AlCoCrFeNiTi HEA coating by plasma spray after Mechanical alloying the powders for about 10 hours. The XRD patterns indicate that the BCC phase, as formed during Ball milling transforms into FCC and ordered BCC phase after coating. The reported average microhardness of the HEA coating reached 642 HV, marking a significant fourfold increase compared to the stainless steel substrate material. Notably, the high-temperature wear performance of the coated samples surpassed that of flame-sprayed or laser-cladded NiCrBSi coatings.

Chen et al. (2019) fabricated the Al<sub>0.6</sub>TiCrFeCoNi HEA coating by HVOF spray and scrutinized its wear behavior across varying temperatures. The findings revealed a rise in the wear rate of the coatings as the temperature increased from room temperature to 300 °C, followed by a slight decline at 500 °C. This trend was associated with an upsurge in fatigue wear at 300 °C and the formation of oxide tribo films at 500 °C.

Vallimanan et al. (2019) prepared AlCoCrMoNi HEA coating using HVOF technique on steel substrate after ball milling for about 20 hours. The erosive wear of the coated HEA shows better performance when compared to that of conventional WC-CoCr and NiCrBSi coatings. The deposited coatings exhibited a hardness of 685 HV and a porosity of 0.93%, respectively.

Xiao et al. (2020) analysed the application of heat treatment on the wear performance of plasma coated FeCoNiCrSiAl<sub>x</sub> HEAs. The authors opined that a noteworthy reduction in wear rates of heat-treated coatings was observed due to the emergence of robust Cr<sub>3</sub>Ni<sub>5</sub>Si<sub>2</sub> intermetallic phase.

Löbel et al. (2020) developed the AlCoCrFeNiTi<sub>0.5</sub> HEA coating, by HVOF spray, and reported a decrease in wear rates at elevated temperatures, owing to the emergence of MgAl<sub>2</sub>O<sub>4</sub> spinel at 900 °C. Further, Liu et al. (2022a) noticed that the wear behaviour of CoCrFeNiW<sub>x</sub> HEA coating at different temperatures is sensitive to temperature.

## **2.3 Functional performance of HEA coatings**

The development of advanced materials that can endure harsh engineering conditions, like high-temperature processes, wear and corrosive environments, is crucial to ensure the reliable performance of mechanical components. Tribological performance of sliding parts is very important in specific crucial applications including the aerospace and automobile industries. So, several researchers investigated the application of HEAs as bulk materials and coatings to understand their wear behaviours in different environments.

### **2.3.1 Mechanical performance**

As High-Entropy Alloys (HEAs) comprise multiple elements, the composition of specific elements plays a pivotal role in shaping their phase composition, microstructure and mechanical properties. AlCoCrFeNi HEA is extensively studied by many researchers, owing to its exceptional combination of strength and toughness.

Shun et al. (2012) studied the effect of Ti addition on the mechanical properties of CoCrFeNi HEA and reported a 75% increment in the strength of the CoCrFeNiTi HEA. Ma and Zhang (2012) synthesized AlCoCrFeNi HEA with a single BCC phase and reported the yield strength and hardness to be 1373 MPa and 520 HV respectively. The AlCoCrFeNi HEA is widely studied, due to its eutectic nature, resulting in better strength and ductility. The addition of Mo to CoCrFeNi HEA induced hard intermetallic phases, leading to an improvement in the strength of the alloy (Liu et al. 2016; Qiu 2020).

Ghassemali et al. (2017) analysed the impact of distinct BCC and FCC phases on the initiation of cracks in the heat-treated AlCoCrFeNi alloy. Their findings revealed a dual-phase microstructure in the heat-treated AlCoCrFeNi HEA, comprising 79% BCC and 21% FCC phases.

Lizárraga et al. (2018) explored how the addition of W influences the phase evolution and magnetic properties of CoCrFeNi HEA. Their study indicated that with an increase in the atomic fraction of W, there was the formation of HCP and BCC phases. Qin et al. (2018) analysed the impact of Co on phase transformation of  $(\text{AlCoCrFeNi})_{100-x}\text{Co}_x$  HEA and observed an increment in the FCC phase fraction, with a rise in the Co atomic

fraction from 0-16 %. The authors also observed a significant improvement in plasticity, owing to a rise in the volume fraction of FCC phase.

Jin et al. (2018) coated the  $\text{FeCoCrNiAl}_{0.5}\text{Si}_x$  HEA on stainless steel by plasma spray and explored the impact of Si concentration on the alloy's microstructure, phase composition, and mechanical behaviour. The study revealed a transformation from FCC solid solution to BCC solid solution and  $\text{Cr}_3\text{Si}$  phase as the Si molar fraction increased from 0 to 2. The authors noted a substantial improvement in hardness, wear resistance, and overall mechanical properties of the HEA with the higher silicon content.

Zhang et al. (2019) investigated the impact of Nb content on the phase formation of  $\text{FeNiCoCrTi}_{0.5}\text{Nb}_x$  laser cladded HEA coatings. Their observations indicated that an increase in Nb molar fraction enhances the intensity of the laves phase, consequently improving the microhardness and mechanical properties of the coating.

Joseph et al. (2019) noted that elevating the Al molar fraction in  $\text{Al}_x\text{CoCrFeNi}$  HEA led to the stabilization of the BCC solid solution phase. Incorporating cobalt content led to the stabilization of the FCC phase and a notable enhancement in the plasticity ( $\text{AlCoCrFeNi}_{100-x}\text{Co}_x$  HEA (Qin et al. 2018).

Li et al. (2020) delved into the alloying impact of tungsten (W) on the phase evolution, microhardness, and mechanical properties of  $\text{CoCrFeNi}$  HEA. Their findings indicated improved mechanical properties in HEAs with higher molar fractions of W. Liu et al. (2021) examined the influence of silicon (Si) addition on the microhardness of  $\text{AlCoCrFeNiSi}_x$  HEA coatings. Their findings revealed a consistent and linear increase in microhardness values with the rise in Si content.

### **2.3.2 Tribological performance**

Pouliat et al. (2017) synthesized  $\text{MoTaWNbV}$  refractory HEA by vacuum arc melting and compared its wear resistance with commercial nickel superalloy, Inconel 718. The synthesised HEAs reported an 80% drop in the wear rates against the  $\text{Al}_2\text{O}_3$  counter body due to the microsegregation of V and Nb in the interdendritic regions.

Ayyagari et al. (2018) investigated the wear performance of  $\text{Al}_{0.1}\text{CoCrFeNi}$  and  $\text{CoCrFeMnNi}$  HEA in dry and ocean environments and found that the former HEA

exhibited better wear resistance in both the conditions, due to the emergence of oxide passivation layers. The worn surface morphologies indicate that the mechanism for wear rate is fatigue wear in case of  $\text{Al}_{0.1}\text{CoCrFeNi}$  and adhesive wear in case of  $\text{CoCrFeMnNi}$  HEA.

Argade et al. (2019) analysed the effect of Laser fluences on the wear performance of  $\text{AlCoCrFe}$  HEA coating deposited by laser additive manufacturing on Al substrate. The authors noticed that the HEA coating, developed using lesser laser fluence of  $17 \text{ J/mm}^2$  showed better wear resistance. This phenomenon can be attributed to a reduction in the volume fraction of the HEA phase and an increase in the intermetallic phase as the laser fluence rises.

Srivastava et al. (2019) deposited  $\text{FeCoCrNi}_2\text{Al}$  HEA coating using HVOF spray and reported a microhardness of  $610 \pm 30 \text{ HV}$ , which was much higher than the conventional  $\text{MCrAlY}$  coatings ( $250\text{-}520 \text{ HV}$ ). The researchers also assessed the erosive wear performance of  $\text{FeCoCrNi}_2\text{Al}$  HEA coatings across a temperature range from room temperature to  $800 \text{ }^\circ\text{C}$ . They observed the formation of a compact  $\text{Al}_2\text{O}_3$  layer at  $800 \text{ }^\circ\text{C}$ , leading to enhanced erosive wear performance.

Geng et al. (2020) observed a rise in the wear rate of  $\text{CoCrFeNi}$  HEA under vacuum conditions as the temperature varied from room temperature to  $800 \text{ }^\circ\text{C}$ . The increment in the wear rate is attributed to the reduction in strength and inability to form dense oxide tribofilms under vacuum conditions.

Gu et al. (2020) investigated the impact of Al addition on the  $\text{Al}_x\text{Mo}_{0.5}\text{NbFeTiMn}_2$  laser cladded HEA. They noted a phase transformation from a single BCC to a dual BCC with the increasing Al molar fraction in the HEA. Additionally, the authors reported enhanced wear resistance of the HEA coatings with the inclusion of molybdenum (Mo) content in the alloy.

Jin et al. (2020) highlighted that introducing Al to the  $\text{Al}_x\text{CoCrFeNiSi}$  HEA led to an improvement in microhardness. This improvement was attributed to the formation of both BCC and intermetallic phases. Xiao et al. (2020) investigated the wear rates of plasma sprayed  $\text{FeCoNiCrSiAl}_x$  HEA coatings after heat treatment and observed a

noticeable drop in the wear rates of the heat treated coatings, due to the formation of hard  $\text{Cr}_3\text{Ni}_5\text{Si}_2$  intermetallic.

Liang et al. (2020) also developed  $\text{AlCrFe}_2\text{Ni}_2\text{W}_{0.2}\text{Mo}_{0.75}$  HEA coating by laser cladding and evaluated its wear performance in different environments such as NaCl solution, sea water and deionized water. The authors observed that the friction and wear properties of the developed HEA coatings was the mildest in sea water conditions, owing to the lubrication effect of  $\text{Mg}(\text{OH})_2$ , and  $\text{CaCO}_3$ , on the surface of coating.

Liang et al. (2021) investigated the tribological performance of  $\text{AlCrFeNiW}_{0.2}\text{Ti}_{0.5}$  coating in artificial sea water and observed that the developed HEA coatings exhibited better wear performance compared to the Q235 steel and SUS304, against  $\text{Si}_3\text{N}_4$ , GCr15, YG6 counter faces. The authors attributed the better wear performance to the anomalous sunflower like microstructure, in which nanoscale spherical precipitates are thoroughly distributed in the core and petals region.

Li and Shi (2021) analysed the impact of aluminum content on the wear and corrosive performance of  $\text{Al}_x\text{CrFeCoNiCu}$  HEA coating and noticed that the wear performance of the coatings increased with the rise in molar fraction of Al. Fu et al. (2021) interrogated the effect of Mo variation on the tribocorrosion performance of laser cladded  $\text{CoCr}_2\text{FeNiMo}_x$  HEA coating and observed that the Mo addition drastically improved the micro hardness and tribocorrosive properties of the coating.

Nguyen et al. (2022) explored the wear behaviour of arc melted  $\text{CrFeNiAl}_{0.4}\text{Ti}_{0.2}$  HEA from 600-950 °C against  $\text{Si}_3\text{N}_4$  counter face. The results indicate that the wear rates gradually decrease, on increasing the temperature from 600 – 800 °C, and increases on further increasing the temperature to 950 °C. This phenomenon is attributed to the formation of continuous oxide layers at 800 °C and thermal softening of the alloy at 950 °C.

Liu et al. (2022) developed  $\text{FeCoCrAlNi}$  HEA coatings by plasma spraying and reported an enhancement in the wear performance, due to the oxidative wear. Yang et al. (2022) provided a comprehensive analysis of the alloying impact of silicon (Si) on the wear performance of  $\text{FeCoCrNiMoSi}_x$  HEA coatings developed by laser cladding.

They observed a substantial enhancement in the hardness and wear behaviour with the Si content in the alloy.

Huang et al. (2022) employed laser cladding to create a  $\text{CoCrCuFeNiTi}_x$  HEA coating. Their observations revealed that the addition of titanium (Ti) played a crucial role in the formation of a hard laves phase and protective  $\text{TiO}_2$  layers on the worn surface. Liu et al. (2022) investigated the effect of W on the dry sliding wear behaviour of  $\text{CoCrFeNiW}_x$  HEA coating at different temperatures and observed that the wear behaviour is sensitive to temperature.

Likewise, the HVOF-sprayed  $\text{AlCoCrFeNiTi}_{0.5}$  HEA coating reported a drop in the wear depths at elevated temperatures, due to the formation of  $\text{MgAl}_2\text{O}_4$  spinel at  $900^\circ\text{C}$  (Löbel et al. 2020). Adding W and Ti to the  $\text{Ti}_x\text{VNbTaW}_y$  refractory HEA also enhanced the wear resistance at  $600^\circ\text{C}$  because of the formation of tribofilms and friction-induced subsurface strengthening (You et al. 2022). Several comparative studies on the wear performance of bulk HEA's with the conventional materials also revealed a significant improvement in the wear resistance, making it an appropriate choice for exploring the HEA's further (Cheng et al. 2020; Nguyen et al. 2022).

### **2.3.3 Corrosion resistance**

Jiang et al. (2019) explored the corrosion performance of  $\text{AlCoCr}_x\text{FeNi}$  HEA and found that the incorporation of chromium (Cr) content resulted in a notable enhancement of the corrosion resistance in the HEA. Vallimanalan et al. (2019) performed the electrochemical corrosion studies on  $\text{AlCoCrMoNi}$  HEA coating and reported that the corrosion rate of the coated HEA is about  $0.00276$  mm/year, which is very less compared to that of  $\text{NiCrSiB}$  coatings. Niu et al. (2019) studied the impact of W molar fraction on the corrosion resistance of  $\text{CoCrFeNiW}_x$  HEA and observed that the addition of W lead to a significant improvement in the pitting resistance.

Aliyu and Srivastava (2019) investigated the effect of graphene oxide variation on the corrosive performance of  $\text{MnCrFeCoNi}$  HEA coating on mild steel samples. The authors observed that the addition of graphene oxide led to the drop in the corrosive current density and corrosion rate. The authors also reported significant microstructural

transformation, with the increase of GO, from homogenous alloy to FeCoNi rich regions embedded in MnCr matrix.

Liu et al. (2021) observed phase transformation from two BCC phases to a mixture of FCC and BCC phase, with the increase in molar fraction of Cr in the  $\text{AlCr}_x\text{NiCu}_{0.5}\text{Mo}$  HEA. The electrochemical corrosive studies shows the  $\text{AlCr}_2\text{NiCu}_{0.5}\text{Mo}$  HEA coating has better corrosive properties when compared to other compositions.

Muangtong et al. (2020) investigated the effect of Sn, Cu, Al addition to the FeCrNiCo HEA, and observed that FeCrNiCoSn HEA has the largest corrosion resistance under the chloride attack. It was seen that the Sn addition lead to the formation of  $\text{SnO}_2$  and  $\text{Cr}_2\text{O}_3$  passive films on the sample surface, thereby leading to better corrosion performance.

Xu et al. (2021) documented that the corrosion resistance of CoCrNiTiMo HEA coating, deposited by double cathode glow discharge method, improved due to the formation of hard  $\text{Co}_2\text{Mo}_3$  intermetallic phase. Aliyu and Srivastava (2021) also investigated the corrosive behavior of electrodeposited AlNiCoFeCu and AlCrNiCoFeCu high entropy alloy coatings in 3.5 wt. % NaCl solution and observed that the corrosive resistance of latter is higher due to the emergence of oxide film on the surface.

Kuptsov et al. (2023) performed the electrochemical corrosion studies on FeCrNiCoCu and FeCrNiCo HEA coated steel substrates in artificial sea water using three electrode cell, and observed that the FeCrNiCo coatings outperformed the steel substrate and FeCrNiCoCu coatings, owing to the formation of Cr based passivation film on the surface. Besides, the authors also noticed the Cu segregation along the interdendritic regions of FeCrNiCoCu HEA coatings, which led to the breakdown of Cr based passivation film, and thereby increased the corrosion rate.

## **2.4 Research gaps**

A review of literature highlights the following research gaps in HEAs

- It was found that High entropy alloys were widely processed as bulk materials using spark plasma sintering and vacuum arc melting techniques. The application of high entropy alloys as coatings to improve the tribological and corrosion performance were limited.

- A thorough investigation of the mechanical alloying parameters, especially the milling time and speed on the phase formation and microstructural evolution has to be studied in detail.
- Research pertaining to the cladding of High entropy alloys to the substrate has been done extensively. However, the studies on high temperature wear behaviour of high entropy alloys coated with HVOF spray technique were minimal.
- The application of refractory materials such as Molybdenum and tungsten in the processing of high entropy alloys were limited. Further, the effect of variation in the molar fraction of molybdenum and tungsten on the mechanical and tribological performance of the high entropy alloys need to be well understood.

## **2.5 Objectives of the study**

- Processing of  $\text{CoCrNiTiMo}_x$  ( $x$ ; molar fraction,  $x=0.5,1,1.5$ ) and  $\text{CoCrNiTiW}_x$  ( $x=0.5,1,1.5$ ) HEA feedstock from pure metal powders to obtain a single or dual phase solid solution using MA.
- Characterization of elemental metal powders and milled powders for purity, phase formation, morphology, particle size and crystallite sizes.
- Thermal spraying of HEA feedstock powder using High velocity Oxy-fuel spray technique on to maraging steel substrate.
- Characterization of  $\text{CoCrNiTiMo}_x$  and  $\text{CoCrNiTiW}_x$  HEA coatings with respect to micro hardness, fracture toughness, microstructure, phase analysis, porosity, surface roughness and Raman spectroscopy.
- Investigation of elevated temperature wear behaviour of  $\text{CoCrNiTiMo}_x$  and  $\text{CoCrNiTiW}_x$  HEA coatings using Pin-on-disc tribometer.

## **2.6 Scope of the research work**

The current study aims to enhance the wear performance of maraging steels, commonly utilized in aircraft landing gear components, which undergo wear and degradation in harsh working conditions. To address this issue, mechanical alloyed  $\text{CoCrNiTiMo}_x$  ( $x$ ; a molar fraction,  $x = 0.5,1$  and  $1.5$ ) and  $\text{CoCrNiTiW}_x$  ( $x$ ; a molar fraction,  $x = 0.5,1$  and  $1.5$ ) HEA powders were employed as feedstock in the development of dense coatings using HVOF. The dry sliding wear behaviour of uncoated substrate and HEA coatings

were extensively investigated at different temperatures and loads using a Pin-on-disc tribometer. The microstructures and phases of the mechanical alloyed powders, deposited coatings and worn surfaces were thoroughly studied. The mechanical properties of the deposited HEA coatings, including the microhardness, fracture toughness and surface roughness were determined. Molybdenum and Tungsten, which are refractory metals, were predicted to enhance the wear behaviour of the HEA. Therefore, the molar fractions of tungsten and molybdenum were varied to analyse its effect on the phase formation, microhardness and wear behaviour. The wear characteristics of the HEA coatings were systematically assessed under varying temperatures and loads, drawing comparisons with the uncoated maraging steel substrate. A comprehensive elucidation of the wear mechanisms inherent in HEAs under diverse testing conditions was provided. The findings hold potential as a benchmark for the strategic deployment of  $\text{CoCrNiTiMo}_x$  and  $\text{CoCrNiTiW}_x$  HEAs in diverse high-temperature scenarios.

## **2.7 Outline of the thesis**

A brief skeletal structure of the thesis along with summary of individual chapters are as given below:

**Chapter 1** begins with the background of the current work and the introduction to high entropy alloys. Subsequently, the core effects of high entropy alloys and their properties were presented. The introduction to mechanical alloying and nanocrystalline materials were also presented thereafter. Lastly a brief discussion on various thermal spray techniques was also presented.

**Chapter 2** presents an extensive literature review of various aspects of high entropy alloys including the different processing methods and coating deposition techniques. Further, the literature documents the functional performance of HEA coatings including the mechanical, tribological and corrosive performance. Based on the literature survey, the research gaps were identified and the objectives were formulated.

**Chapter 3** describes the materials used in the study. The detailed methodology adopted in the current research right from the selection of raw materials to evaluating the

tribological performance was explicitly presented. Further, the various characterization techniques used in the current study were discussed.

**Chapter 4** sheds light on the initial characterization studies of the constituent metal powders to identify the microstructure, purity and particle sizes. Further, the effect of various mechanical alloying process parameters, including the milling time and speed on the phase formation and microstructure evolution of the milled powders was extensively investigated. Finally, an optimal milling time is fixed and the feedstock powders were processed.

**Chapter 5** presents the microstructural and mechanical characterization results of the deposited  $\text{CoCrNiTiMo}_x$  and  $\text{CoCrNiTiW}_x$  HEA coatings. The microstructural characterization has been performed by using XRD, FESEM, EDS, and OM techniques, whereas the mechanical characterization is accomplished by using Vickers microhardness and profilometer.

**Chapter 6** evaluates the specific wear rates and frictional coefficients of  $\text{CoCrNiTiMo}_x$  and  $\text{CoCrNiTiW}_x$  HEA coatings at different temperatures and loading conditions. Moreover, the corresponding wear mechanisms and phases formed at different testing conditions were reported elaborately.

**Chapter 7** highlights the major conclusions from the current research and also sheds light on the scope for future studies.



## CHAPTER 3

### MATERIALS AND METHODOLOGY

#### 3.1 Selection of substrate material

The substrate utilized in the current study is maraging steel 250 grade, which is currently used in rocket motor casings, low temperature tooling, light aircraft landing gear and power shafts. The material has been procured from Chamunda Industries, Mumbai. Optical Emission Spectroscopy technique is used for evaluating and analysing the actual chemical composition of maraging steel in the current research. The nominal and actual compositions of the substrate were reported in Table 3.1.

Table 3.1 Chemical composition (wt. %) of maraging steel 250.

Element	Ni	Co	Mo	Ti	Cr	Al	C	Fe
Nominal	17-19	7-8.5	4.1-5.2	0.3-0.5	0.5	0.05-0.15	<0.03	Bal
Actual	19.5	8.22	3.92	0.51	0.09	0.14	0.04	67

#### 3.2 Selection of feedstock powders

In this study, High entropy alloys (HEA) consisting of transition elements have been selected for enhancing the wear properties of the substrate material.  $\text{CoCrNiTiMo}_x$  ( $x$ ; a molar fraction,  $x = 0.5, 1$  and  $1.5$ ) and  $\text{CoCrNiTiW}_x$  ( $x$ ; a molar fraction,  $x = 0.5, 1$  and  $1.5$ ) HEAs with chemical compositions as mentioned in table 3.2 were chosen as the feedstock for HVOF spray deposition. The selection of  $\text{CoCrNiTiMo}_x$  and  $\text{CoCrNiTiW}_x$  HEA composition is primarily based on the properties of the constituent elements. All the constituent elements in the HEA composition were transition metals possessing higher hardness and melting points. Molybdenum and Tungsten, being refractory metals possessing high hardness and melting point, are anticipated to enhance the wear resistance. Therefore, the molar fraction of Molybdenum and Tungsten were varied and its effect on the phase formation, mechanical and wear behaviour of the HEAs was investigated. The molar fraction of Mo and W used in the current research were 0.5, 1, and 1.5. The molar fractions were selected in such a way

that the effect of the refractory element on the phase formation, microstructure, mechanical and wear performance is clearly understood.

Moreover, the constituent elements possessing similar atomic sizes were considered in designing the HEA, owing to its capability in enhancing the formation of solid solution phases. Furthermore, the thermodynamic parameters of the HEA compositions, including the atomic size difference, enthalpy of mixing, and entropy of mixing were calculated in order to predict the formation of solid solution phases (Zhang et al.). The pure metal powders has been purchased from Sichuan Zhichun New materials technology Co Ltd, Chengdu, China. The properties of the metal powders have been shown in the table 3.3.

Table 3.2 Composition of HEAs used in the current study

S. No	HEA	Atomic %					
		Co	Cr	Ni	Ti	Mo	W
1	CoCrNiTiMo <sub>0.5</sub>	22.22	22.22	22.22	22.22	11.12	-
2	CoCrNiTiMo	20	20	20	20	20	-
3	CoCrNiTiMo <sub>1.5</sub>	18.18	18.18	18.18	18.18	27.28	-
4	CoCrNiTiW <sub>0.5</sub>	22.22	22.22	22.22	22.22	-	11.12
5	CoCrNiTiW	20	20	20	20	-	20
6	CoCrNiTiW <sub>1.5</sub>	18.18	18.18	18.18	18.18	-	27.28

Table 3.3 Properties of the Elemental metal powders

Metal Powder	Atomic number	Density (g/cc)	Crystal structure	Atomic radius (pm)	Melting point (°C)
Cobalt	27	8.86	HCP	135	1493
Chromium	24	7.14	BCC	140	1907
Nickel	28	8.91	FCC	135	1455
Titanium	22	4.50	HCP	140	1668
Molybdenum	42	10.28	BCC	145	2623
Tungsten	74	19.25	BCC	136	3422

### 3.3 Processing of HEAs by MA

Mechanical alloying, a non-equilibrium processing technique, is used for synthesizing the  $\text{CoCrNiTiMo}_x$  and  $\text{CoCrNiTiW}_x$  HEAs. The pure metal powders of Cobalt, Titanium, Nickel, Chromium, Molybdenum and Tungsten possessing different morphologies and particle sizes were taken in a planetary ball mill (Retsch PM 100) according to their compositions, as mentioned in Table 3.2. The selection of the milling media plays a crucial role in contamination. The hardness of the milling media should be considerably higher than the hardness of the powders to be milled. Common milling media includes tungsten carbide, zirconia, stainless steel, or hardened steel.

Tungsten Carbide vial and balls were used in performing the milling process owing to their exceptional hardness and thermal stability. The ball to powder weight ratio was maintained at 10:1 and the milling speed was varied between 200 rpm to 300 rpm to check the effect of milling speed on the alloying rate. The milling was carried out for 50 hours and samples were collected at regular intervals of 10 hours to study the evolution of phases and dissolution of elements in the high entropy alloy. Wet milling is adopted in the current study, using toluene as the process control agent to mitigate the cold welding and agglomeration of powders during the milling process. The ball milling setup is as shown in Figure 3.1.



Figure 3.1 Planetary Ball mill

In mechanical alloying, the process parameters were selected based on the application. Higher milling speeds were selected, if one intends to enable the solid solution formation at an early stage. However, higher milling speeds and ball-to-powder ratios

(BPR) result in drastic reduction of the particle sizes of the milled powders. Further, higher milling speeds also results in contamination from the milling medium. Milling time also plays an important role in the formation of solid solution phases and reducing the contaminants. In order to cater the complete formation of solid solutions during the mechanical alloying of HEAs, longer milling times are required. Nevertheless, extended milling times significantly drops the particle sizes, leading to poor flowability in the nozzle. Therefore enough emphasis has been laid in the current research, in identifying the effect of milling speed and milling time on the alloying rate and particle size of the powders.

### 3.4 Deposition of HEA coatings using HVOF technique

High-velocity oxy-fuel spray (Aum techno spray, Bangalore, India) was employed in the deposition of milled  $\text{CoCrNiTiMo}_x$  and  $\text{CoCrNiTiW}_x$  HEA powders in order to achieve dense coatings with better mechanical properties. The HVOF process relies on the synergy of thermal and kinetic energy transfer, to achieve the desired microstructures. Within the HVOF process, powder is introduced into a gun's flame and propelled onto a substrate through the combustion reaction of various gases, leveraging high velocity and temperature. The schematic of HVOF process is presented in Fig. 3.2.

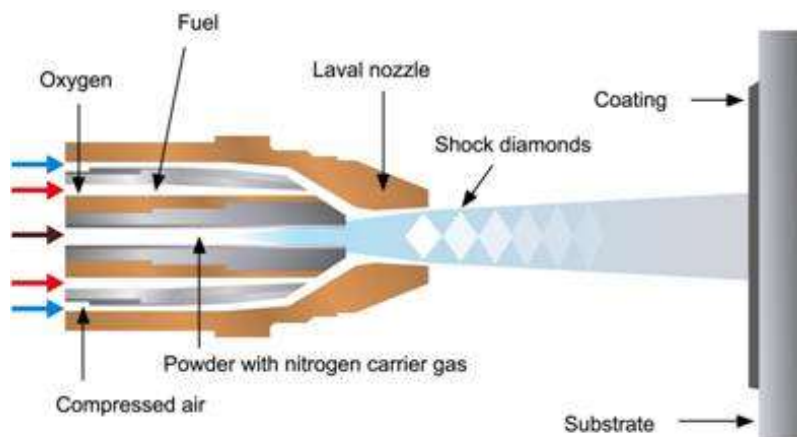


Figure 3.2 Schematic of HVOF spray (Harith et al. 2018)

Retaining the phases, which were formed in the milling stage, even after the coating deposition requires careful control of various parameters to prevent phase transformations, oxidation, and other detrimental effects that could alter the phases. The

flame temperature has to be carefully controlled, so as to generate enough heat just to melt the powders. Further rise in flame temperatures eventually leads to phase transformations. Therefore enough emphasis has to be laid in deciding the process parameters. Optimal spray distance (typically 150-300 mm) has to be maintained, to ensure the particles reach the substrate at the correct temperature and state (semi-molten or fully molten). Too close may cause excessive heating, while too far may cause cooling and improper adhesion. Moreover, using powders with narrow particle size distribution (typically 15-45 microns) ensures uniform melting and deposition. Further, utilizing inert gas shielding (e.g., argon) during spraying also minimizes oxidation.

The process parameters used in the relevant studies utilising HVOF spray have been studied and adopted in the current research (Bolelli et al. 2019; Prasad et al. 2019). The deposited coatings were subjected to trial characterization studies to assess the quality of coatings. The coating thickness, porosity and cross-sectional microstructures were studied in detail. Based on the characterization studies, the process parameters were finalized and all the six compositions were deposited. Table 3.4 displays the process parameters utilized during the coating deposition. The substrate preparation which includes surface cleaning, surface roughening, and preheating enables the better interlocking of the molten splats onto the substrate surface. Grit blasting is widely preferred by many researchers, as it enhances the surface roughness, which is very much desirable for mechanical bonding of the spray particles with the substrate. The feedstock powders were preheated to 150 ° for 1 h, in order to remove the moisture content and enhance flowability in the spray nozzle.

Table 3.4 Process parameters used in HVOF

Parameters	Values
Oxygen (flow rate)	225 lpm
Hydrogen (flow rate)	550 lpm
Nitrogen (flow rate)	45 lpm
Powder feed rate	20 g/min
Spray distance	250-300 mm
Thickness/ pass	15-18 microns

### 3.5 High temperature tribological performance

Dry sliding wear tests were performed on the  $\text{CoCrNiTiMo}_x$  and  $\text{CoCrNiTiW}_x$  HEA coatings using Pin-On-disc tribometer (Ducom instruments, India), in accordance with ASTM G99 standards. Dry sliding wear provides insights into the potential for adhesion, abrasion, and other wear mechanisms that might be prevalent in applications where lubrication is not present. Furthermore, dry sliding wear tests were particularly relevant in cases where the use of lubricants is impractical or undesirable. Alumina counter disc is used in the current research, owing to its higher hardness. High hardness implies good resistance to wear and the ability to withstand abrasive nature of the sliding contact. Additionally, alumina's excellent thermal stability and chemical inertness resists chemical reactions and degradation despite the heat generated during sliding contact, thus ensuring highly reliable and reproducible results. The experimental setup used for the tribological testing is presented in Figure 3.3.



Figure 3.3 Pin-on-disc tribometer used for tribological testing

Cylindrical specimens coated on one face, possessing a diameter of 12 mm and length of 30 mm were used in wear testing. The as-sprayed coated samples possessing higher surface roughness were brought down to  $1 \mu\text{m}$  by carefully polishing the surface. The frictional and wear behavior of the HEA coatings were extensively studied by varying the temperatures and normal loads. The testing parameters were clearly outlined in

Table 3.5. The typical sliding velocity of maraging steel components, widely used in the aerospace landing gear vary from 0.1 to 2 m/s. Further the temperatures attained by them may vary from ambient to elevated temperatures. Therefore, the process parameters in the current study were selected in such a way, so as to mimic the actual conditions. Moreover, the temperature rise of the interphase post wear testing due to the frictional heat is also analyzed by using a digital laser infrared non-contact thermometer. The rise in temperature of the interface depends on several factors including the sliding distance, sliding speed and sliding pairs used.

Table 3.5 Parameters used for Pin-On-disc tribometer

Parameters	Value
Counter disc	Alumina (165 mm diameter, 6 mm thickness)
Normal load	2 kg and 4 kg
Sliding velocity	1.5 m/s
Wear track diameter	120 mm
Temperature	25 °C , 200 °C, 400 °C and 600 °C
Sliding distance	2000 m

During the wear test, the frictional forces were continuously monitored by a load cell securely attached to the Pin-on-disc apparatus. A chamber heating module was used for conducting the high-temperature wear studies. Each experiment was performed thrice, and the average value was considered to ensure repeatability and accuracy. The specific wear rates of the HEA coatings and substrate were determined using Eq. 3.1 (Nguyen et al. 2022). The wear volume (V) is calculated after measuring the mass loss and density of the samples (Eq. 3.2) (Parthasarathi i Duraiselvam 2010). The mass loss is determined by weighing the samples before and after wear testing, using an electronic weighing balance with 0.1 mg accuracy. The density of coating is determined using the Eq. 3.3.

$$W = \frac{v}{L \times S} \quad (3.1)$$

$$V = \frac{m}{\rho} \times 1000 \quad (3.2)$$

$$\rho = \rho_1 \left( \frac{m_a}{m_a - m_1} \right) \quad (3.3)$$

W is the specific wear rate in mm<sup>3</sup>/N-m, V denotes the volumetric wear in mm<sup>3</sup>, L is the load in N, and S is the sliding distance in meter,  $\rho$  is the density of coating in g/cm<sup>3</sup>, m is the mass loss in g.  $\rho_1$  corresponds to the density of water (1 g/cm<sup>3</sup>) at room temperature,  $m_a$  is the weight of the coating in the air (g), and  $m_1$  is the weight of coating in water (g).

### **3.6 Characterization of milled powders**

#### **3.6.1 XRF analysis of elemental powders**

X-ray fluorescence analysis has been carried out on the constituent metal powders to ensure their purity and to check the percentage of trace elements present in the composition.

#### **3.6.2 SEM and EDAX analysis**

The surface characteristics and elemental composition of both the individual metal powders and milled powders at various milling durations were analyzed using Field Emission Scanning Electron Microscopy (Carl ZEISS-GeminiSEM) coupled with Energy Dispersive Spectroscopy (EDS).

#### **3.6.3 XRD analysis**

The crystal structure and phase changes in the milled powders across different milling durations were examined using an XRD (Malvern-Empyrean) equipped with a Copper source ( $\lambda = 1.5405 \text{ \AA}$ ) in the  $2\theta$  range of 30° to 105°. The scanning process involved a step size of 0.026° and a time per step of 27.54 seconds. The X'pert High score software was employed to analyze the XRD profiles for phase identification. The crystallite size and lattice strain of the milled powders were determined from the XRD data using the Williamson-Hall approach.

#### **3.6.4 Particle size analysis**

The particle size distributions of the milled powders at various milling times were identified by laser diffraction method using CILAS 1064 particle size analyzer. In order to have a good flow ability and deposition efficiency of coatings, the particle size of the feedstock powders should be of the range 5-45 microns.

### **3.7 Characterization of deposited coatings**

#### **3.7.1 Specimen preparation for cross-sectional analysis**

A precision sectioning saw from Ducom Instruments Pvt. Ltd, Bangalore is utilized to cut the specimens, prior to the microstructural and mechanical characterization. Subsequently, the samples were mounted and polished down to 2000 grit. In the last phase, the specimens underwent mirror polishing on a cloth wheel polishing machine, utilizing 0.5 $\mu$ m alumina powder suspensions for a refined surface. Thereafter, the specimens were ultrasonically washed using acetone and dried in hot air

#### **3.7.2 Microstructural analysis**

The surface morphology and cross-sectional microstructure of the deposited coatings were extensively investigated by using a SEM equipped with EDS. Backscattered electron mode is utilised for analysing the cross sections, whereas secondary electron mode is preferred for analysing the surface morphologies of coated samples. Elemental mapping of the coated samples was further performed to identify the distribution of constituent elements in the microstructure.

#### **3.7.3 XRD analysis**

The phase composition of the as-sprayed coatings was found using an x-ray diffractometer (Malvern PANalytical, Netherlands) using Cu source ( $\lambda = 1.5403 \text{ \AA}$ ). Scanning was performed in the range of 20° to 105°, and a step size of 0.027° with a duration of 28 s per each step was employed during the test. The phases were identified and indexed using the ICDD-PDF 2 database in Xpert high score plus software.

#### **3.7.4 Coating thickness**

The thickness of the HEA coatings were monitored during the HVOF deposition using Minitest-2000 thin film thickness gauge. Further, to verify the thickness of the as-sprayed coatings, high resolution images were taken along the cross-section using back scattered electron mode in Scanning Electron Microscope.

#### **3.7.5 Porosity and density**

An optical microscope (Zeiss Axiovert, Germany) with ImageJ software was used to measure the coatings' porosity at its cross sections following ASTM B276 guidelines. The density of coatings was calculated using a pycnometer, following the guidelines

outlined in the ASTM C135 standard. The deposited coatings were peeled off manually by hammering at the cross section. A minimum of 2 g of sample was peeled off to determine the density of coatings.

### **3.7.6 Micro hardness**

The coated samples' microhardness values were evaluated according to ASTM E384 standards, using a Vickers indenter (Omnitech, India). The polished cross-sections of the coated samples were subjected to indentations by applying a load of 300 g for a dwell time of 10 s. Several measurements were taken along the thickness direction from the substrate to the coating surface. The experiments were repeated thrice and average of the three values were considered for determining the microhardness.

### **3.7.7 Fracture toughness**

The fracture toughness of the coatings was determined by using a Vickers indenter on the cross-section of the coating. Multiple indents were taken on the coatings cross section, and toughness value is determined by measuring the lengths of cracks that originated from the corners of the indent. However, the magnitude of fracture toughness was determined by using the Evans and Wilshaw's empirical equation (Eq. 3.4). (Evans i Wilshaw 1976). Determination of fracture toughness of coatings by employing Evans and Wilshaw's approach is well established in the literature (Lin et al. 2015; Ndumia et al. 2023). The test was performed by applying a normal load of 19.62 N and dwell time of 10 s. An optical microscope was used to analyse the length of radial cracks generated from the indentation corners.

$$K_{IC} = 0.079 \left( \frac{P}{a^{3/2}} \right) \log \left( \frac{4.5a}{c} \right) \quad (3.4)$$

Where  $K_{IC}$  is the fracture toughness, P is the load applied on the indenter, 'a' is the half average length of the diagonal of Vickers marks, and 'c' is the average length of cracks obtained in the tips of the Vickers marks.

### **3.7.8 Surface Roughness**

The Surface roughness profile of the coated samples was determined using a 3D Non-contact profilometer (Nanovea, ST400, USA). The coated samples were scanned in a 5mm × 5mm area and 2D line profiles were taken at specific locations.

## **3.8 Characterization of worn samples**

### **3.8.1 SEM analysis**

The wear mechanisms of HEA coatings at different temperatures were identified by analyzing the worn surfaces using the secondary electron imaging mode in FESEM. The chemical compositions of the worn surfaces at different regions were studied by EDS and elemental maps.

### **3.8.2 XRD analysis**

XRD analysis has been performed on the worn surfaces of CoCrNiTiMo<sub>x</sub> and CoCrNiTiW<sub>x</sub> HEA coatings at different test temperatures to identify the phase transformations. Scanning was performed in the range of 20° to 105° and ICDD-PDF2 database is utilized in identifying and indexing the formed phases.

### **3.8.3 Raman spectroscopy**

The Oxide formation at a temperature of 600 °C was studied using a Confocal Raman spectrometer (Renishaw, UK). Raman spectroscopy is an effective analytical tool to characterize the worn surfaces and identify the formed oxide phases. Multiple researchers have employed Raman spectroscopy to discern the emergence of oxide phases (Guo et al. 2019; Miao et al. 2021). Raman spectroscopy is highly sensitive to the vibrational modes of molecules. Each oxide phase has a unique set of vibrational frequencies that appear as distinct peaks in the Raman spectrum, effectively serving as a molecular fingerprint. By comparing the observed Raman spectrum with reference spectra of known oxide phases, specific oxides can be accurately identified. A 50 mW laser with an excitation wavelength of 532 nm and a 50× objective lens was used. The range of Raman shift is taken from 100-1200 cm<sup>-1</sup>, and an exposure time of 20 s is adopted for characterizing the sample.

## **3.9 Summary**

The detailed flow chart describing the methodology adapted in the current research is presented in Figure 3.4. The sequence of steps right from the selection of raw materials to evaluating the tribological performance of the deposited coatings was elaborated.

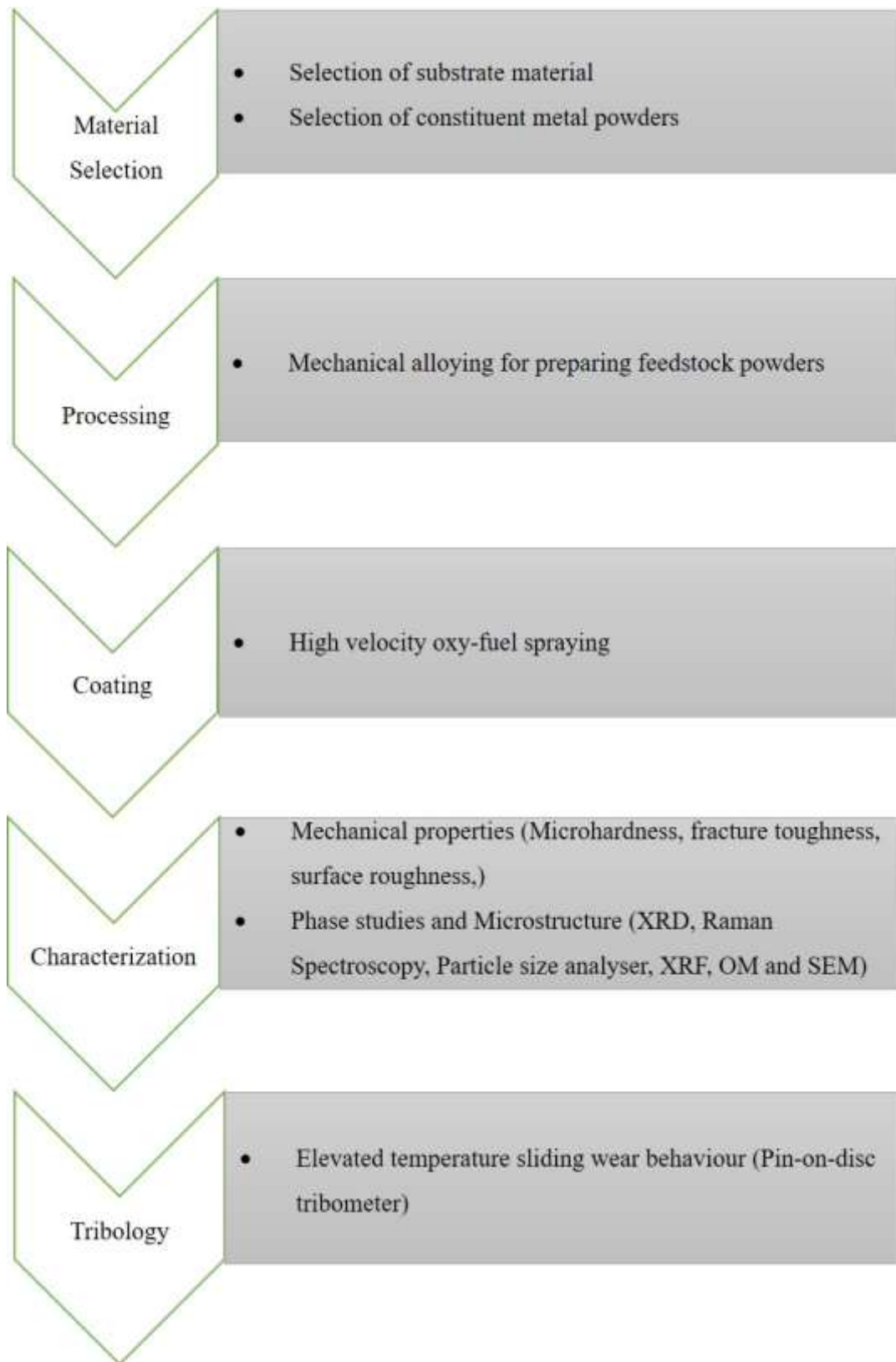


Figure 3.4 Methodology of the research work

## CHAPTER 4

### PROCESSING OF HIGH ENTROPY ALLOYS

#### 4.1 Characterization of pure metal powders

The elemental metal powders were initially characterized before ball milling to determine their microstructure, purity, and crystal structure using SEM, XRF, and XRD. The surface morphology of the elemental powders had been studied using the scanning electron microscope (Figure 4.1), and it's evident that most of the powders are flaky and non-spherical subject to their processing methods. X-ray Fluorescence (XRF) analysis has been performed to ensure the purity of metal powders. The results reveal that all the metal powders are highly pure with impurities less than 0.5% in each metal powder, as mentioned in Table 4.1.

The qualitative analysis of the elemental powders has been done by using X-ray diffraction (Figure 4.2). The corresponding peak locations of the elemental powders has been identified and validated with that of the standard ICDD database. The crystallite size is calculated by Debye-Scherrer law (Murali et al. 2016) (Eq. 4.1) and the crystal structure of the particular elemental powder is determined from the peak positions, using the X-ray diffraction data (Table 4.1). It has been observed that the crystallite sizes of all the metal powders differ reasonably, varying from 41 nm to 265 nm, as indicated in Table 4.1. It is also evident that cobalt, chromium and nickel metal powders possess a nanocrystalline structure, before the start of ball milling. Elements possessing a crystallite size less than 100 nm were termed as nanocrystalline materials.

$$\text{Crystallite size } (d) = k\lambda/B \cos \theta \quad (4.1)$$

Where k is a constant =0.94,  $\lambda$ = wavelength of Cu-K $\alpha$  = 1.5406 Å B= FWHM, 2 $\theta$  is the diffraction angle.

Table 4.1 Characterization of as-received metal powders

S. No	Element	Avg. particle size ( $\mu\text{m}$ )	Purity (at. %)	Crystal Structure	Crystallite size (nm)
1	Cobalt	72	99.80	FCC	50.70
2	Chromium	44	99.50	BCC	41.72
3	Nickel	42	99.50	FCC	34.90
4	Titanium	48	99.99	HCP	264.04
5	Molybdenum	61	99.90	BCC	265.60
6	Tungsten	56	99.90	BCC	232.50

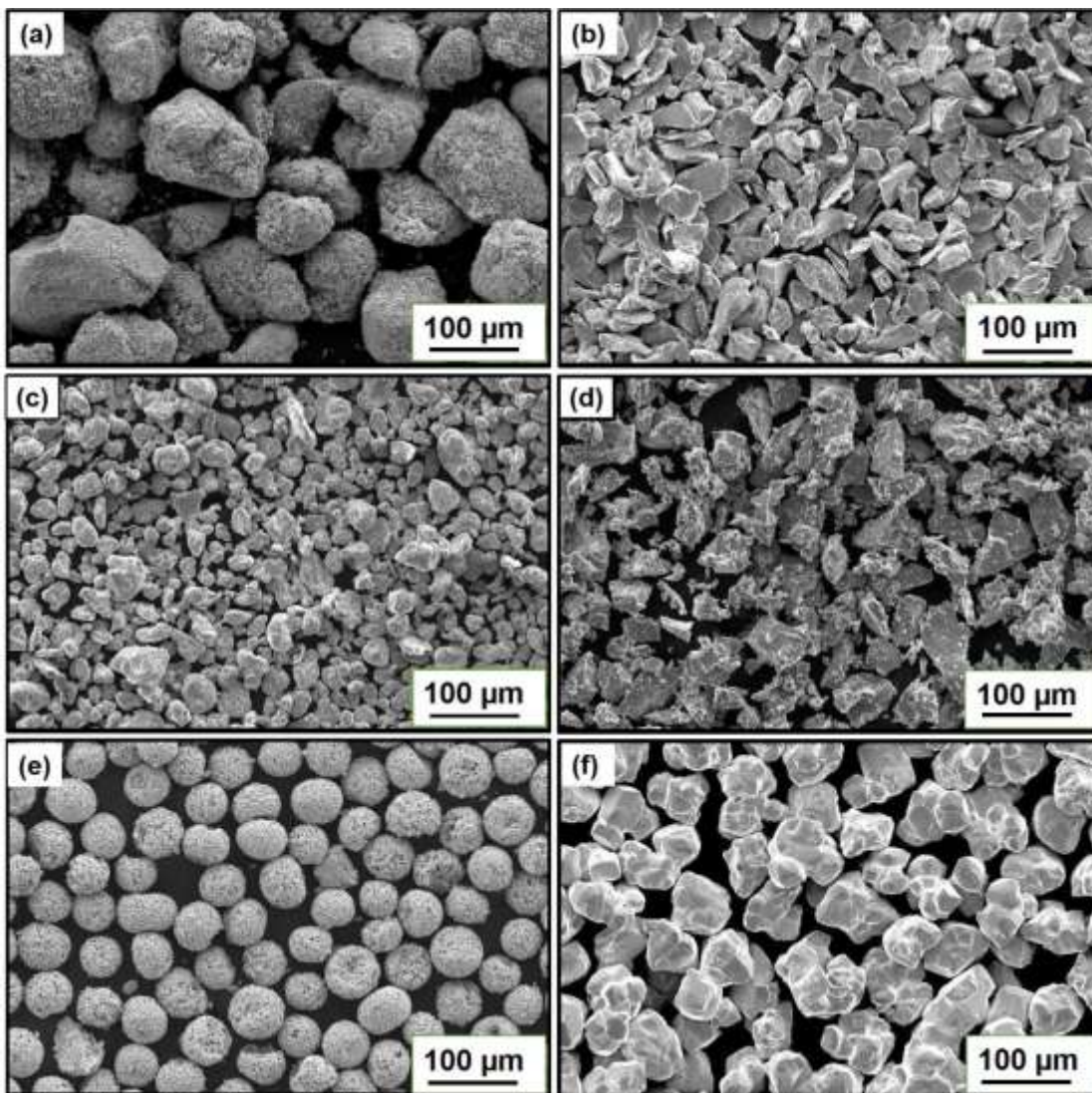


Figure 4.1 Surface morphology of metal powders; (a) Cobalt (b) Chromium, (c) Nickel, (d) Titanium, (e) Molybdenum and (f) Tungsten.

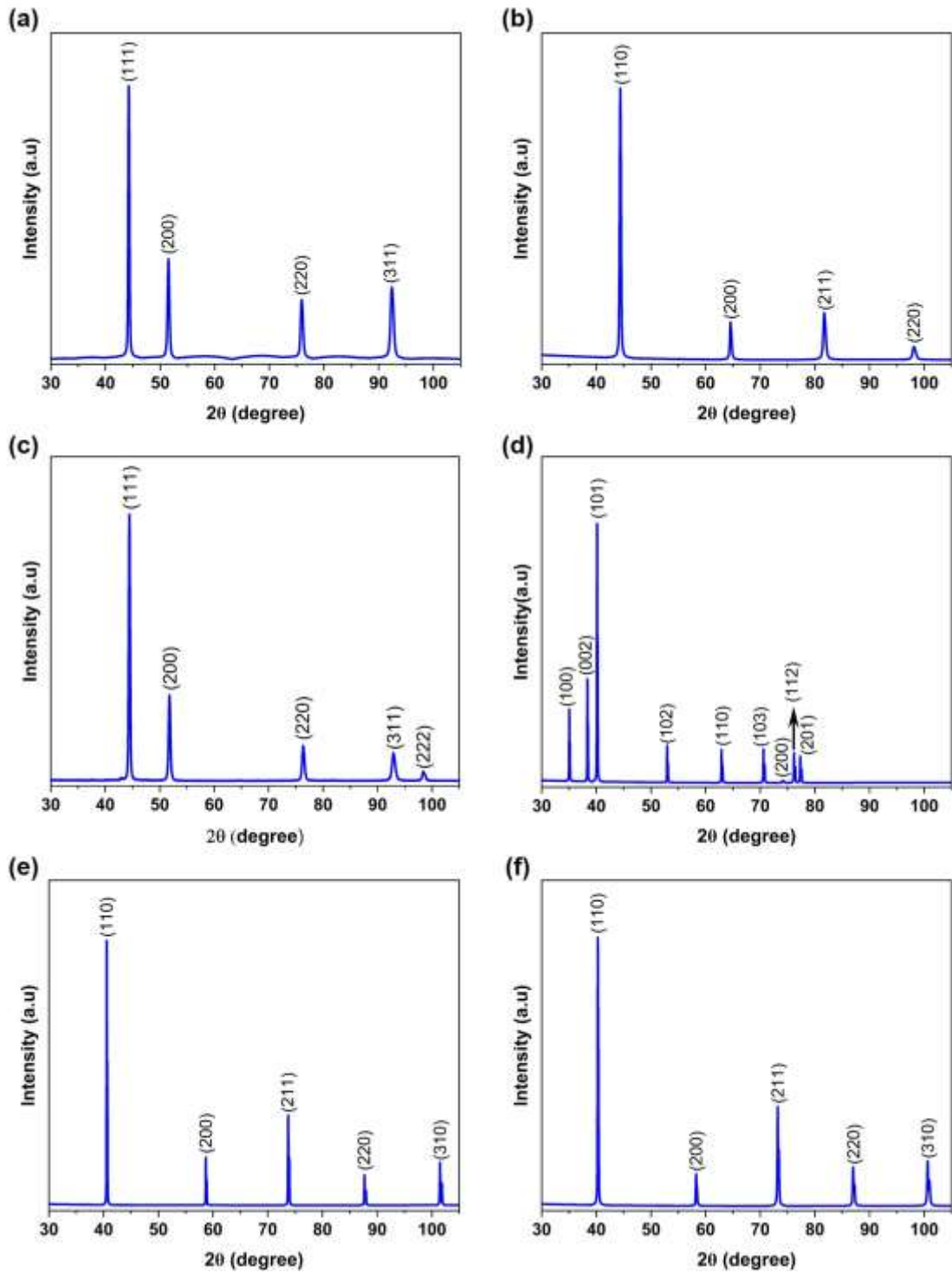


Figure 4.2 X-ray Diffraction of pure metal powders; (a) Cobalt (b) Chromium, (c) Nickel, (d) Titanium, (e) Molybdenum and (f) Tungsten.

## 4.2 Processing of CoCrNiTiMo HEAs by Mechanical Alloying

### 4.2.1 Phase evolution of ball milled powders

XRD patterns of CoCrNiTiMo HEA milled powders for different durations are shown in Figure 4.3(a&b). Before ball milling all the metal powders are thoroughly mixed and characterized for phases. In the X-ray diffraction graph, all the peaks corresponding to individual metals i.e. cobalt, chromium, nickel, titanium, and molybdenum are evident. The mechanical alloying process is carried out to know the effect of ball milling speed and alloying rate on the phase evolution of high entropy alloy powder with respect to milling time. Figure 4.3(a) shows the XRD patterns of CoCrNiTiMo HEA powder milled at 200 rpm. Before the start of the ball milling, all the peaks corresponding to pure metal powders are observed. After 10 hours of mechanical alloying, most of the Titanium and Cobalt peaks started diffusing into the lattice. The rate of diffusion of the elements into the lattice depends on the melting point of the particular elements (Chen et al. 2009). Elements with lower melting points have a higher tendency to diffuse into the lattice at a faster rate. Chen et al. (Chen et al. 2009) has observed that metals with higher melting point possess high bonding strength and low self-diffusion coefficient and hence these elements results in a lower alloying rate. After 20 hours, all the titanium and cobalt peaks are completely dissolved into the lattice.

As the ball milling is prolonged further to 30 hours, a noticeable drop in the peak intensities of Nickel at (2 0 0), (2 2 0) can be observed besides broadening of peaks. The decrease in the intensity of peaks indicates that the peaks are slowly dissolving into the matrix; the broadening of peaks indicates the reduction of crystallite size and the increment of lattice strain. Also, with the prolonging of milling time, the most intense peak of Molybdenum (1 1 0) move towards lower angles, indicating the change in the lattice parameter of Mo. The Mo (1 1 0) peak at 40.48 degrees at the start of the milling shifts to 40.46 and 40.41 degrees at 20, 30 hours respectively. This indicates the increase of the Mo lattice parameter, owing to the diffusion of other elements into the Mo lattice (Chen et al. 2009). The lattice parameter of Mo increases from 3.149Å at the start to 3.153Å by the end of 30 hours of milling. As milling reaches 40 hours, all the nickel peaks are completely dissolved. This indicates that by 40 hours, all the peaks corresponding to cobalt, titanium, and nickel have been completely dissolved into

molybdenum and chromium lattice sites. Here, molybdenum and chromium act as solvents and dissolve all other elements, leading to solid solution formation. On further extending the milling time to 50 hours, two BCC solid solution phases with lattice parameters  $a = 3.148 \text{ \AA}$  (BCC1) and  $a = 2.883 \text{ \AA}$  (BCC2) have been formed without the formation of any intermetallic compounds.

Figure 4.3(b) shows the XRD patterns of CoCrNiTiMo HEA powder milled at 300 rpm. At 300rpm milling speed, because of the higher energy of the system, the impact of the balls onto the powders is significantly high. The powder particles are continuously trapped in between the balls and the vial and are subject to more severe plastic deformation. Hence the dissolution of the metal powders into the lattice sites starts much earlier at higher speeds. The diffusion of titanium and cobalt peaks starts well before 5 hours of milling, and by the end of 10 hours of milling all the titanium, cobalt and nickel peaks have been completely diffused into the lattice sites of molybdenum and chromium. The X-ray diffraction pattern at 10 hours of milling indicates the start of the solid solution phase formation. On milling beyond 15 hours, a new phase can be witnessed. The intensity of the new peaks increases with milling time and it can be observed that this new phase is the WC contamination from the milling media. After 30 hours of milling, two BCC solid solution phases with WC contamination phase can be observed.

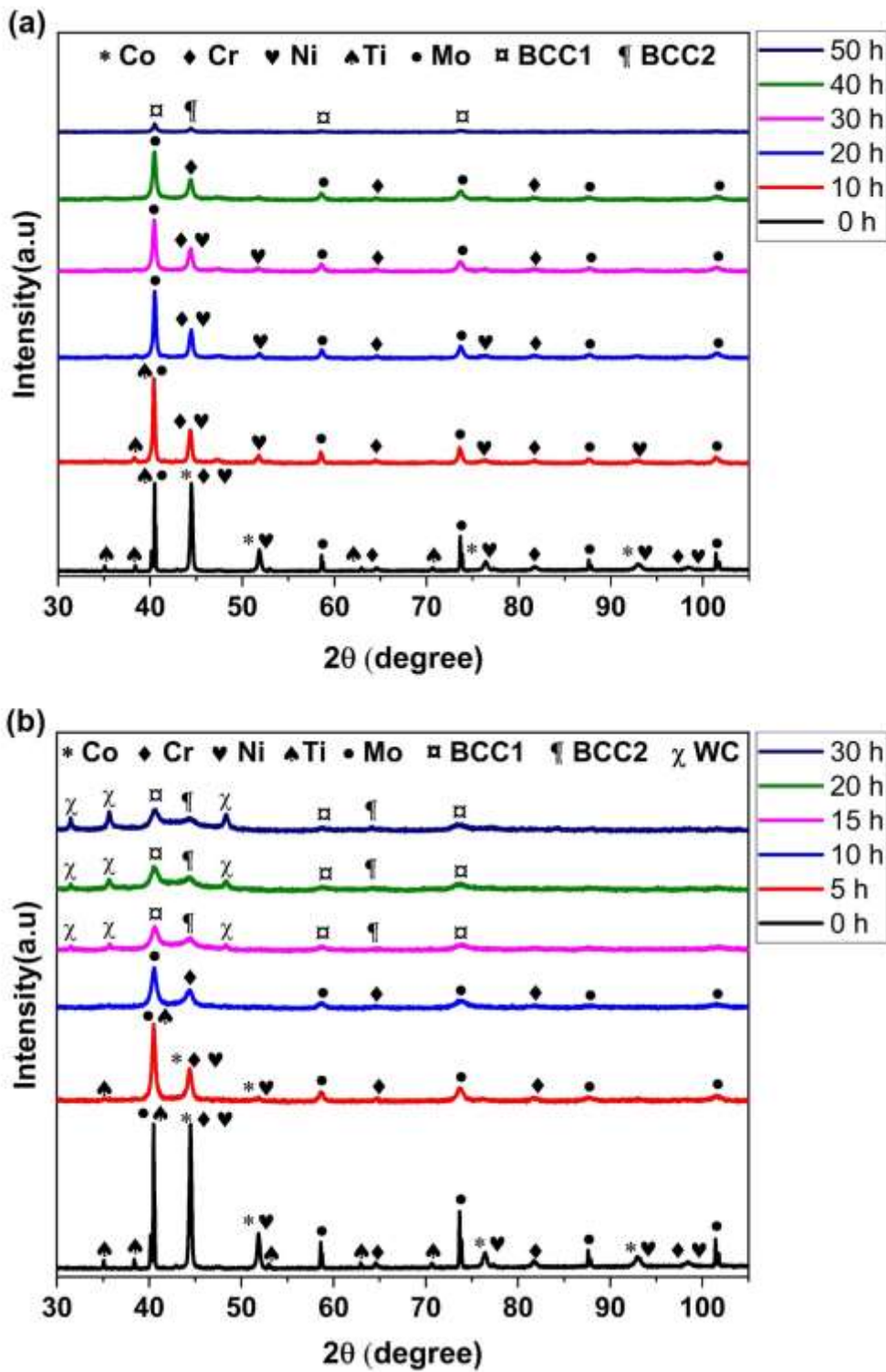


Figure 4.3. XRD of CoCrNiTiMo HEA powders at different milling times using a speed of (a) 200 rpm and (b) 300 rpm.

#### 4.2.2 Calculation of crystallite size and lattice strain

In the mechanical alloying process, high impact energy is induced from the balls and vial to the powders and because of this, the metal powders were subjected to continuous grain refinement and rise in lattice strain. It is important to calculate the crystallite size and lattice strain at regular intervals to know the effect of ball milling. Crystallite size can be calculated either by the Debye-Scherrer method or the Williamson-Hall method. Williamson-Hall method considers the effect of lattice strain on peak broadening of XRD data and it gives effective results compared to the former method. Crystallite size and lattice strain can be calculated from the peak locations and FWHM values by using the Eq. 4.2 (Gupta et al. 2016). The instrumental effects in the peak broadening of the XRD data have been eliminated by running a standard Si sample on the X-ray diffractometer and following Eq. 4.3.

$$B \cos \theta = K\lambda/L + 4\eta \sin \theta \quad (4.2)$$

$$B = \sqrt{B_o^2 - B_i^2} \quad (4.3)$$

Where  $\theta$  is the Bragg angle, B is corrected FWHM values at corresponding peak locations of  $\theta$ , after considering the instrumental broadening,  $\lambda$  is the wavelength of the XRD source,  $\eta$  is strain in the material and K is dimensionless shape factor and L is the crystallite size.  $B_i$  is the FWHM value corresponding to the standard 'Si' sample.  $B_o$  is the observed FWHM values at corresponding peak locations.

A comparative study has been made for the mechanically alloyed powder by varying speed to select the optimal process based on the phase evolution and crystallite size. Crystallite size and lattice strain calculations were made on the ball milled samples at regular intervals of 10 hours. For the CoCrNiTiMo HEA milled at 200 rpm, the complete formation of solid solutions is seen at 50 hours, whereas for powders milled at 300 rpm, the solid solution formation is evident at 30 hours itself. Based on the Williamson-Hall plot, crystallite size and lattice strain calculations have been made and shown in Table 4.2. Figure 4.4 shows the Williamson-Hall plot for the milled powders at 200 rpm at two different time frames 10 hours and 50 hours.

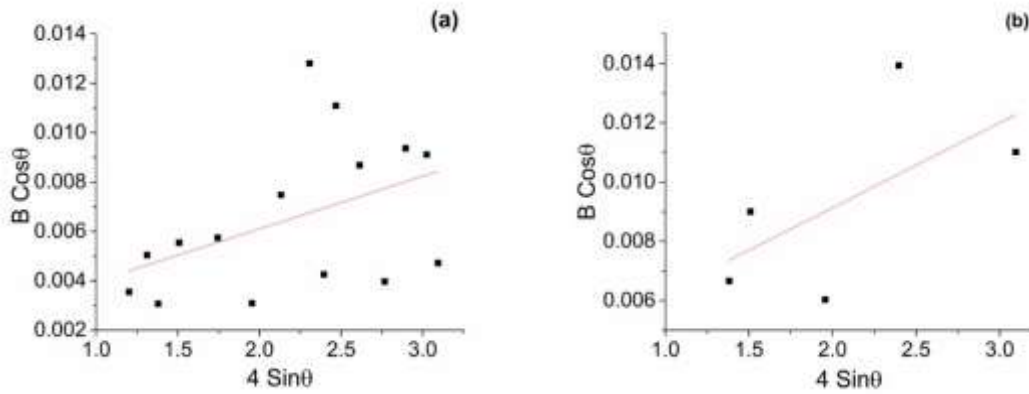


Figure 4.4 Williamson- Hall plots of CoCrNiTiMo ball milled powders at 200 rpm (a) 10 h and (b) 50 h

Table 4.2 Crystallite size and lattice strain of CoCrNiTiMo Ball milled powders

Milling time (h)	Crystallite size (nm)		Lattice strain (%)	
	200 rpm	300 rpm	200 rpm	300 rpm
0 h	124	124	0.187	0.187
10 h	78.7	14.83	0.213	0.49
20 h	66.7	4.71	0.208	0.50
30 h	64.07	3.42	0.319	0.87
40 h	50.4	-	0.303	-
50 h	46.2	-	0.415	-

From Table 4.2, it is observed that the crystallite size of the CoCrNiTiMo powders milled at 200 rpm, steadily decreased with respect to time. At the beginning of the milling, the blended powders possessed a crystallite size of 124 nm, thereafter the crystallite size gradually reduced to 46 nm at the end of 50 hours of milling. When the ball milling is carried out at 300 rpm, the reduction in crystallite size is significantly high and it drops drastically from 124 nm to 3 nm after 30 hours of milling.

Further, it can also be seen that the lattice strain of the milled powders gradually increases from 0.187% to 0.415% at the end of 50 hours of milling in the case of CoCrNiTiMo HEA milled at 200 rpm. In the case of powders milled at 300 rpm, the lattice strain values increase significantly with milling time and it reached to 0.87% at the end of 30 hours of milling. The noticeable rise in the lattice strain is due to the inherent nature of the mechanical alloying process. The ball milling process induces strain in the lattice of the milled powders because of the continuous interaction and

intense plastic deformation of the powders with the milling media. In all the two cases, it was observed that the decrease in the crystallite size is significant in the initial hours with a noticeable rise in the lattice strain. This explains that the rate of diffusion of the elements into the host lattice is higher at the start of milling (Chen et al. 2015b; Wang et al. 2014a).

#### **4.2.3 Microstructural evolution of milled powders**

SEM morphology of the CoCrNiTiMo high entropy alloy milled at 200 rpm is presented in Figure 4.5 (a-f) at different milling times i.e. 0, 10, 20, 30, 40, 50 hours of milling. Before starting the milling process, the blended powders have an irregular morphology with different shapes because of the distinct processing techniques used in synthesizing the pure metal powders (Figure 4.5a). After milling the powders for 10 hours, because of the entrapment of the powders in between the balls and the vial, the particles are flattened initially, as can be witnessed from Figure 4.5(b). On continuing the milling further up to 20 hours, the flattened powders can be seen cold welded to each other slightly as seen in Figure. 4.5(c). The extent of cold welding is reduced here because of the wet milling environment due to the presence of Toluene as a process control agent. Milling up to 30 hours results in the fracturing of the cold welded particles, leading to refinement of the milled high entropy powders. From figure 4.5(d), it can be seen that most of the particles fall under 10 microns of size, indicating particle size reduction. By milling beyond 40 hours, a significant decrease in particle size can be seen, and the particles tend to be near-spherical (Fig 4.5e). Milling until 50 hours, results in the further reduction in particle size as can be witnessed in Figure 4.5 (f).

The chemical compositions of the constituent elements of CoCrNiTiMo milled for 50 hours at 200 rpm has been determined by Energy dispersive Spectroscopy and shown in Figure 4.6. The expected compositions were named as ideal and the experimental composition were reported as observed values in Fig 4.6. Due to the intense plastic deformation and thorough mixing of the constituent elements in the vial during the mechanical alloying process, the composition slightly changes. The authors tried to compare the ideal compositions before mechanical alloying with the observed experimental compositions post mechanical alloying. It can be observed that the

expected and observed compositions of all the elements are close to each other with a variation of 1-3%, indicating excellent chemical homogeneity of the milled powders.

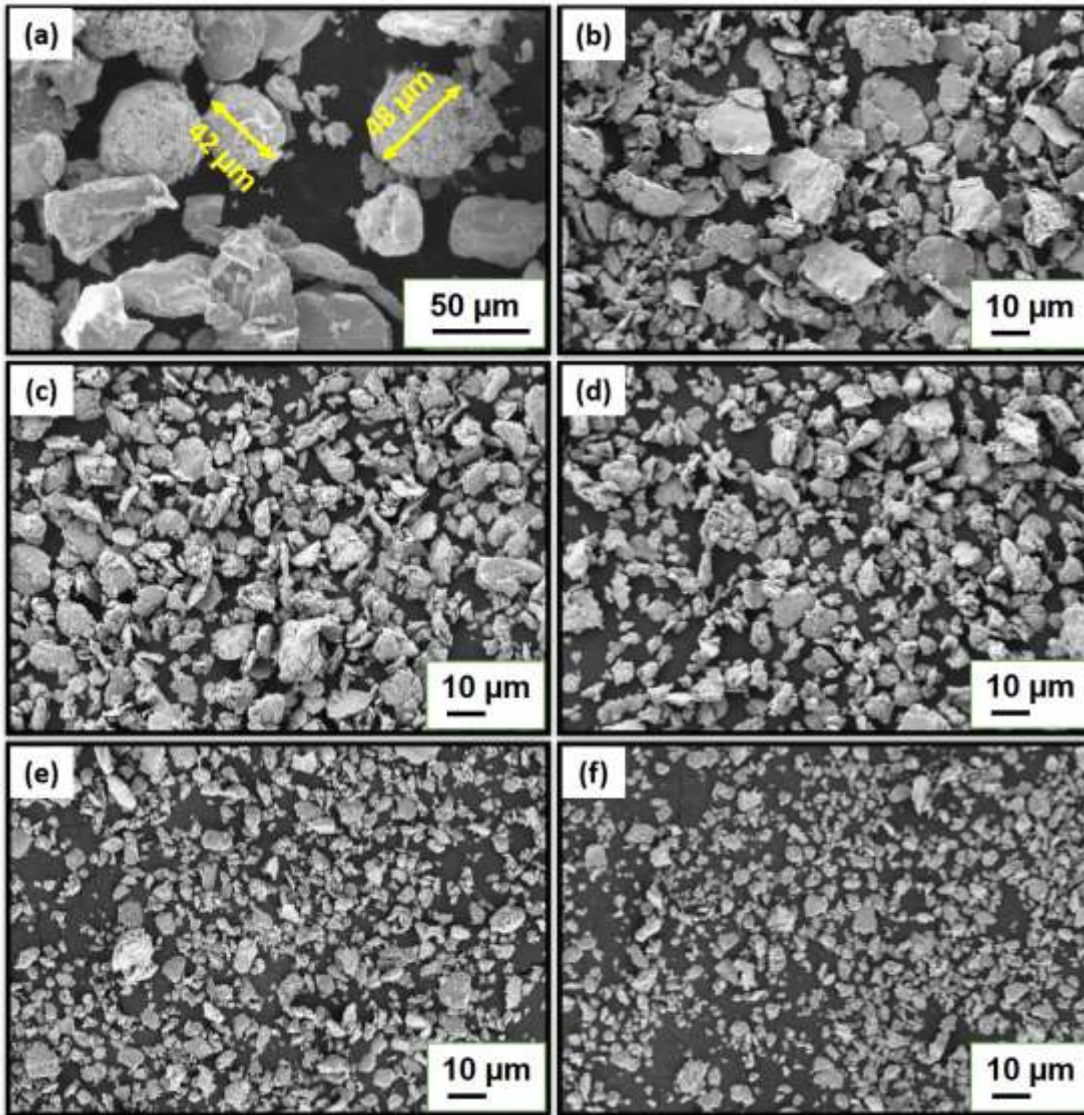


Figure 4.5 Microstructural evolution of CoCrNiTiMo HEA powders after milling for a) 0 h b) 10 h c) 20 h d) 30 h, e) 40 h, and f) 50 h.

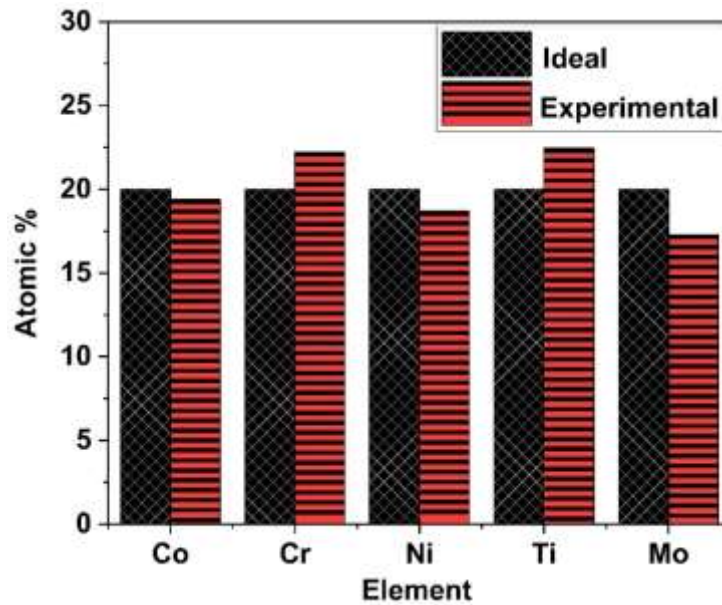


Figure 4.6 Chemical composition of CoCrNiTiMo milled at 200 rpm for 50 hours

#### 4.2.4 Particle size analysis

The evolution of the particle size for CoCrNiTiMo HEA powders milled at 200 rpm has been shown in Figure 4.7. It can be seen that initially after 10 hours of milling, the particle size is 24 microns and the span is diverse ranging from 2-90 microns, with 90% of the particles falling under 50 microns. On continuing the milling process further, the particle size reduces and the range of particle size distribution becomes narrow. After 50 hours of milling, the average particle size and the range of distribution are 6 microns and 1-20 microns respectively. The effect of milling speed on the particle size evolution can be seen in Figure 4.8. It is evident from Figure 4.8 that the particle size reduction rate is higher with the increase in the milling speed. This is due to the intense plastic deformation experienced at higher speeds. At 300 rpm milling speeds, the average particle size reduces to 5.5 microns, after 30 hours of milling with a range of 0.5-20 microns.

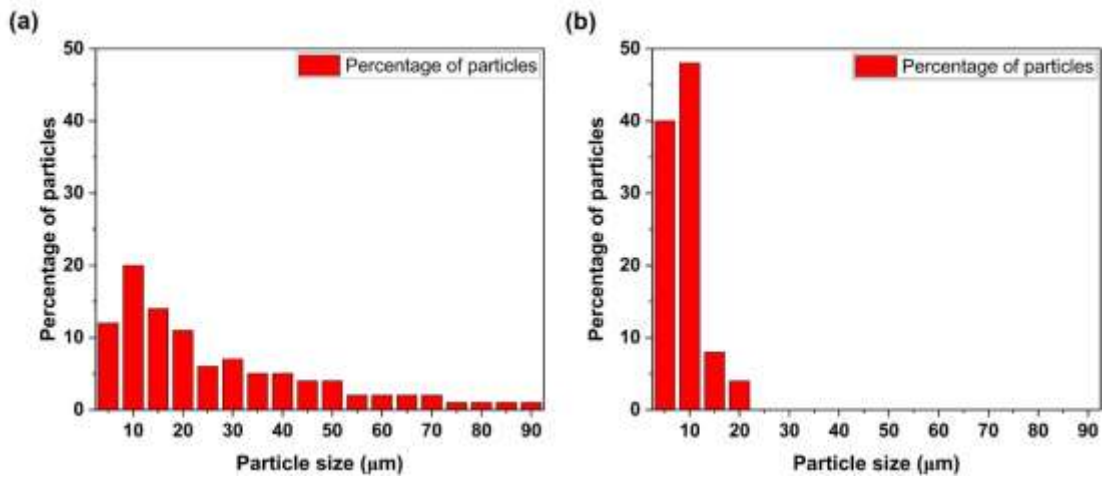


Figure 4.7 Particle size distribution of CoCrNiTiMo HEA powders milled for a) 10 h and b) 50 h at a milling speed of 200 rpm.

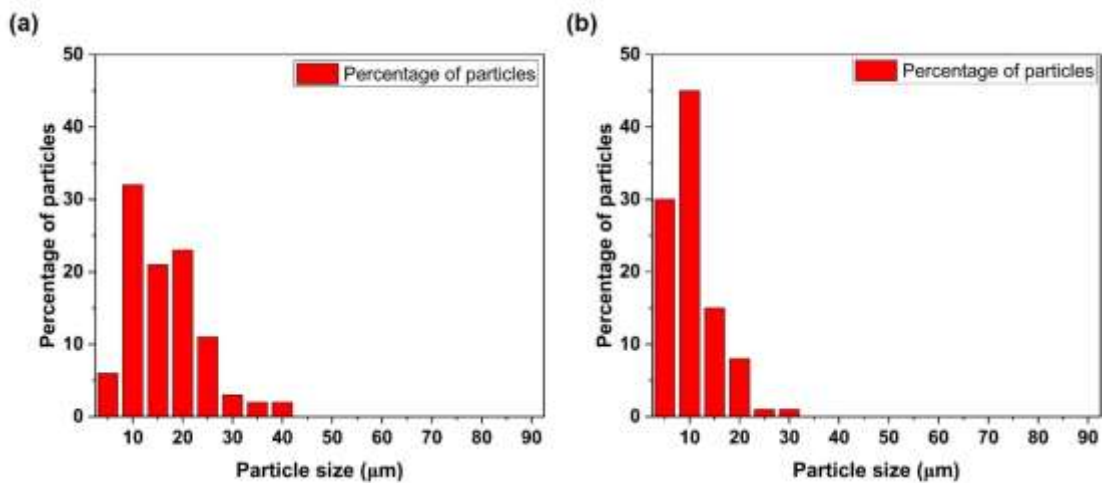


Figure 4.8 Particle size distribution of CoCrNiTiMo HEA powders milled for a) 10 h and b) 30 h at a milling speed of 300 rpm.

### 4.3 Processing of CoCrNiTiW HEAs by Mechanical Alloying

#### 4.3.1 Phase evolution of ball milled powders

Figure 4.9 illustrates the phase evolution of CoCrNiTiW HEA powders with respect to milling time. The XRD data of the blended powders before the start of the milling process showed the presence of all elemental metal powders, including Co, Cr, Ni, Ti, and W. After 10 h of milling, most of the diffraction peaks corresponding to the Ti element disappeared, confirming the diffusion of Ti into the lattice. The elements with lesser melting points possess high diffusion coefficients and are more likely to diffuse

into the lattice sites of the solvent (Chen et al. 2009). Apart from Ti, the peaks corresponding to Co were partially dissolved into the lattice, confirming the start of solid solution formation. After 20 hours, all the titanium and cobalt peaks are completely dissolved into the lattice. The peaks corresponding to Ni also started to dissolve into the lattice sites of Chromium and Tungsten at this stage.

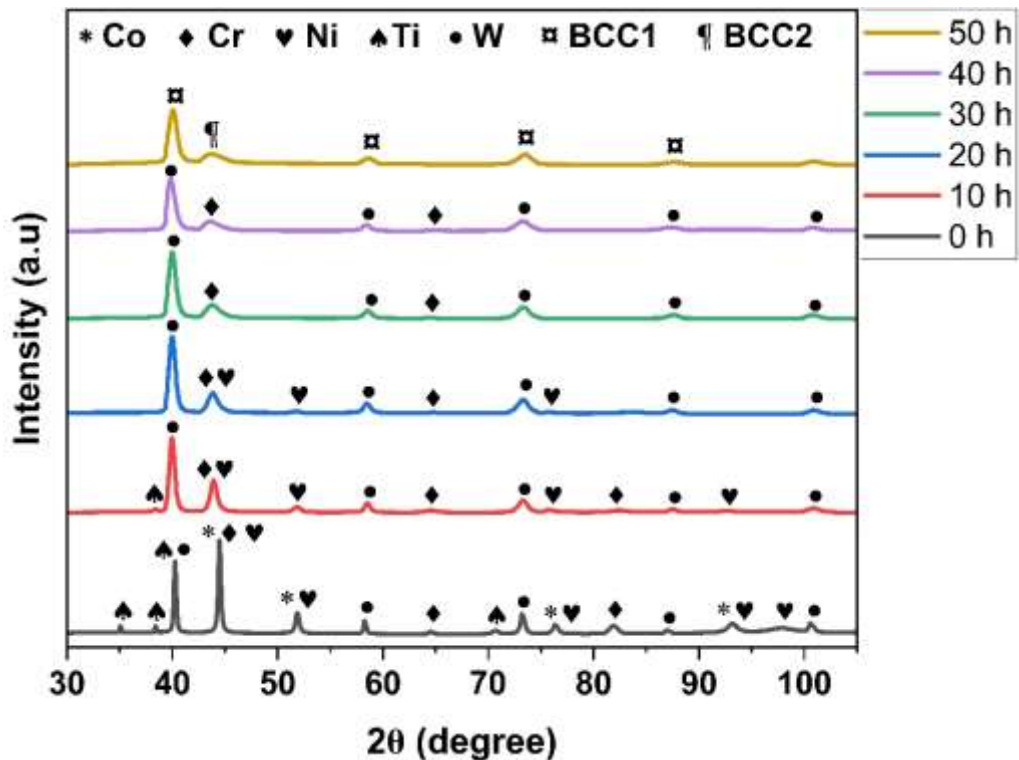


Figure 4.9 XRD of CoCrNiTiW HEA powders at different milling times.

On further continuing the milling up to 30 h, all the Ni peaks completely disappeared. Further, a noticeable drop in the intensity and widening of the major peaks corresponding to chromium and Tungsten can be witnessed in Figure 4.9. The reduction in the peak intensity is attributed to the diffusion of elements, enabling solid solution formation (Varalakshmi et al. 2008). Whereas the peak broadening is due to the decrease in crystallite size and increase in lattice strain as the milling progresses with time (Shivam et al. 2019; Suryanarayana et al. 2001). On increasing the milling time further up to 40 h, no noticeable change in the phase structure can be seen. However, a decrease in the peak intensities and a reasonable broadening of peaks can be observed. The analysis of the alloy after 50 h of milling revealed the formation of two BCC solid solutions with lattice parameters of 3.152 Å (BCC1) and 2.885 Å (BCC2), respectively.

### 4.3.2 Calculation of crystallite size and lattice strain

From Table 4.3, it is observed that the crystallite size of the CoCrNiTiW powders milled at 200 rpm, steadily decreased with respect to time. At the beginning of the milling, the blended powders possessed a crystallite size of 136 nm, thereafter the crystallite size gradually reduced to 31.5 nm at the end of 50 hours of milling. From table 4.3, it can also be seen that the lattice strain of the milled powders gradually increased from 0.179% to 0.508% at the end of 50 hours of milling. The noticeable rise in the lattice strain is due to the inherent nature of the mechanical alloying process. The ball milling process induces strain in the lattice of the milled powders because of the continuous interaction and intense plastic deformation of the powders with the milling media.

Table 4.3 Calculation of crystallite size and lattice strain for CoCrNiTiW HEA

Milling time	Crystallite size (nm)	Lattice strain (%)
0 h	136	0.179
10 h	81.1	0.208
20 h	75.4	0.249
30 h	58.2	0.289
40 h	43.8	0.372
50 h	31.5	0.508

### 4.3.3 Microstructural evolution

The morphology evolution of CoCrNiTiW HEA powders at different milling times can be witnessed in Figure 4.10. At the start of the milling, the powder particles exhibit uneven morphology with different shapes, owing to the various processing methods involved in preparing pure metal powders. The particle size of the blended powders, before the start of milling, ranged from 45-55  $\mu\text{m}$ . After 10 h of milling, flattening of the powder particles is predominant due to the entrapment and repeated impact of the powder particles between the vial and balls (Suryanarayana 2001). The average particle size at this stage can be found to be around 18-22 microns. At this stage, as the milling balls collide with each other and the powders, some of the powders were agglomerated and cold welded at their contact points due to the high pressure and temperatures generated during the milling process (Suryanarayana 2019). Since the milling process

is carried out in a wet atmosphere, the extent of cold welding at this stage is controlled by the process control agent. Nevertheless, occasional cold welding of the milled powders can be seen from Fig. 4.10c. Fracturing and refinement of the powder particles can be seen by continuing the milling for up to 30 h (Figure 4.10d). The morphology of the particles tends to be more spheroidal at longer milling hours due to the continuous refinement (Tian et al. 2018). The powders particle size was further refined to 4-5 microns after 50 h of milling.

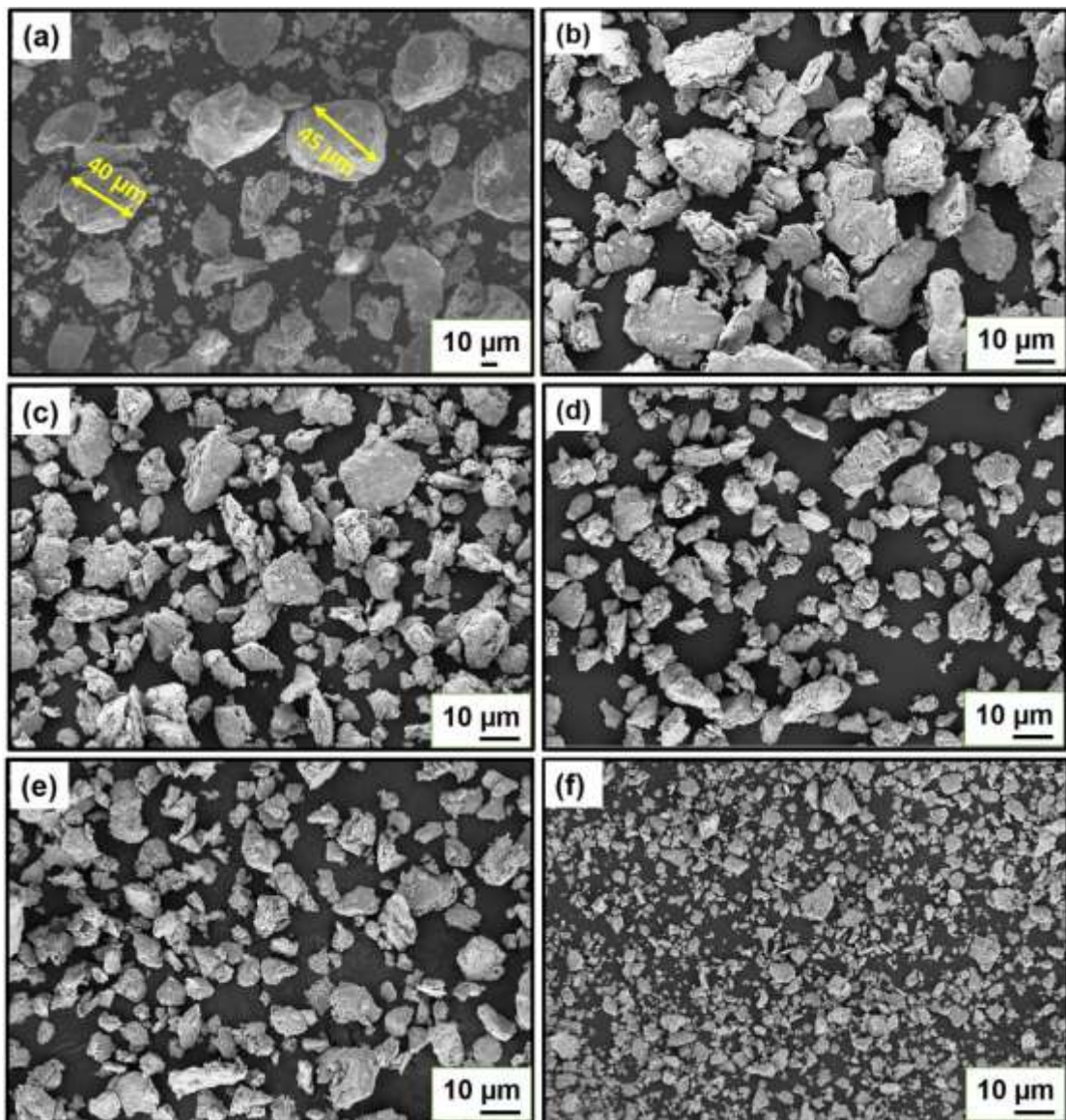


Figure 4.10 Microstructural evolution of CoCrNiTiW HEA powders after milling for a) 0 h b) 10 h c) 20 h d) 30 h, e) 40 h, and f) 50 h.

The chemical composition of the milled powders can be seen in the Figure 4.11. It is evident that the mechanical alloying process resulted in the homogeneous mixing as well as a significant reduction in the particle size of the alloying powders. Fig. 4.11 depicts a minimal deviation in the expected and observed compositions of the milled powders, conveying a homogeneous distribution of the constituent elements in the milled powders.

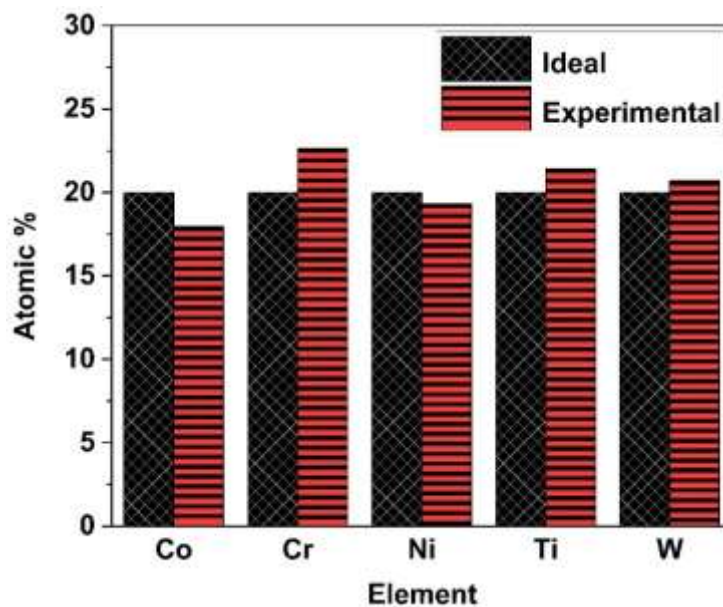


Figure 4.11 Chemical composition of CoCrNiTiW HEA powders milled at 200 rpm for 50 hours

#### 4.3.4 Particle size analysis

Figure 4.12 illustrates the progression of particle size for CoCrNiTiW HEA powders milled at 200 rpm. Initially, after 10 hours of milling, the average particle size measures 26 microns, exhibiting a wide range of particle sizes from 5 to 90 microns. Notably, 86% of the particles fall within the 5-50 micron range. As the milling process continues, there is a discernible reduction in the average particle size, accompanied by a narrowing of the size distribution range. Upon reaching 50 hours of milling, the average particle size further decreases to 7 microns, and the distribution range becomes even more constrained, ranging from 1 to 30 microns. This signifies a substantial refinement in particle size, underscoring the efficacy of prolonged milling at 200 rpm in producing finer and more homogeneously sized CoCrNiTiW HEA powders.

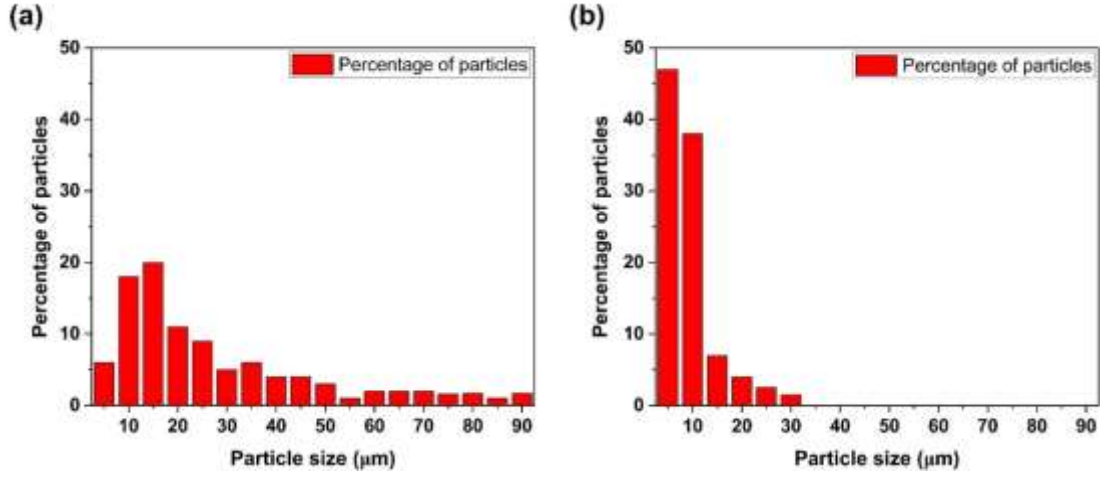


Figure 4.12 Particle size distribution of CoCrNiTiW HEA powders milled for (a) 10 h and (b) 50 h at a milling speed of 200 rpm.

#### 4.4 Solid Solution formation criteria in High entropy alloys

In case of binary alloys, the formation of solid solution has been identified by Hume-Ruthery rules. Likewise, concerning High Entropy Alloys, Zhang et al. (2008) outlined the criteria for the formation of solid solution phases. Thermodynamic factors such as atomic size difference, enthalpy and entropy of mixing, valence electron concentration, and electronegativity difference were employed to assess the potential for solid solution formation in High Entropy Alloys (Guo 2015; Guo i Liu 2011). The corresponding equations (Eq. 4.4-4.10) were given below and the calculated parameters are presented in Table 4.4.

$$\delta = 100 \sqrt{\sum_{i=1}^n c_i \left(1 - \frac{r_i}{\bar{r}}\right)^2} \quad (4.4)$$

$$\bar{r} = \sum_{i=1}^n C_i r_i \quad (4.5)$$

$C_i$  and  $r_i$  is the atomic fraction and atomic radius of the  $i^{\text{th}}$  element.  $\bar{r}$  is the average atomic radius.  $\delta$  is the atomic size difference.

$$\Delta H_{mix} = 4 \sum_{i=1, i \neq j}^n \Delta H_{mix}^{ij} c_i c_j \quad (4.6)$$

$\Delta H_{mix}^{ij}$  is the enthalpy of mixing of the binary alloy.  $c_i$  and  $c_j$  are the atomic fractions of the elements in the binary alloy.  $\Delta H_{mix}$  is the enthalpy of mixing of the alloy.

$$\Delta S_{mix} = -R \sum_{i=1}^n c_i \ln c_i \quad (4.7)$$

Where  $\Delta S_{mix}$  is the entropy of mixing and R is gas constant.

$$VEC = \sum_{i=1}^n c_i (VEC)_i \quad (4.8)$$

Where  $(VEC)_i$  is the valence electron concentration of the  $i^{\text{th}}$  element and VEC is for the alloy.

$$\Delta X = \sqrt{\sum_{i=1}^n c_i (X_i - \bar{X})^2} \quad (4.9)$$

$$\bar{X} = \sum_{i=1}^n c_i X_i \quad (4.10)$$

Where  $X_i$  is the pauling electronegativity for the  $i^{\text{th}}$  element and  $\bar{X}$  is the averaged electronegativity.  $\Delta X$  is the electronegativity difference of the alloy.

Drawing from empirical relations, (Guo 2015) established specific guidelines for the creation of stable solid solutions in High Entropy Alloys. They identified that the formation of a stable solid solution is feasible under the conditions of  $-22 < \Delta H_{mix} < 7$  kJ/mol,  $11 < \Delta S_{mix} < 19.5$  J/K·mol, and  $0 < \delta < 8.5$ . Guo (2015) also outlined criteria for the type of solid solution phase formation based on Valence Electron Concentration (VEC) values. According to their findings, BCC phases would exclusively form when VEC is less than 6.87, a combination of BCC and FCC phases in the range of  $6.87 < VEC < 8$ , and solely FCC phases when VEC exceeds 8. Further, the phases are more stable if the electronegativity difference  $\Delta X > 0.133$  (Dong et al. 2014).. Enthalpy of mixing of the High entropy alloy has been calculated from the enthalpy of mixing values of the binary alloy using Miedema's model (Takeuchi and Inoue 2005). Yang and Zhang have determined a parameter  $\Omega$  for defining the stability of solid solutions and the equation is presented in Eq. 4.11 and Eq. 4.12 (Yang i Zhang 2012).

$$\Omega = \frac{T_m \Delta S_{mix}}{|\Delta H_{mix}|} \quad (4.11)$$

$$T_m = \sum_{i=1}^n c_i (T_m)_i \quad (4.12)$$

Where  $(T_m)_i$  is the melting point of the  $i^{\text{th}}$  element and  $T_m$  is the melting point of the alloy. It has been proposed that if  $\Omega > 1$ , then the contribution of  $T_m \Delta S_{mix}$  will exceed

that of  $\Delta H_{mix}$  and thus the formation of solid solution phases is stable according to Gibbs free energy rule (Eq. 4.13) (Yang i Zhang 2012)

$$\Delta G_{mix} = \Delta H_{mix} - T\Delta S_{mix} \quad (4.13)$$

Based on the empirical relations, the thermodynamic parameters are calculated and listed in the Table 4.4. The results show that the entropy of mixing, atomic size difference, enthalpy of mixing, electronegativity difference and sigma values for both the compositions satisfy the criteria set by Guo et al. for the formation of solid solution phases. The calculated VEC values predict a mixture of FCC and BCC phases for both CoCrNiTiMo and CoCrNiTiW high entropy alloys, whereas the data confirms the formation of 2 BCC solid solution phases. Further it is not mandatory that the predicted phases should always form. Dwivedi et al. (2016) reported the formation of a FCC phase, while the VEC values predict the formation of BCC phase.

Table 4.4 Thermodynamic parameters of processed High entropy alloy:

Composition	$\Delta S_{mix}$ (J/mol. K)	$\delta$	$\Delta H_{mix}$ (kJ/mol)	VEC	$\Delta X$	$T_m$ (K)	$\Omega$
CoCrNiTiMo <sub>0.5</sub>	13.14	3.81	-17.23	7.10	0.194	1994	1.520
CoCrNiTiMo	13.38	2.68	-15.52	7	0.214	2102	1.812
CoCrNiTiMo <sub>1.5</sub>	13.25	3.07	-13.87	6.88	0.225	2152	2.076
CoCrNiTiW <sub>0.5</sub>	13.14	2.08	-16.54	7.10	0.240	2082	1.654
CoCrNiTiW	13.38	1.78	-17.42	7	0.280	2262	1.737
CoCrNiTiW <sub>1.5</sub>	13.25	1.86	-12.24	6.88	0.302	2368	2.563

#### 4.5 Summary

Mechanical alloying, a non-equilibrium processing technique, is used for synthesizing the CoCrNiTiMo<sub>x</sub> and CoCrNiTiW<sub>x</sub> HEA feedstock. The constituent metal powders were mixed in appropriate proportions according to their weight fractions and grounded in a planetary ball mill with a tungsten carbide vial and balls. In order to identify the ideal milling time for synthesizing CoCrNiTiMo<sub>x</sub> and CoCrNiTiW<sub>x</sub> high entropy alloy feedstock powders, milling was carried out for 50 h and samples were taken at regular intervals of 10 hours for characterization. After thoroughly characterizing the milled powders with respect to phases, microstructure, chemical homogeneity and particle size evolution, at different milling speeds and times, the HEA powders milled for 10 h at a

milling speed of 200 rpm was selected as feedstock for thermal spray deposition using HVOF technique. The average particle sizes of the CoCrNiTiMo and CoCrNiTiW feedstock powders, as determined from the laser diffraction analysis using a particle size analyser, were found to be 23.18  $\mu\text{m}$  and 25.66  $\mu\text{m}$  respectively. Similarly, the particle sizes of other HEA compositions used in the current research varied from 22  $\mu\text{m}$  – 27  $\mu\text{m}$ . The corresponding thermodynamic parameters of the processed HEA's, including atomic size difference, enthalpy of mixing, entropy of mixing, valence electron concentration, and electro negativity were calculated in order to predict the solid solution phase formation.

## CHAPTER 5

### CHARACTERIZATION OF HEA COATINGS

#### 5.1 Characterization of CoCrNiTiMo<sub>x</sub> HEA coatings

##### 5.1.1 Surface morphology

Figure 5.1 shows the surface morphologies of CoCrNiTiMo<sub>0.5</sub>, CoCrNiTiMo, and CoCrNiTiMo<sub>1.5</sub> HEA coatings deposited by HVOF spray. It is evident that the all the coated surfaces typically consists of multiple unmolten, partially molten, and fully molten particles spread across the surface.

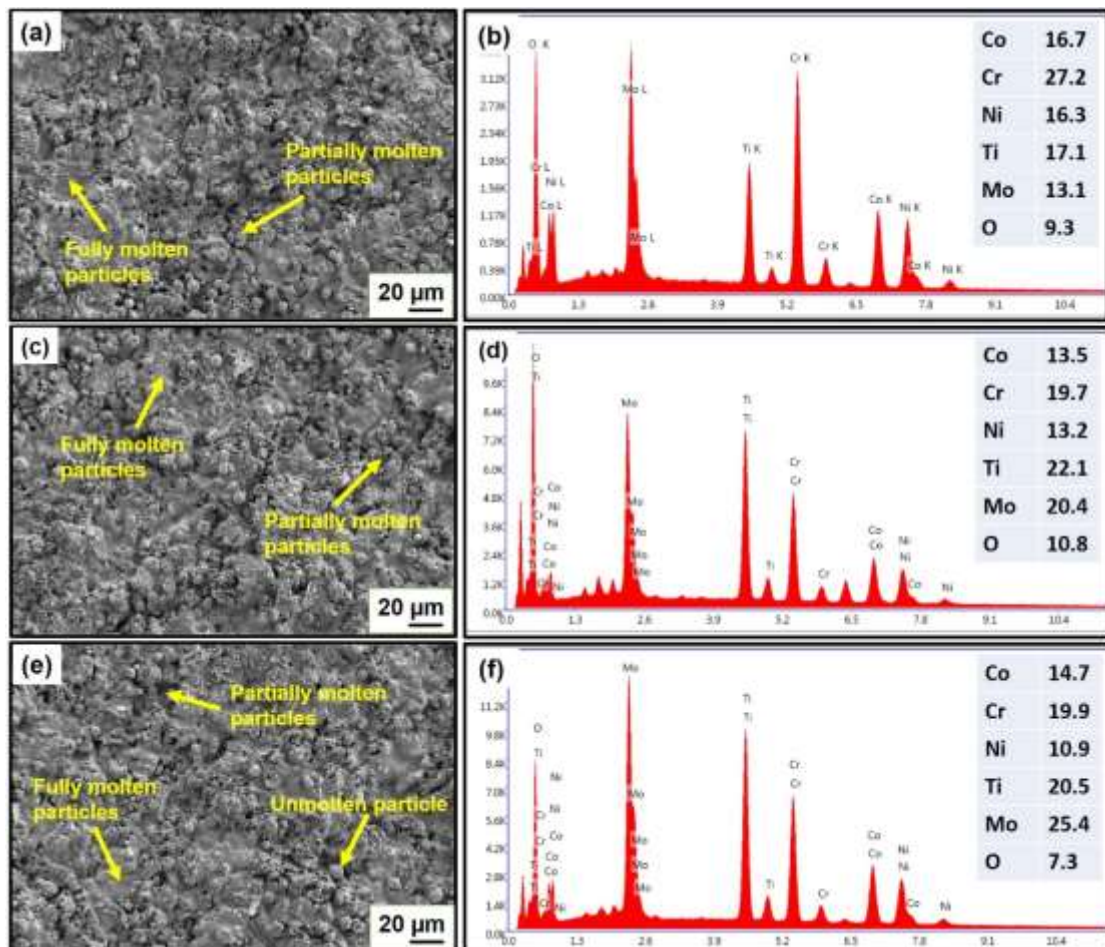


Figure 5.1 Surface morphology of (a) CoCrNiTiMo<sub>0.5</sub>, (c) CoCrNiTiMo and (e) CoCrNiTiMo<sub>1.5</sub> HEA coatings deposited by HVOF spray. (b), (d), (f) shows the EDS analysis of corresponding HEA coated surfaces respectively.

Many undulations and a rough surface can be seen, which is typical of HVOF spray. Since HVOF spray works on imparting high kinetic energies to the feedstock materials, complete melting of the feedstock is not possible. Furthermore, the insufficient melting time in the spray nozzle eventually forms partially molten surfaces (Prasad et al. 2019). The EDS analysis performed on the surface confirms the presence of all alloying elements along with significant contributions from oxygen.

### 5.1.2 Cross-sectional microstructure

The coating thickness of  $\text{CoCrNiTiMo}_x$  ( $x$  is atomic fraction;  $x= 0.5, 1, 1.5$  HEA coatings varies between 216-234 microns, as seen from the cross-sectional SEM images (Figure 5.2). The coating cross-section in Figure. 5.2 possess lamellar structure, owing to the layer by layer stacking of the deposited feedstock splats (Liu et al. 2022b). During HVOF spray deposition, the semi-molten feedstock particles impact the substrate surface with high velocities and solidify rapidly, forming dense coatings. The high-energy impact of the feedstock particles creates a mechanical deformation in the substrate surface and promotes bonding between the coating and substrate.

The mechanical interlocking of the coating splats to the substrate can be seen at the coating interface in Figure 5.3. A rough wavy surface, with crests and troughs, can be seen at the interface of HEA coatings (Nair et al. 2023). Pores and cracks were minimal near the interface, suggesting better adhesion of the coated layers to the substrate (Chen et al. 2015a). The porosities of  $\text{CoCrNiTiMo}_{0.5}$ ,  $\text{CoCrNiTiMo}$ , and  $\text{CoCrNiTiMo}_{1.5}$  HEA coatings, as determined by image analysis, were observed to be  $1.1 \pm 0.3\%$ ,  $1.12 \pm 0.05 \%$ , and  $1.32 \pm 0.2\%$  respectively. Oxide inclusions can be occasionally seen throughout the coating cross-section in minor proportions, owing to the oxidation of the in-flight particles during deposition (Patel et al. 2022). The dark regions (highlighted as points 1,3&5) in Figure 5.2 represent the oxy-rich phases. In contrast, the grey regions (highlighted as points 2,4&6) represent a homogeneous distribution of all constituent elements with minor oxide inclusions. Table 5.1 shows the compositions of highlighted points in Figure 5.2.

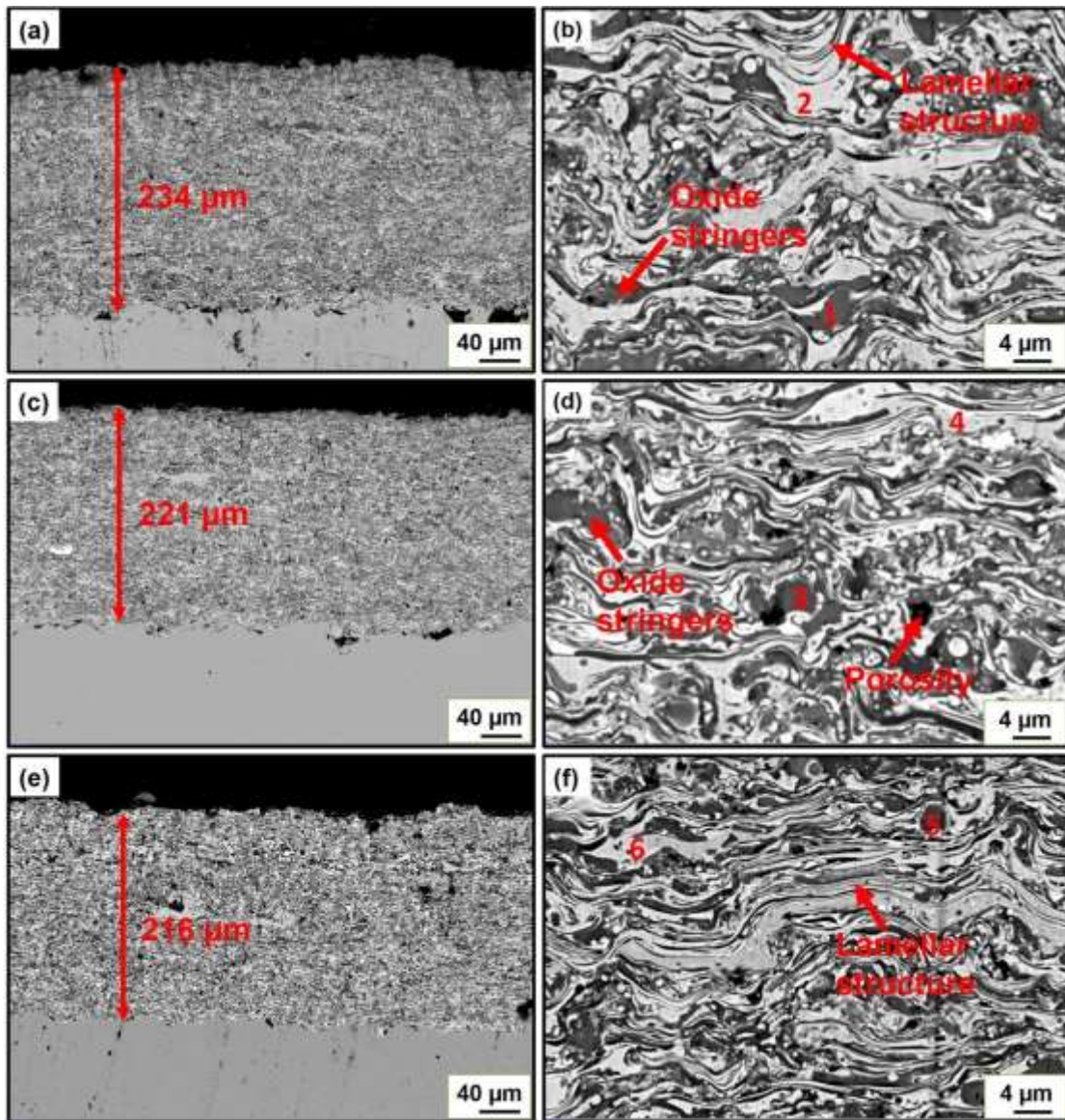


Figure 5.2. Cross-sectional microstructure of (a), (b) CoCrNiTiMo<sub>0.5</sub> (c), (d) CoCrNiTiMo, (e), (f) CoCrNiTiMo<sub>1.5</sub> HEA coatings in backscattered electron mode, showing coating thickness and lamellar structure.

Table 5.1 Chemical composition of highlighted points in Figure 5.2 (at %).

Point	Co	Cr	Ni	Ti	Mo	O
1	6.9	9.5	4.6	13.7	1.1	64.2
2	28.9	21.0	27.1	2.3	12.8	7.9
3	4.2	10.0	2.2	16.3	3.5	63.8
4	21.9	23.2	21.4	6.4	19.3	7.7
5	7.8	9.0	6.7	9.0	1.9	65.6
6	21.9	7.2	22.2	1.3	33.6	13.8

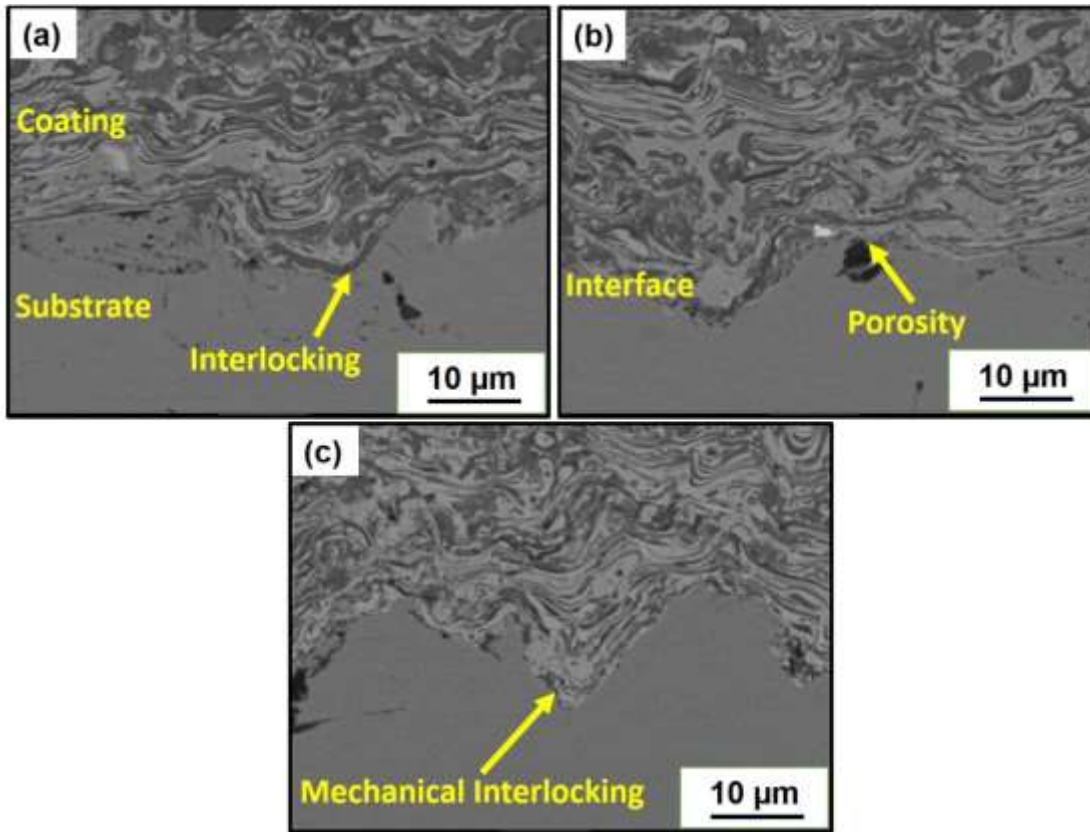


Figure 5.3. Interfacial bonding of (a) CoCrNiTiMo<sub>0.5</sub>, (b) CoCrNiTiMo, and (c) CoCrNiTiMo<sub>1.5</sub> HEA coatings with the Substrate.

The distribution of the constituent alloying elements in the microstructure is visualized by analyzing the elemental maps at the cross sections of the deposited HEA coatings. It can be identified from Figure 5.4 that all the HEA coatings exhibit a homogeneous distribution of the alloying elements. The CoCrNiTiMo<sub>1.5</sub> HEA coating also revealed a dense elemental map of Mo, indicating higher concentration of Molybdenum in the microstructure.

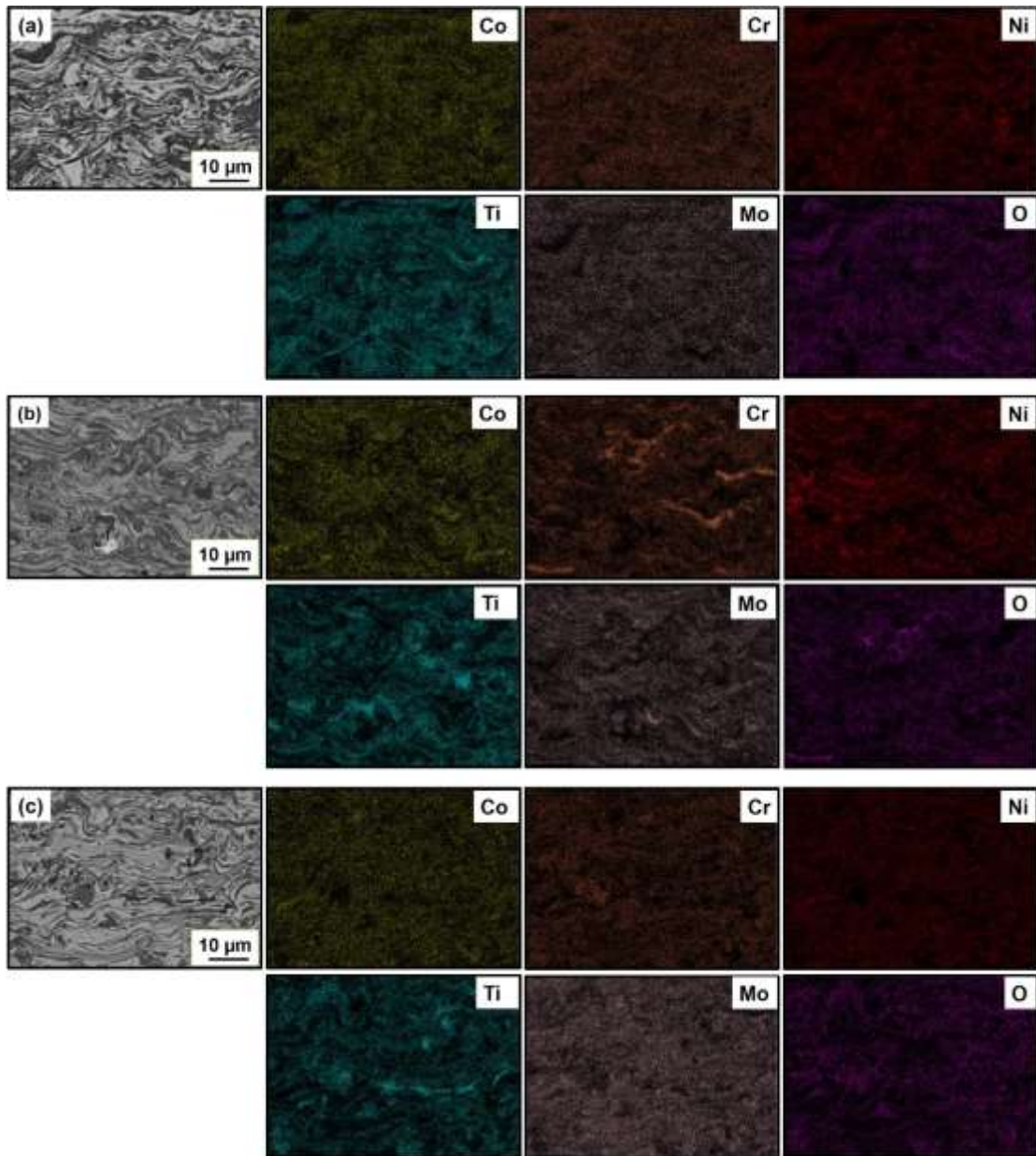


Figure 5.4 Elemental mapping of (a) CoCrNiTiMo<sub>0.5</sub>, (b) CoCrNiTiMo, and (c) CoCrNiTiMo<sub>1.5</sub> HEA coating cross-section.

### 5.1.3 XRD studies

Figure 5.5 presents the phases formed in the CoCrNiTiMo<sub>0.5</sub>, CoCrNiTiMo and CoCrNiTiMo<sub>1.5</sub> HEAs after the deposition of coatings. It is discernible from the XRD analysis that the BCC phases, forged during the milling stage, have persevered post-coating deposition. Nevertheless, the exposure to elevated temperatures and kinetic energies within the HVOF nozzle has instigated the emergence of supplementary

intermetallic and oxide phases. The feedstock powders underwent exposure to temperatures ranging from 1400 °C - 1600 °C and were propelled at velocities up to 1300 m/s during the coating deposition (Jin et al. 2020; Meghwal et al. 2022).

Retaining the solid solution phases during the HVOF coating process requires careful control of various parameters to prevent phase transformations, oxidation, and other detrimental effects that could alter the phases. The flame temperature has to be carefully controlled, so as to generate enough heat just to melt the powders. The flow rate of fuel and oxygen has to be appropriate, so as to preserve the desired temperatures. Moreover, optimal spray distance (typically 150-300 mm) has to be maintained, to ensure the particles reach the substrate at the correct temperature and state (semi-molten or fully molten). Too close may cause excessive heating, while too far may cause cooling and improper adhesion. Further, utilizing inert gas shielding (e.g., argon) during spraying also minimizes oxidation.

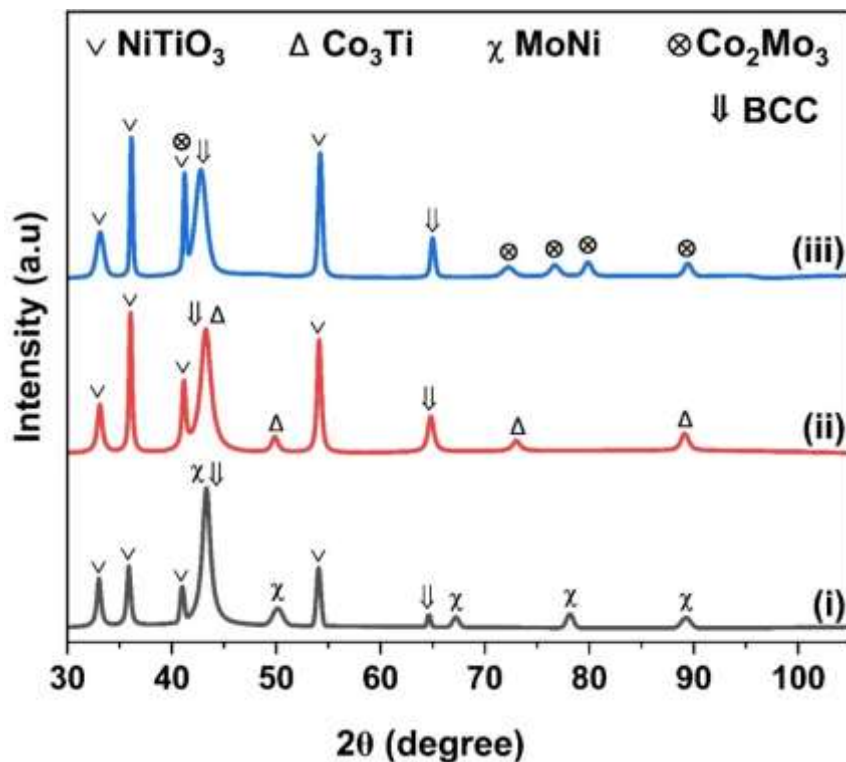


Figure 5.5 X-ray diffraction studies of HVOF sprayed (i) CoCrNiTiMo<sub>0.5</sub>, (ii) CoCrNiTiMo, and (iii) CoCrNiTiMo<sub>1.5</sub> HEA coating.

The as-sprayed CoCrNiTiMo<sub>0.5</sub> coatings displayed a BCC phase (PDF# 01-085-1336), NiTiO<sub>3</sub> spinel (PDF# 01-076-0334), and MoNi intermetallic (PDF# 00-048-1745). Likewise, the CoCrNiTiMo HEA coatings showed the presence of a single BCC phase (PDF# 01-085-1336), Co<sub>3</sub>Ti intermetallic (PDF# 03-065-4116) and NiTiO<sub>3</sub> (PDF# 01-076-0334). Further, the CoCrNiTiMo<sub>1.5</sub> HEA resulted in the formation of a Co<sub>2</sub>Mo<sub>3</sub> intermetallic, NiTiO<sub>3</sub> spinel, and BCC phase. The occurrence of oxide phases is attributed to the in-flight oxidation of feedstock powders. The presence of intermetallic phases contributes to the augmentation of hardness and mechanical properties (Chen et al. 2019c; Joseph et al. 2020; Liu et al. 2016). Moreover, there is a significant peak broadening in the XRD pattern of the coated samples, signifying a notable decrease in the crystallite size. The drop in the crystallite size may be ascribed to the relatively higher cooling rates in the thermal spray techniques (Chen et al. 2019a).

#### **5.1.4 Microhardness**

The microhardness values of CoCrNiTiMo<sub>0.5</sub>, CoCrNiTiMo, and CoCrNiTiMo<sub>1.5</sub> HEA coating cross-sections at different penetration depths have been presented in Figure 5.6. The microhardness near the substrate was around  $422 \pm 7$  HV<sub>0.3</sub>, with minimal variation. However, the deposited HEA coatings demonstrate a noticeable deviation in the microhardness at various distances from the interface. A sudden increase in the microhardness at the coating interface can be attributed to the work hardening effect. A reasonable variation in the microhardness values can be seen at different points, owing to the formation of different phases, including NiTiO<sub>3</sub> spinel, MoNi and Co<sub>3</sub>Ti intermetallic, and disordered BCC phases. Further, pores, oxides, melted and unmelted particles throughout the microstructure contribute to the disparity in the microhardness values (Jin et al. 2018b; Tian 2016).

Typical Vickers hardness values for HEA coatings often range between 500 to 1200 HV. Some specific HEA coatings, particularly designed for wear resistance and high-temperature applications, can achieve even higher hardness values. In the current work, the average microhardness values of the as-sprayed CoCrNiTiMo<sub>0.5</sub>, CoCrNiTiMo, and CoCrNiTiMo<sub>1.5</sub> HEA coatings were  $841 \pm 62$  HV<sub>0.3</sub>,  $927 \pm 45$  HV<sub>0.3</sub>, and  $952 \pm 23$  HV<sub>0.3</sub>, respectively. The high hardness of the investigated HEAs can be attributed to the BCC solid solutions and intermetallic compounds formed during thermal spray deposition.

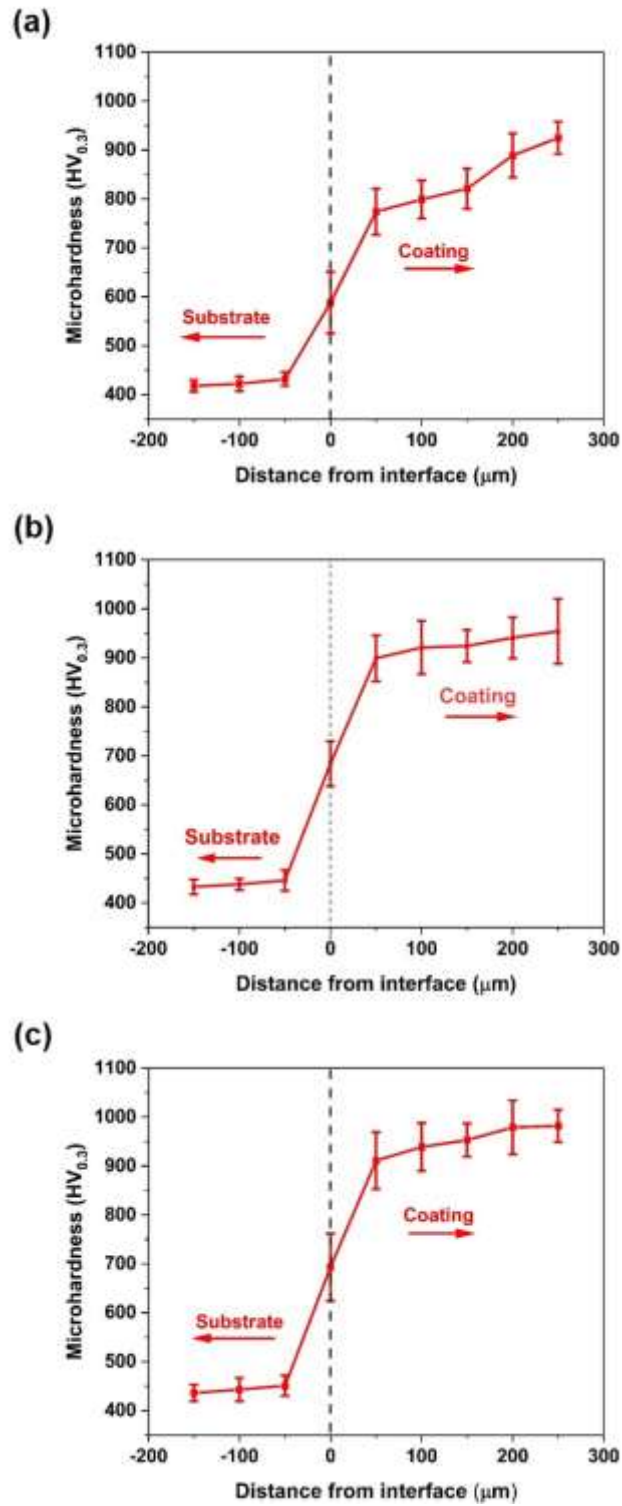


Figure 5.6 Vickers microhardness of (a) CoCrNiTiMo<sub>0.5</sub>, (b) CoCrNiTiMo, and (c) CoCrNiTiMo<sub>1.5</sub> HEA coatings.

HEAs containing disordered BCC phases demonstrate high hardness compared to FCC-based HEAs (Nair et al. 2023). Furthermore, HEAs display high strength and hardness due to the lattice distortion effect of the different constituent elements (Lee et al. 2020; Roy et al. 2021). Additionally, a significant increment is seen in the microhardness values of the CoCrNiTiMo<sub>1.5</sub> HEA coatings, compared to that of as-sprayed CoCrNiTiMo<sub>0.5</sub> coatings, owing to the presence of higher molar fractions of Molybdenum.

### **5.1.5 Fracture toughness**

Fracture toughness measures a material's ability to withstand the growth of existing cracks or the initiation of new ones. In the context of sliding wear, where surfaces are subjected to repeated friction and contact stresses, a coating with high fracture toughness is generally more resistant to cracking and failure. In Figure 5.7, the emergence of cracks is depicted, originating from the tips of the Vickers indenter and running parallel to the coating-substrate interface. The material's fracture toughness is determined by calculating the length of radial cracks emerging from the tips of the indenter. There were no observed cracks perpendicular to the free surface of the coating, suggesting an anisotropic behaviour influenced by the layered microstructure and elongated shape of the splats in the thermally sprayed coatings (Lekatou et al. 2023).

Within a thermally sprayed coating, the interlamellar regions and splat boundaries may act as areas with heightened stress concentration and diminished cohesive strength. Hence, the occurrence of pores and the propagation of microcracks are frequently observed at the boundaries of the splats (Zois et al. 2009). The average fracture toughness of refractory HEA coatings typically falls within the range of 3 to 6 Mpa m<sup>1/2</sup> (Lin et al. 2015; Ndumia et al. 2023), with specific values depending on the composition, deposition method, and microstructural characteristics. The average fracture toughness of refractory HEA coatings is generally lower than that of bulk HEAs due to the coating's microstructure, thickness, and the presence of interfaces with the substrate. Enhancing the fracture toughness while maintaining other desirable properties remains a key challenge in the development and optimization of refractory HEA coatings.

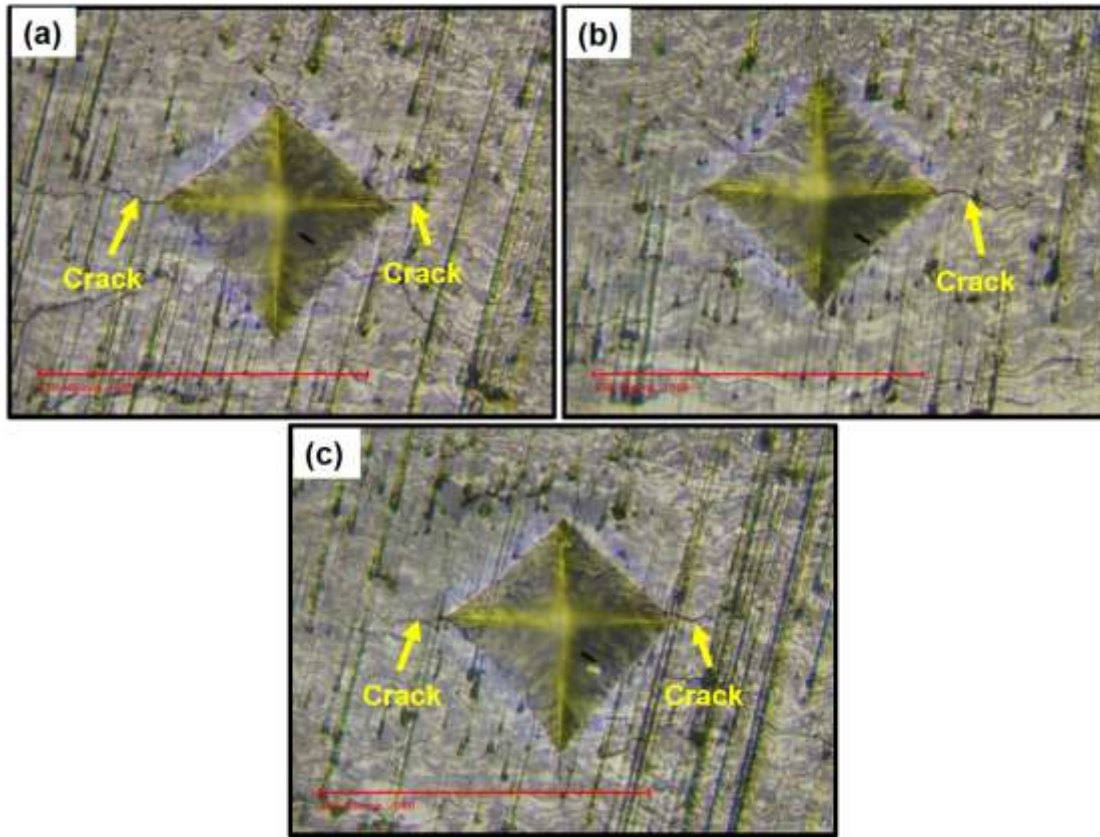


Figure 5.7 Optical microscope image showing the crack propagation for (a) CoCrNiTiMo<sub>0.5</sub>, (b) CoCrNiTiMo, and (c) CoCrNiTiMo<sub>1.5</sub> HEA coatings under a Vickers indenter.

The fracture toughness of CoCrNiTiMo<sub>0.5</sub>, CoCrNiTiMo, and CoCrNiTiMo<sub>1.5</sub> HEA coatings, as determined by using Evans and Wilshaw's equation, were found to be  $2.89 \pm 0.31$  (Mpa m<sup>1/2</sup>),  $3.26 \pm 0.25$  (Mpa m<sup>1/2</sup>) and  $3.79 \pm 0.35$  (Mpa m<sup>1/2</sup>) respectively. CoCrNiTiMo<sub>1.5</sub> HEA coating showed better fracture toughness than CoCrNiTiMo<sub>0.5</sub> and other thermally sprayed coatings (Lin et al. 2015; Ndumia et al. 2023). The coatings with higher fracture toughness values can absorb more energy before fracture, thus enhancing wear performance.

### 5.1.6 Surface Roughness and density

The 3-dimensional roughness plots of CoCrNiTiMo<sub>0.5</sub>, CoCrNiTiMo and CoCrNiTiMo<sub>1.5</sub> HEA coatings can be seen in Figure. 5.8. It is evident that there were many surface asperities and undulations on the coated surface, owing to the deposition and solidification of molten splats. The average surface roughness of CoCrNiTiMo<sub>0.5</sub>,

CoCrNiTiMo and CoCrNiTiMo<sub>1.5</sub> HEA coatings were found to be 4.915  $\mu\text{m}$ , 3.178  $\mu\text{m}$  and 4.266  $\mu\text{m}$ , respectively. Coatings deposited by HVOF technique, often result in smoother microstructures with comparatively lesser roughness values, enabling their application in various wear resistant components. The surface roughness of the deposited coatings can be further tailored by controlling the process parameters during the coating deposition. Furthermore, the average densities of CoCrNiTiMo<sub>0.5</sub>, CoCrNiTiMo and CoCrNiTiMo<sub>1.5</sub> HEA coatings, as determined using ASTM C 135 standards, were found to be 6.42 g/cm<sup>3</sup>, 6.96 g/cm<sup>3</sup> and 7.47 g/cm<sup>3</sup>, respectively.

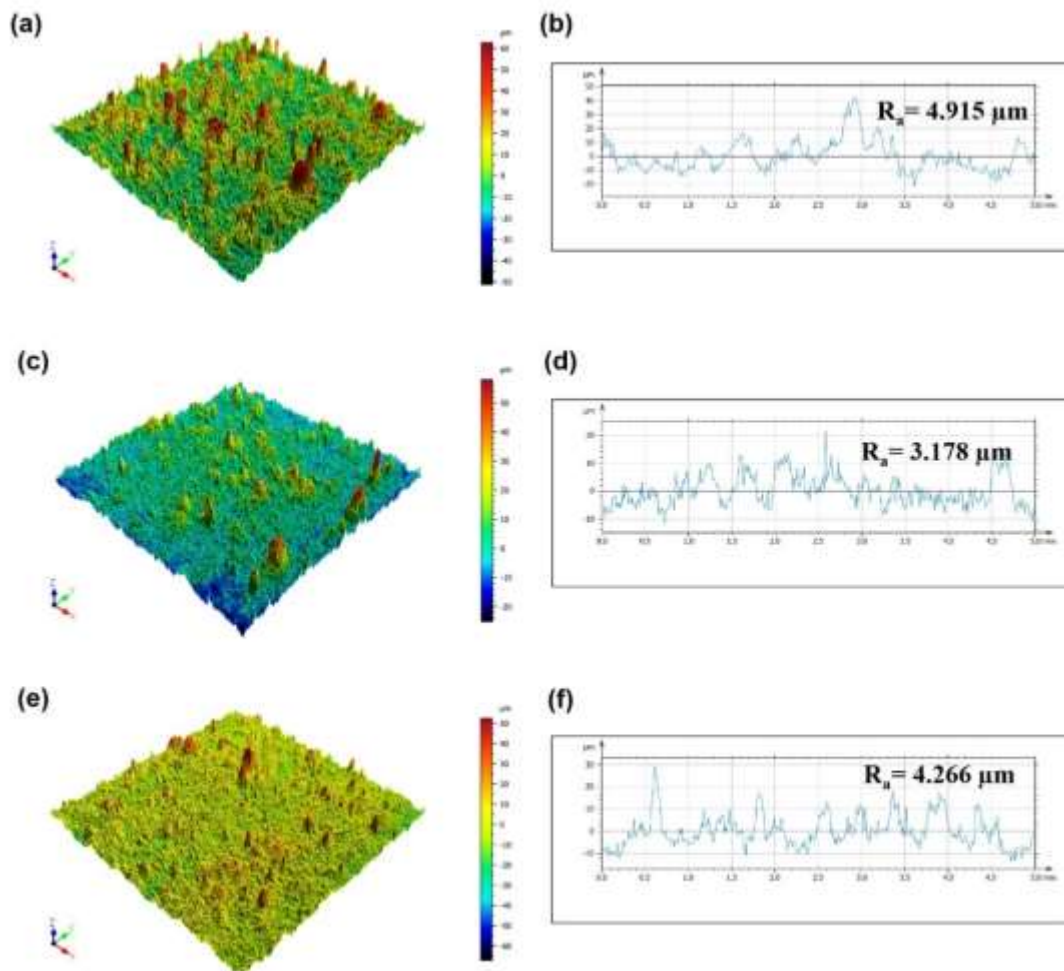


Figure 5.8 Profilometry studies showing the 3-dimensional roughness plot of (a) CoCrNiTiMo<sub>0.5</sub>, (c) CoCrNiTiMo, and (e) CoCrNiTiMo<sub>1.5</sub> HEA Coatings. Corresponding 2D line profiles can be seen in (b), (d), (f) respectively.

## 5.2 Characterization of CoCrNiTiW<sub>x</sub> HEA coatings

### 5.2.1 Surface morphology

Figure 5.9 shows the surface morphologies of CoCrNiTiW<sub>0.5</sub>, CoCrNiTiW, and CoCrNiTiW<sub>1.5</sub> HEA coatings deposited by HVOF spray. Many partially molten and unmolten particles can be identified on the coating surface, which is inherent in thermal spray deposition techniques. The high velocities in the HVOF nozzle lead to a lesser interaction time of the feedstock particles with the combustion gases, forming numerous partially molten splats (Prasad et al. 2019).

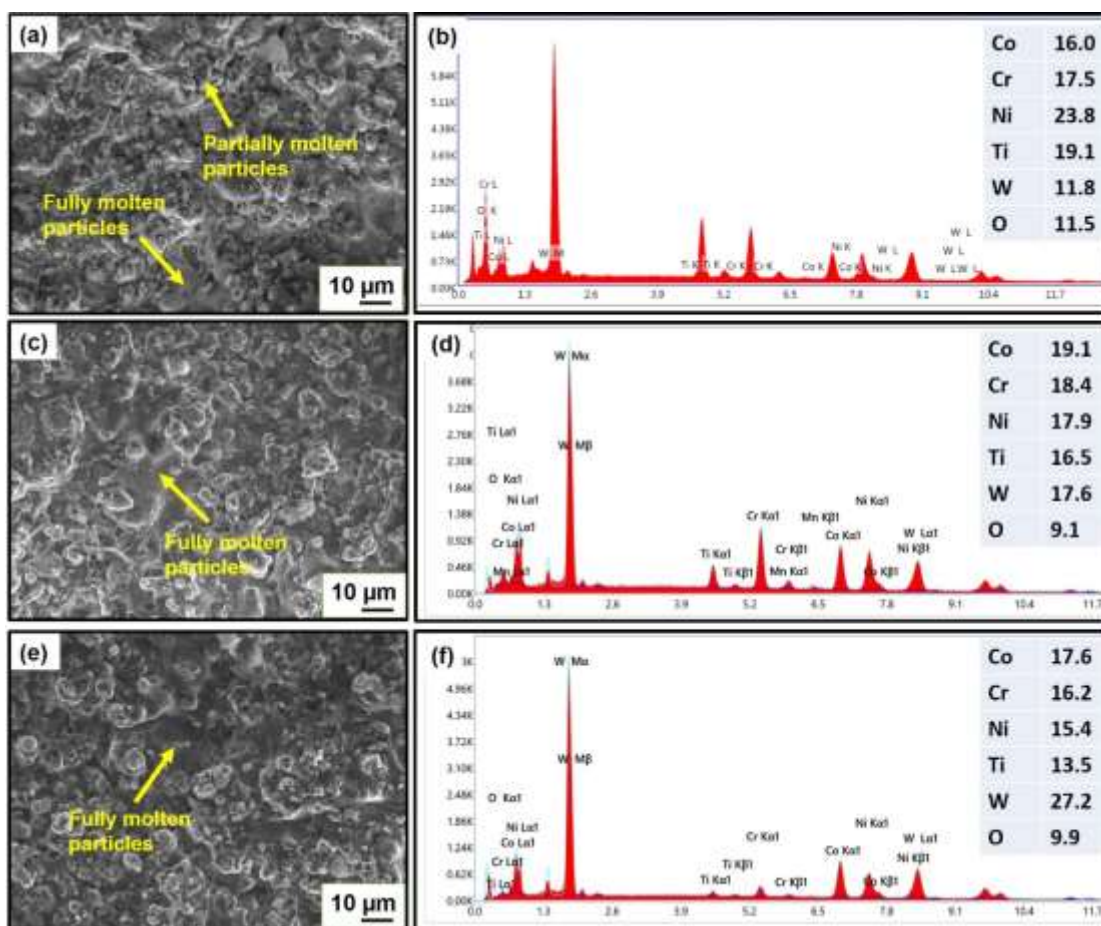


Figure 5.9 Surface morphology of (a) CoCrNiTiW<sub>0.5</sub>, (c) CoCrNiTiW and (e) CoCrNiTiW<sub>1.5</sub> HEA coatings deposited by HVOF spray. (b), (d), (f) shows the EDS analysis of corresponding HEA coated surfaces respectively.

The high velocities and lower temperatures observed in the HVOF nozzle also help attain microstructures with fewer defects. Typically, the particle velocity in an HVOF process ranges from 500 to 1,300 m/s. The particle spray velocity is widely affected by

the choice of fuel, flow rate of gases in the HVOF nozzle, spray distance and the coating density. The choice of fuel (e.g., hydrogen, propane, kerosene) affects the combustion temperature and the resultant gas velocity. The spray distance and the coating density also influence the spraying velocity. Therefore, the process parameters adopted in the current research were fixed after analysing the parameters considered for similar HEA coatings. The EDS analysis performed on the surface highlights the presence of all alloying elements along with significant contributions from oxygen (Figure 5.9 b,d&f).

### **5.2.2 Cross-sectional microstructure**

Figure 5.10 shows the cross-sectional microstructures of CoCrNiTiW<sub>0.5</sub>, CoCrNiTiW and CoCrNiTiW<sub>1.5</sub> HEA coatings in backscattered electron imaging mode. The coating thickness is observed to be uniform and is around  $252 \pm 8 \mu\text{m}$  for CoCrNiTiW<sub>0.5</sub>,  $236 \pm 7 \mu\text{m}$  for CoCrNiTiW and  $278 \pm 12 \mu\text{m}$  for CoCrNiTiW<sub>1.5</sub> HEA (Fig. 5.10a,c&e). Maintaining a constant thickness along the coatings cross-section ensures uniform mechanical properties such as hardness, wear resistance, and fatigue strength across the coated surface. A uniform coating thickness helps in evenly distributing stresses across the coated surface, reducing the risk of stress concentrations that can lead to cracks or delamination. Furthermore, Consistent thickness ensures a uniform bond strength between the coating and the substrate, enhancing the overall adhesion and reducing the likelihood of coating failure.

A lamellar microstructure can be seen, which is a typical characteristic of HVOF spray (Srivastava et al. 2019). Multiple lamellar structures were seen to be stacked one over the other due to the impact and solidification of the molten splats on the previously deposited splat. Feedstock powders were exposed to temperatures of 1500 °C and accelerated to velocities ranging from 500 - 1300 m/s during deposition. Therefore, inflight oxidation of molten splats is apparent, forming oxide stringers (Jin et al. 2020; Meghwal et al. 2022). Furthermore, the fine powder particles possessing higher surface area were extremely reactive and resulted in the formation of oxide stringers. The entrapment of oxide stringers between the coating splats was comparatively lesser for CoCrNiTiW<sub>1.5</sub>, owing to the relatively higher particle size of the CoCrNiTiW<sub>1.5</sub> feedstock powder.

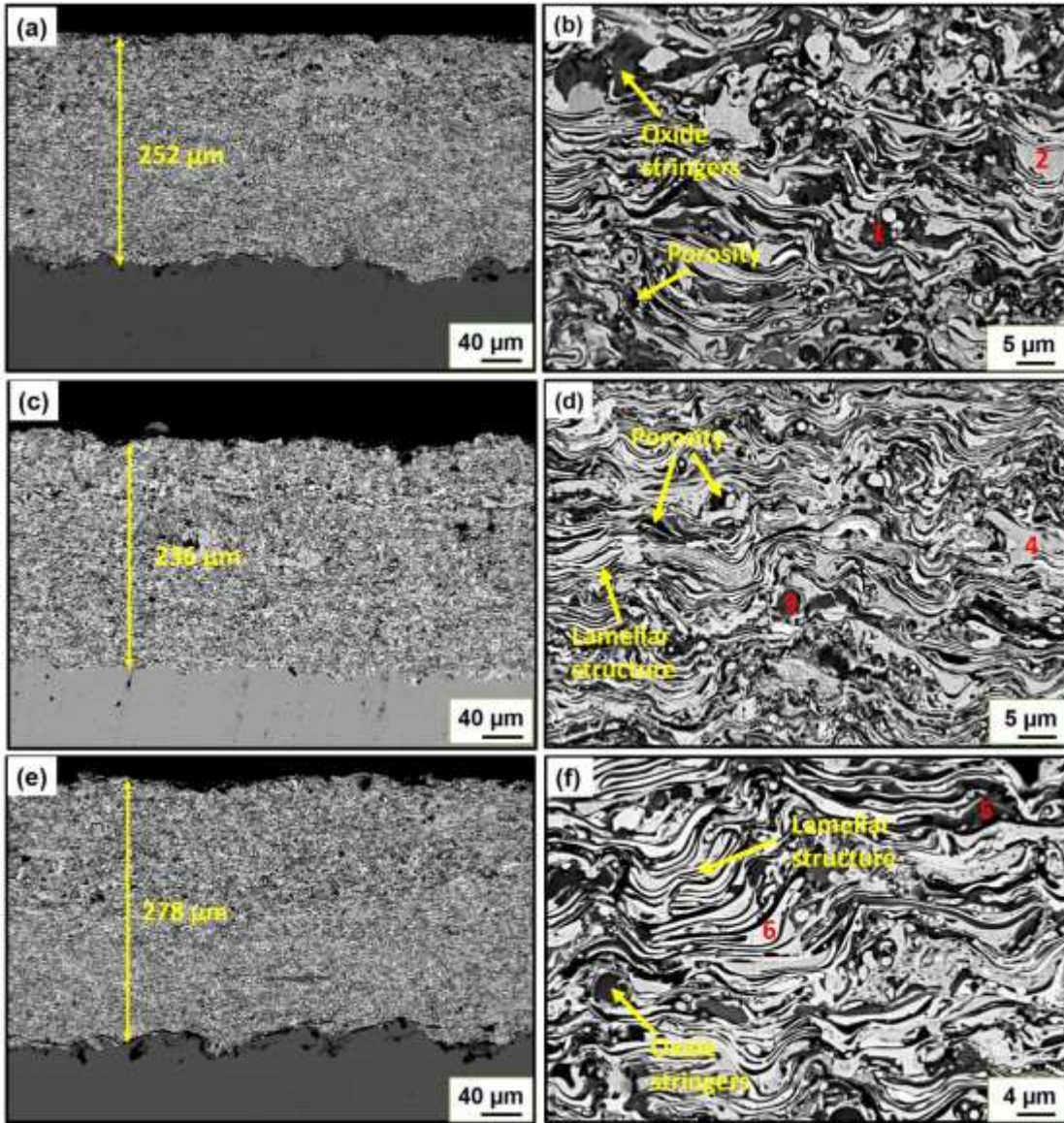


Figure 5.10 Cross-sectional microstructure of (a), (b) CoCrNiTiW<sub>0.5</sub> and (c), (d) CoCrNiTiW and (e), (f) CoCrNiTiW<sub>1.5</sub> HEA coatings.

The porosities of CoCrNiTiW<sub>0.5</sub>, CoCrNiTiW, and CoCrNiTiW<sub>1.5</sub> HEA coatings were found to be  $1.31 \pm 0.32$  %,  $1.19 \pm 0.03$  % and  $1.25 \pm 0.37$  % respectively. Fabrication defects including the pores and minor cracks were inevitable in thermal spray deposition, owing to the solidification induced defects arising from the mismatch in coefficient of thermal expansion of the coating and substrate (Hsu et al. 2017b). Further, the rapid solidification at the interface restricts the escape of entrapped oxides and gases, adding to the porosity. Table 5.2 shows the corresponding elemental compositions of highlighted spots in Figure 5.10, as determined by EDS analysis. It

was observed that the dark spots (spots 1,3 & 5) in the microstructure were oxy-rich regions, and the grey spots (spots 2,4 & 6) were enriched with all the constituent elements, representing the actual composition of the HEA.

Table 5.2 Chemical composition of highlighted points in Figure 5.10 (at %).

Point	Co	Cr	Ni	Ti	W	O
1	6.7	14.7	6.1	12.2	3.2	57.1
2	22.1	21.4	20.9	7.5	14.4	12.3
3	1.8	14.6	1.1	11.0	4.4	67.1
4	21.2	20.4	19.9	6.5	19.6	11.1
5	3.4	13.4	2.7	13.1	5.7	61.8
6	28.5	6.4	20.4	2.5	33.0	9.0

The nature of bonding of the as-sprayed HEA coating with that of the substrate can be analyzed from the interfacial SEM images in Fig. 5.11. The grit-blasted substrate possessing a rough surface with wavy nature can be seen at the interface.

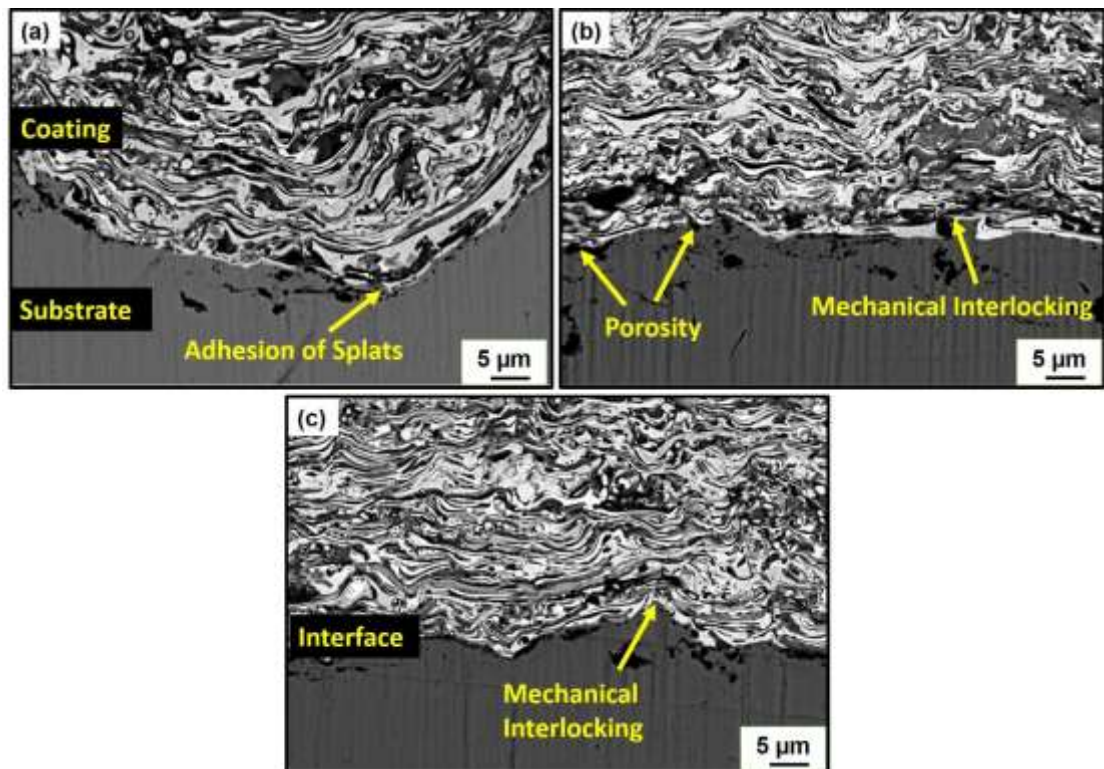


Figure 5.11 Interfacial bonding of (a) CoCrNiTiW<sub>0.5</sub> and (b) CoCrNiTiW and (c) CoCrNiTiW<sub>1.5</sub> HEA coating with the substrate.

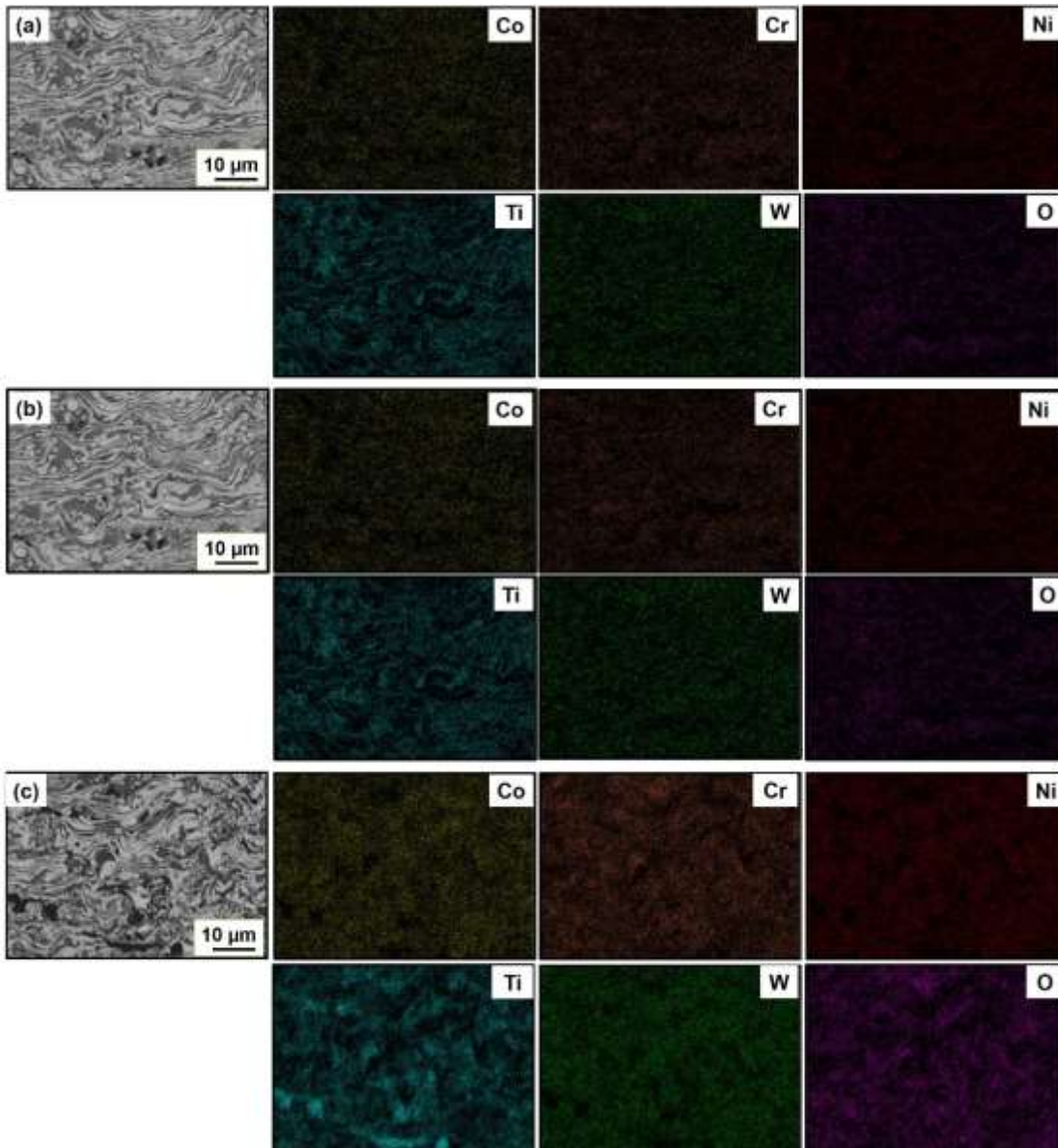


Figure 5.12 Elemental mapping of (a) CoCrNiTiW<sub>0.5</sub>, (b) CoCrNiTiW and (c) CoCrNiTiW<sub>1.5</sub> HEA Coating cross-section.

The interaction of the wavy nature of the substrate with that of incoming molten splats during coating deposition resulted in a good adhesion of the coatings with the substrate. The mechanical interlocking of the solidified splats with the substrate surface can be identified in Figure 5.11. The interfacial SEM analysis corroborate the good adhesion of the coating with the substrate. To further characterize the coating microstructure and identify the distribution of alloying elements, elemental mapping was performed on the coatings cross-section (Figure. 5.12). Based on the EDS maps, it appears that all the

alloying elements are evenly distributed throughout the cross-section. Additionally, the dark spots scattered all over the cross-section were identified as oxide stringers enriched with Ti, Cr and Ni oxides.

### 5.2.3 XRD studies

The X-ray diffraction patterns of CoCrNiTiW<sub>0.5</sub>, CoCrNiTiW and CoCrNiTiW<sub>1.5</sub> coatings were depicted in Figure 5.13. The BCC solid solution phase of the milled feedstock has been retained after the development of coatings. However, an additional intermetallic phase Co<sub>3</sub>Ti (PDF# 03-065-4116) for CoCrNiTiW<sub>0.5</sub>, and Cr<sub>7</sub>Ni<sub>3</sub> (PDF# 00-051-0637) for CoCrNiTiW<sub>1.5</sub> HEA coatings can be seen. The formation of intermetallic phases can also be seen in other HEAs, resulting in improved hardness and mechanical properties (Chen et al. 2019c; Joseph et al. 2020; Liu et al. 2016). Due to the higher operating temperatures and kinetic energies involved in the HVOF spray deposition, the feedstock is subjected to oxidation (Li et al. 2017; Meghwal et al. 2022).

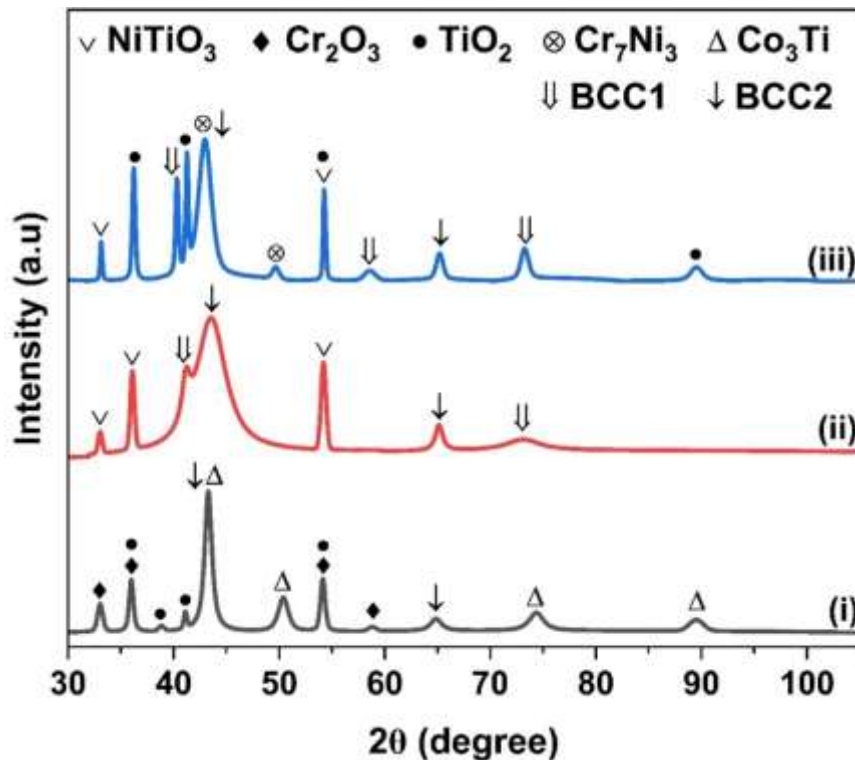


Figure 5.13 XRD analysis of HVOF sprayed (i) CoCrNiTiW<sub>0.5</sub> and (ii) CoCrNiTiW and (iii) CoCrNiTiW<sub>1.5</sub> HEA coatings.

The CoCrNiTiW<sub>0.5</sub> HEA coating reports the formation of Cr<sub>2</sub>O<sub>3</sub> (PDF# 01-084-0315), and TiO<sub>2</sub> (PDF# 01-076-0319), while the CoCrNiTiW<sub>1.5</sub> forms NiTiO<sub>3</sub> spinel (PDF# 01-076-0334), and TiO<sub>2</sub> (PDF# 01-076-0319). Further, the equimolar CoCrNiTiW HEA coating showed the presence of two BCC solid solutions (PDF# 01-089-4900), (PDF# 01-085-1336) and NiTiO<sub>3</sub> spinel. Broadening of the diffraction peaks can also be witnessed in the x-ray diffractogram of the deposited HEA coatings, owing to the grain refinement. The higher cooling rates in the thermal spray deposition techniques lead to a reduction in the grain sizes of the deposited splats (Chen et al. 2019a; Li et al. 2017; Zhou et al. 2022). Due to the lesser W content, the CoCrNiTiW<sub>0.5</sub> HEA reported the formation of a single BCC solid solution. Contrarily, the presence of higher molar fractions of tungsten in CoCrNiTiW<sub>1.5</sub> HEA reported the formation of two BCC solid solution phases.

#### 5.2.4 Microhardness

Figure 5.14 shows the microhardness of CoCrNiTiW<sub>0.5</sub>, CoCrNiTiW and CoCrNiTiW<sub>1.5</sub> HEA coatings using a Vickers indenter following ASTM E 384 standards. The indentations were made on the polished cross-sections at 50  $\mu\text{m}$  intervals, starting from the substrate and progressing towards the coating surface. It was observed that the microhardness values at the substrate ranged from 410-440 HV<sub>0.3</sub>. The hardness at the interface is influenced by both the substrate and coating and hence its value lies intermediate to the hardness values of the substrate and coating. Excluding the microhardness at the interface, the microhardness of CoCrNiTiW<sub>0.5</sub> coating varied from  $823 \pm 51$  to  $901 \pm 49$  HV<sub>0.3</sub>. Simultaneously, CoCrNiTiW<sub>1.5</sub> showed an increment from  $955 \pm 48$  to  $1087 \pm 53$  HV<sub>0.3</sub> (Figure 5.14b).

The variation in the microhardness values at different distances from the interface is mainly attributed to the microstructural heterogeneity, owing to the distribution of different phases (Liu et al. 2022a). The x-ray diffraction data from Figure 5.13 confirmed the presence of single BCC solid solution, Co<sub>3</sub>Ti phases for CoCrNiTiW<sub>0.5</sub> and two BCC solid solutions and Cr<sub>7</sub>Ni<sub>3</sub> phase for CoCrNiTiW<sub>1.5</sub> HEA's. Apart from the heterogeneous distribution of phases, the significant variation in the microhardness along the thickness of the coatings might be due to the presence of porosity, oxides, unmelted and semi-melted particles, inclusions in the microstructure, and layered

structure of the coatings. Similar observations in the microhardness values were also seen in other HVOF sprayed coatings (Jin et al. 2018b; Tian 2016).

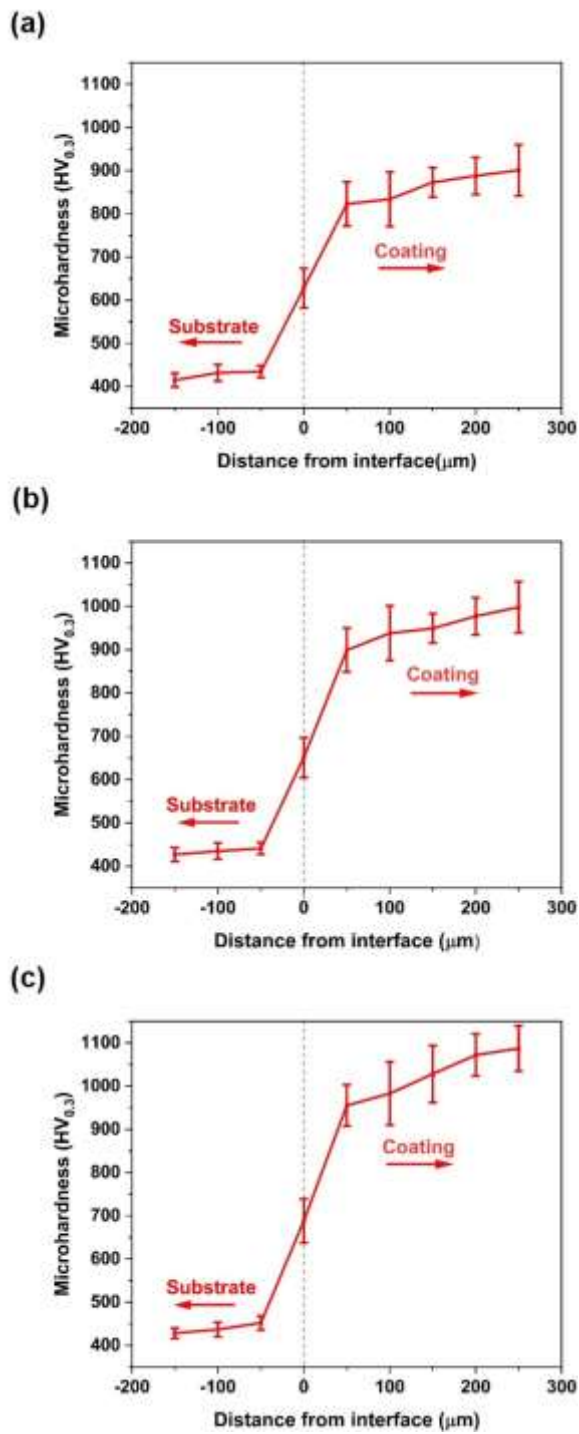


Figure 5.14 Vickers microhardness of (a) CoCrNiTiW<sub>0.5</sub>, (b) CoCrNiTiW and (c) CoCrNiTiW<sub>1.5</sub> HEA coating.

The average microhardness values of CoCrNiTiW<sub>0.5</sub>, CoCrNiTiW and CoCrNiTiW<sub>1.5</sub> HEA coatings were found to be 863±52 HV<sub>0.3</sub>, 951 ± 38 HV<sub>0.3</sub> and 1025±39 HV<sub>0.3</sub> respectively. The substantial rise in the microhardness of CoCrNiTiW<sub>1.5</sub> HEA is ascribed to the presence of additional BCC solid solution phase (Fig. 5.13). BCC phases, possessing lesser slip systems, acts as barriers for the movement of dislocations. Therefore, the plastic deformation of the system is restricted, leading to an enhancement in strength and hardness (Meghwal et al. 2022).

### 5.2.5 Fracture toughness

Figure 5.15 shows the formation of cracks, emerging from the tips of the Vickers indenter and parallel to the coating-substrate interface.

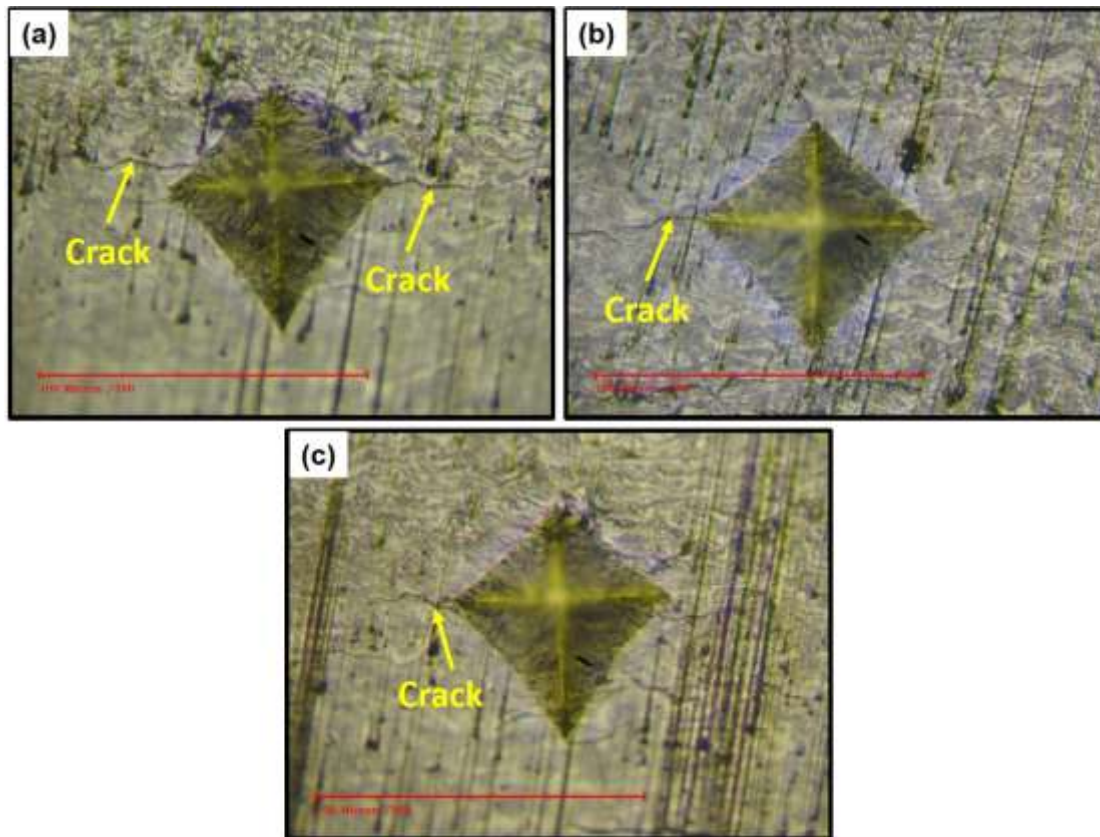


Figure 5.15 Optical microscopy showing the cracks generated for (a) CoCrNiTiW<sub>0.5</sub>, (b) CoCrNiTiW and (c) CoCrNiTiW<sub>1.5</sub> HEA coatings during the indentation fracture toughness test.

The results reveal that the fracture toughness of CoCrNiTiW<sub>0.5</sub>, CoCrNiTiW and CoCrNiTiW<sub>1.5</sub> HEA coatings were found to be 3.22 ± 0.26 (Mpa m<sup>1/2</sup>), 3.54 ± 0.32

( $\text{Mpa m}^{1/2}$ ) and  $3.87 \pm 0.3$  ( $\text{Mpa m}^{1/2}$ ) respectively. The reported values were found to be higher than the other thermal sprayed coatings (Lin et al. 2015; Ndumia et al. 2023). A higher fracture toughness value indicates the coating's resistance to crack propagation. In the context of sliding wear, where surfaces are subjected to repeated friction and contact stresses, a coating with high fracture toughness is generally more resistant to cracking and failure.

### 5.2.6 Surface roughness and density

The 3-dimensional roughness plots of the deposited coatings can be seen in Figure 5.16.

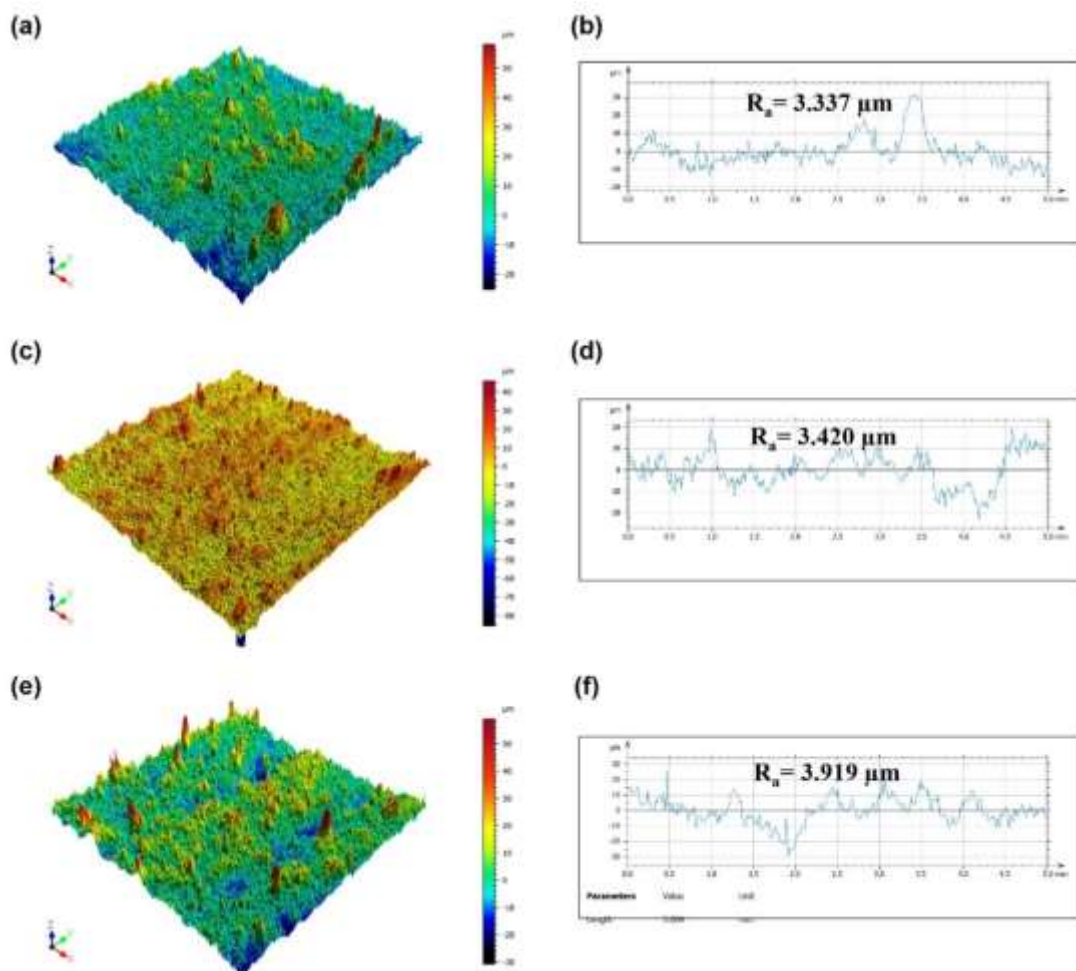


Figure 5.16 Profilometry studies showing the 3-dimensional roughness plot of (a)  $\text{CoCrNiTiMo}_{0.5}$ , (c)  $\text{CoCrNiTiMo}$ , and (e)  $\text{CoCrNiTiMo}_{1.5}$  HEA coatings. Corresponding 2D line profiles can be seen in (b), (d), (f) respectively.

The average surface roughness of CoCrNiTiW<sub>0.5</sub>, CoCrNiTiW and CoCrNiTiW<sub>1.5</sub> HEA coatings were found to be 3.337  $\mu\text{m}$ , 3.420  $\mu\text{m}$  and 3.919  $\mu\text{m}$ , respectively. Furthermore, the average densities of CoCrNiTiW<sub>0.5</sub>, CoCrNiTiW and CoCrNiTiW<sub>1.5</sub> HEA coatings, as determined using ASTM C 135 standards, were found to be 7.93  $\text{g}/\text{cm}^3$ , 9.27  $\text{g}/\text{cm}^3$  and 10.17  $\text{g}/\text{cm}^3$ , respectively.

### **5.3 Summary**

CoCrNiTiMo<sub>x</sub> (x=0.5,1,1.5) and CoCrNiTiW<sub>x</sub> (x=0.5,1,1.5) HEA coatings were successfully deposited on maraging steel substrate by HVOF spray technique. The deposited coatings were characterized with respect to their microstructure and mechanical performance. The microstructural characterization was accomplished by XRD analysis, SEM and EDS techniques. The mechanical characterization includes microhardness, fracture toughness and surface roughness analysis. The physical parameters such as density and porosity of the deposited coatings were assessed. The effect of variation in the molar fractions of Molybdenum and Tungsten on the phase formation, microhardness and fracture toughness is thoroughly investigated. The results indicate a significant enhancement in the mechanical performance of the deposited HEA coatings with an increase in the molar fractions of Molybdenum and Tungsten.

## CHAPTER 6

### TRIBOLOGICAL STUDIES

#### 6.1 High Temperature tribological behaviour of CoCrNiTiMo<sub>x</sub> HEA Coatings

##### 6.1.1 Frictional coefficient plots

Figure 6.1 shows the representative friction coefficient graphs of CoCrNiTiMo<sub>0.5</sub>, CoCrNiTiMo and CoCrNiTiMo<sub>1.5</sub> HEA coatings at different loading conditions and temperatures. Figure 6.1b shows the friction coefficient variation of CoCrNiTiMo<sub>0.5</sub> HEA coating with respect to sliding time at a normal load of 4 kg under different temperatures. It can be observed that there were two stages in the friction coefficient graph at any particular temperature. The initial stage, usually called the run-in stage, lasted around 250 s at room temperature. During the run-in stage, a rapid and steep increase in friction coefficient values has been seen, owing to the breaking of worn surface and growth in contact area (Nguyen et al. 2022). The final stage is the stable state, where the friction coefficient values become more stable and fluctuates between narrow ranges.

The CoCrNiTiMo<sub>0.5</sub> coating exhibited an average steady-state friction coefficient of  $0.57 \pm 0.039$  at room temperature and  $0.45 \pm 0.045$  at 600°C. From the Figure 6.1b, it is obvious that the CoCrNiTiMo<sub>0.5</sub> HEA coatings showed a drop in the friction coefficient values with an increase in temperature. The frictional coefficients of CoCrNiTiMo HEA coatings under normal loading of 4kg decreased from  $0.52 \pm 0.014$  to  $0.44 \pm 0.006$ , with a temperature rise from RT to 600°C. Similarly, CoCrNiTiMo<sub>1.5</sub> HEA coating also showed a reduction in the friction coefficient values from  $0.60 \pm 0.042$  to  $0.43 \pm 0.047$  at an elevated temperature of 600°C (Figure 6.1f). The reduction in the friction coefficient values at high temperature may be attributed to the formation of oxide layer on the worn surface. The oxide films reduce contact surface adhesion and provide a self-lubricating effect (Li et al. 2022; Miao et al. 2021; Xiao et al. 2020c). The as-sprayed coatings friction coefficient values at 200°C and 400°C wear test lie between RT and 600°C. Additionally, the reduction in frictional coefficients at elevated temperatures is noticeable even under a normal load of 2 kg.

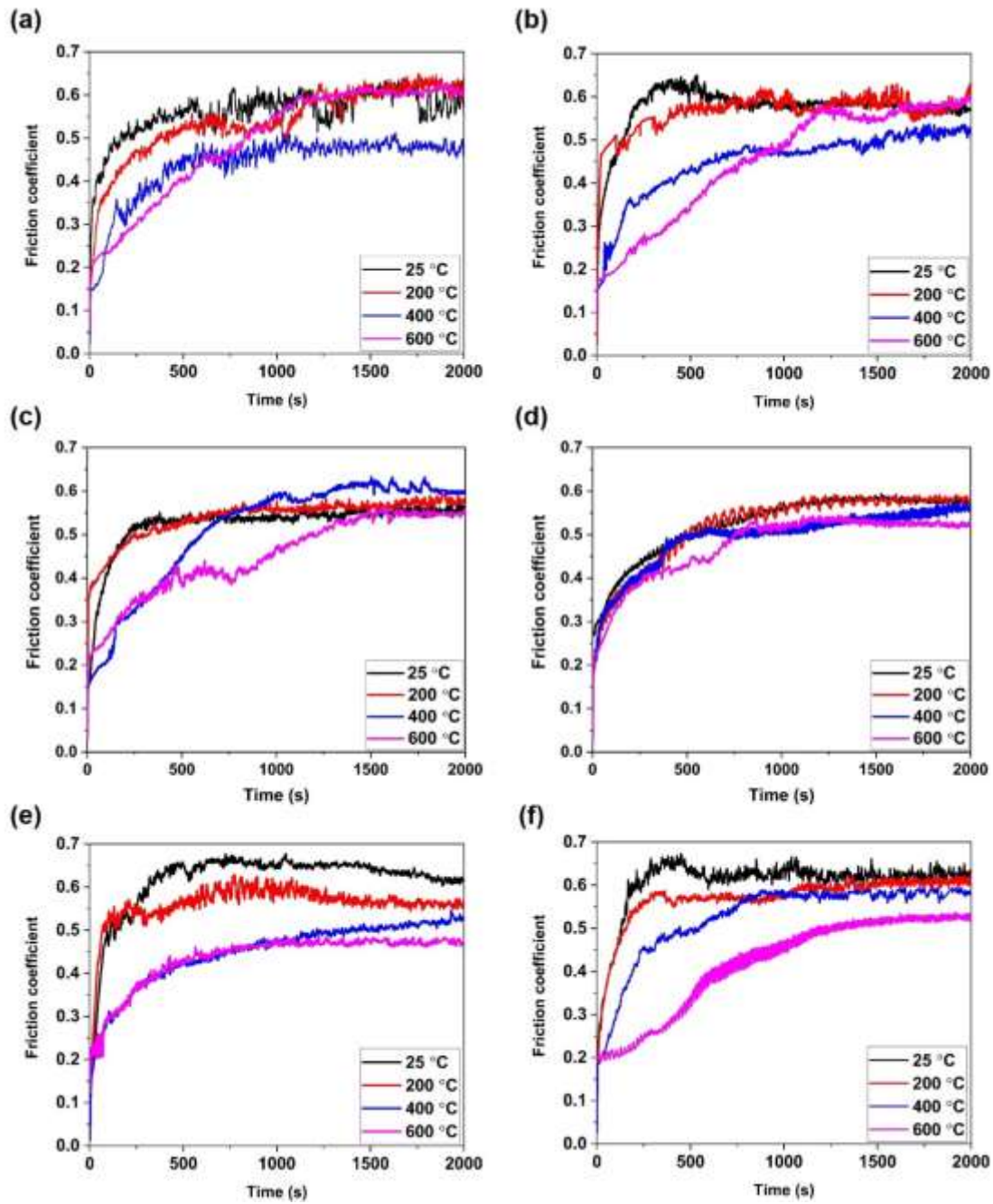


Figure 6.1 Friction coefficient plots of worn-out samples at different temperatures for CoCrNiTiMo<sub>0.5</sub> at (a) 2kg (b) 4kg, CoCrNiTiMo at (c) 2 kg (d) 4 kg and CoCrNiTiMo<sub>1.5</sub> at (e) 2 kg (f) 4 kg loading condition.

From Fig. 6.1b, it can also be observed that the duration of the run-in period was influenced by sliding temperature. The run-in period, initially 250 s at RT, increased to 400 s at a temperature of 200°C. The running-in time for the wear test at 400°C and

600°C was 900 and 1170 s, respectively. These prolonged running-in periods at high temperatures can be attributed to the continuous formation and breakdown of the oxide layer. The formation of tribofilms suppresses the steep increase of the frictional forces, enabling them to take longer times before attaining a steady state. The steady state for CoCrNiTiMo HEA coatings at RT was attained at around 220 s. Nevertheless, for wear tests conducted at 200 °C, 400 °C, and 600 °C, the steady states were reached after 518 s, 890 s, and 1255 s, respectively (Figure 6.1c). A similar trend can be observed for the frictional coefficient values of the CoCrNiTiMo<sub>1.5</sub> coatings at different temperatures. From Figure 6.1f, the CoCrNiTiMo<sub>1.5</sub> coatings exhibited a pronounced increase in the running-in time for the wear tests conducted at 400°C and 600°C. The Run-in times increased from 270 s at room temperature to 1280 s at 600°C.

### 6.1.2 Specific wear rate

The specific wear rates of CoCrNiTiMo<sub>0.5</sub>, CoCrNiTiMo, CoCrNiTiMo<sub>1.5</sub> HEA coatings, and maraging steel substrate with respect to temperature and load were presented in Figure 6.2. The effect of normal load on the specific wear rates of the substrate is significant when compared to that of as-sprayed coatings, at room temperatures. From Figure 6.2, the maraging steel substrate reported a drastic increase in the specific wear rate from  $51.92 \pm 3.7 \times 10^{-6} \text{ mm}^3/\text{N-m}$  to  $82.3 \pm 5.6 \times 10^{-6} \text{ mm}^3/\text{N-m}$ , with a rise in the load from 2kg to 4kg. The frictional heat and contact pressures generated at the interface plastically deform the softer material, leading to abrasion of surface layers (Medabalimi et al. 2021).

In contrast, the CoCrNiTiMo<sub>0.5</sub> coating showed a meagre increase in the wear rate from  $22.49 \pm 2.6 \times 10^{-6} \text{ mm}^3/\text{N-m}$  to  $28.05 \pm 2.8 \times 10^{-6} \text{ mm}^3/\text{N-m}$ . Further, the increase of Mo atomic fraction on the specific wear rates showed better wear resistance at any given temperature and load (Figure 6.2a&b). The CoCrNiTiMo HEA coating only experienced a marginal rise in wear rates from  $17.34 \pm 2.8 \times 10^{-6} \text{ mm}^3/\text{N-m}$  to  $21.23 \pm 3.1 \times 10^{-6} \text{ mm}^3/\text{N-m}$ . Further, the CoCrNiTiMo<sub>1.5</sub> HEA exhibited a rise from  $12.73 \pm 2.7 \times 10^{-6} \text{ mm}^3/\text{N-m}$  to  $17.39 \pm 3.1 \times 10^{-6} \text{ mm}^3/\text{N-m}$ , with with a rise in the load from 2kg to 4kg. The variations in hardness levels among these materials clarify the notable differences in wear rates between the substrate and coatings. The high wear resistance of CoCrNiTiMo<sub>1.5</sub> HEA can be attributed to its high microhardness of 952 HV<sub>0.3</sub>.

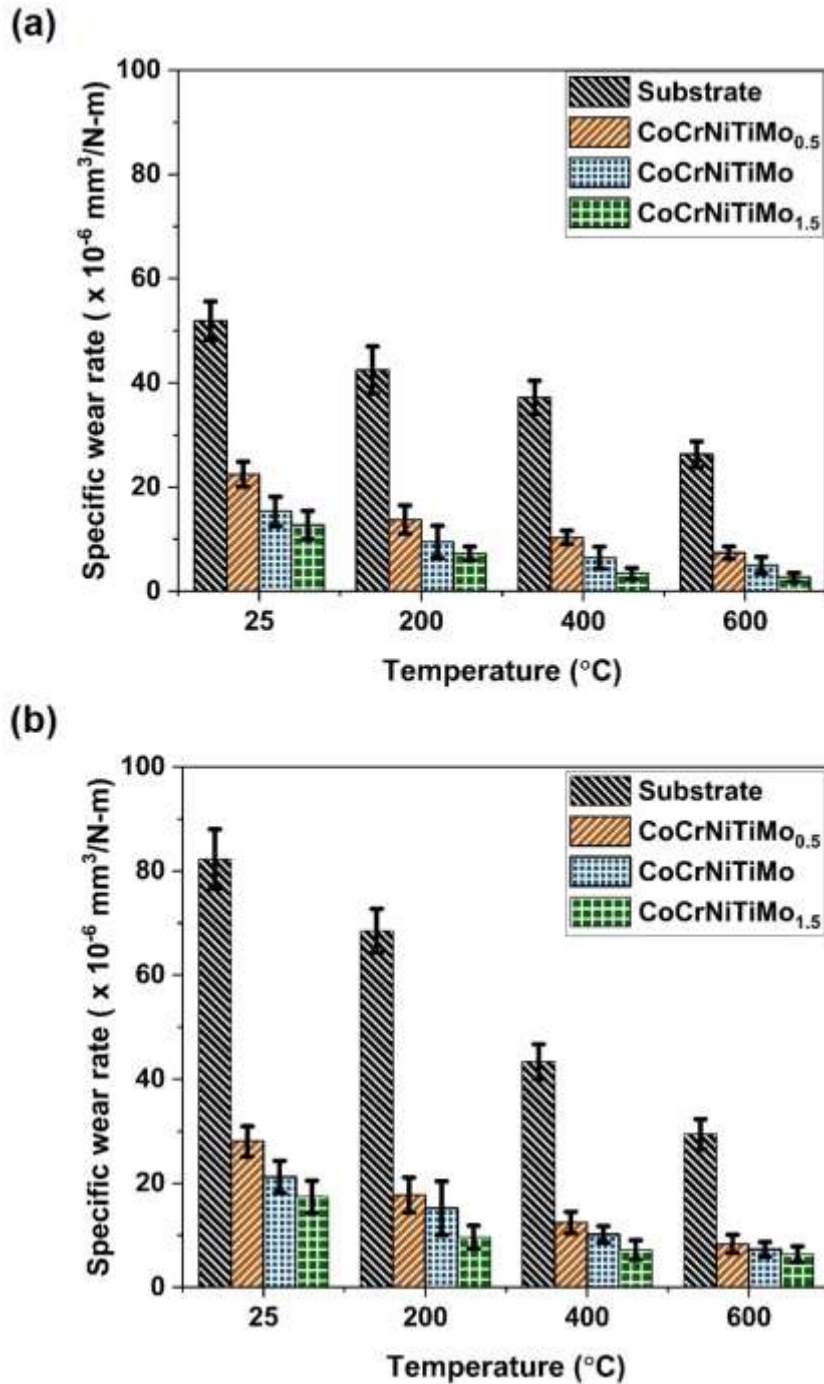


Figure 6.2 Specific wear rate plots of Substrate and  $\text{CoCrNiTiMo}_x$  HEA coatings at (a) 2kg normal load and (b) 4kg normal load.

Further, the temperature rise of the interphase, during room temperature wear tests is analysed to check the effect of frictional heat on the sample. It was seen that the temperature rise is minimal and has been limited to 2-3  $^{\circ}\text{C}$ , indicating the generation of

lesser frictional heat at the interphase. The lesser frictional heat generated in the current study may be attributed to the lesser sliding speeds and loading conditions. The rise in temperature of the interface during pin-on disc wear test depends on several factors including the sliding distance, sliding speed and sliding pairs used.

It can be seen from Figure 6.2a&b that the specific wear rates of CoCrNiTiMo<sub>x</sub> (x=0.5, 1 and 1.5) and substrate decrease with a rise in wear temperature. The specific wear rates of CoCrNiTiMo<sub>0.5</sub> HEA coating, at a normal load of 4kg, decreased by 70.3%, from  $28.05 \pm 2.9 \times 10^{-6} \text{ mm}^3/\text{N-m}$  to  $8.33 \pm 1.8 \times 10^{-6} \text{ mm}^3/\text{N-m}$ , when the temperature is increased to 600°C from room temperature. The CoCrNiTiMo HEA coating's wear rate dropped by 65.6%, from  $21.23 \pm 3.1 \times 10^{-6} \text{ mm}^3/\text{N-m}$  to  $7.3 \pm 1.4 \times 10^{-6} \text{ mm}^3/\text{N-m}$ . Similarly, there is a drop in the specific wear rate of CoCrNiTiMo<sub>1.5</sub> HEA coating by 63.4%, from  $17.39 \pm 3.1 \times 10^{-6} \text{ mm}^3/\text{N-m}$  to  $6.36 \pm 1.5 \times 10^{-6} \text{ mm}^3/\text{N-m}$  after the temperature is raised to 600°C. The decreasing trend of the specific wear rates with respect to temperature was mainly attributed to the formation of tribofilms on the worn surface.

### 6.1.3 Wear mechanisms

The worn surfaces of the as-sprayed coatings were investigated using secondary electron imaging mode in scanning electron microscopy to understand the wear behavior and underlying wear mechanisms. The wear mechanisms for CoCrNiTiMo<sub>0.5</sub> HEA coatings at different temperatures can be analyzed from Figure 6.3. A significant number of grooves can be observed on the worn surfaces after the wear test at room temperature, indicating dominant abrasive wear mechanism (Figure 6.3a). Whereas, the wear test at 200°C, shows several spalling pits along with the abrasive grooves. The debris particles were slightly bigger and multiplied compared to those at room temperature (Figure 6.3b). The EDS results on the spalling pits and debris showed a significant contribution of Aluminium, indicating adhesion of the counter surface onto the worn surface (Table 6.1). The compaction of the pulled-out debris particles between the sample surface and counter face leads to adhesion of the particles due to the frictional heat generated at the contact surfaces (Alvi i Akhtar 2019). Therefore, the wear rate at 200°C is dominated by the combined effects abrasive and adhesive wear.

The wear test, at 400°C, showed crack formation on the surface. Delamination of the worn surface can also be witnessed in Figure 6.3c, implying the fatigue wear mechanism. Dark patches on the worn surface can also be occasionally seen. The EDS data indicates high levels of oxygen present in the dark regions, confirming oxidative wear. Therefore, the wear at 400°C is due to the combined effects of fatigue and oxidative wear. After wear testing at 600°C, the worn surface reported an increase in the number of cracks on the surface. However, the delamination sites have been reduced, and a relatively smoother surface can be seen in Figure 6.3d. A pronounced dark layer was found to be spread across the worn surface. The EDS data from Table 6.1 validates the substantial quantities of oxygen on the worn surface, indicating an oxidative wear mechanism (Jin et al. 2022).

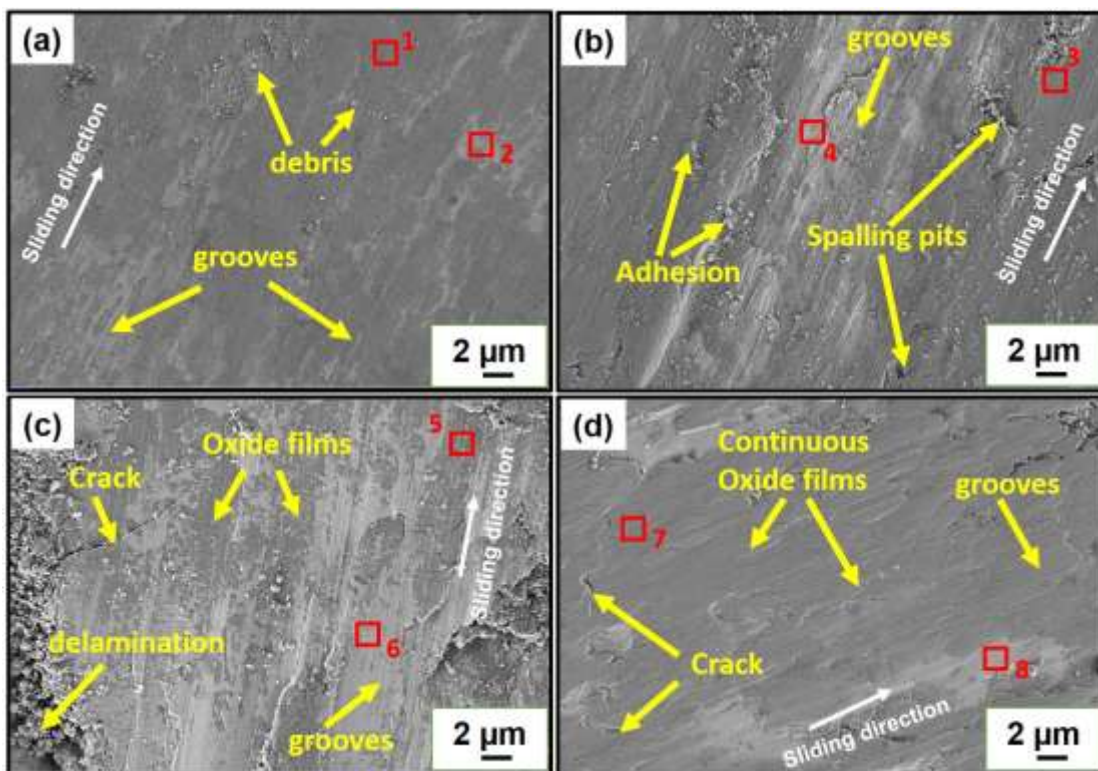


Figure 6.3 SEM images showing the wear mechanisms of CoCrNiTiMo<sub>0.5</sub> HEA worn surfaces at a) RT b) 200 °C c) 400 °C d) 600 °C in secondary electron imaging mode.

Fig. 6.4 reveals the surfaces of CoCrNiTiMo HEA coatings after wear testing at different temperatures. The micrographs of CoCrNiTiMo demonstrated many grooves aligned in the sliding direction during wear testing at room temperature, implying an

abrasive wear mechanism (Joseph et al. 2019). Moreover, the surface of the worn samples occasionally displays adhered debris particles (Figure 6.4a). The EDS analysis uncovers the presence of Al, which was transferred from the Alumina counter body. Table 6.2 depicts the compositions of all the labelled points in Figure 6.4. Following wear testing at 200 °C, the adherence of loose debris particles is predominant, confirming the adhesive wear mechanism (Figure 6.4b). The extended contact and inadequate lubrication resulted in the adherence of the transferred debris particles from the counterface.

Table 6.1 EDS analysis of specified points in Figure 6.3 showing the chemical compositions in at%

Sliding temperature	Point	Chemical composition (at %)						
		Co	Cr	Ni	Ti	Mo	O	Al
RT	1	10.7	14.6	10.8	12.3	9.7	35.4	6.7
	2	26.3	20.8	25.6	8.2	11.7	6.8	0.6
200 °C	3	12.2	10.4	11.7	9.3	6.6	38.6	11.2
	4	21.9	21	19.9	18	8.9	10.2	0.13
400 °C	5	10.7	8.9	9.2	8.7	4.2	44.3	14
	6	14.7	15.3	13.7	15.6	5.4	30.2	5.1
600 °C	7	4.9	13.4	5.1	13.3	6.2	54.8	2.3
	8	10.7	21.4	10.9	17.3	15.4	22.7	1.3

It is apparent from the worn surfaces at 400 °C that the surface exhibits minor cracks and deformation. Fatigue wear is primarily characterized by the absence of cohesion among the splats, resulting in delamination of the weakly bonded layers (Singh et al. 2019). Nevertheless, there are no visible signs of delamination on the surface, indicating that the level of fatigue wear is minimal. In addition, the surface features numerous abrasive grooves. Therefore, the wear at 400 °C is due to fatigue and abrasive wear mechanisms. A consistent oxide layer was observed on the surface after performing the wear test at 600 °C (Figure 6.4d). The surface had a refined appearance with fewer debris particles and a smoother texture. The oxide tribofilms inhibit adhesion between friction pairs, decreasing surface roughness (Cheng et al. 2020). Consequently, there was a significant decrease in COF and wear rates, as depicted in Figure 6.1 & Figure 6.2 The EDS analysis on the oxide tribofilms manifested significant contributions from Co, Mo, Ti and O<sub>2</sub>, implying the presence of corresponding metal oxides.

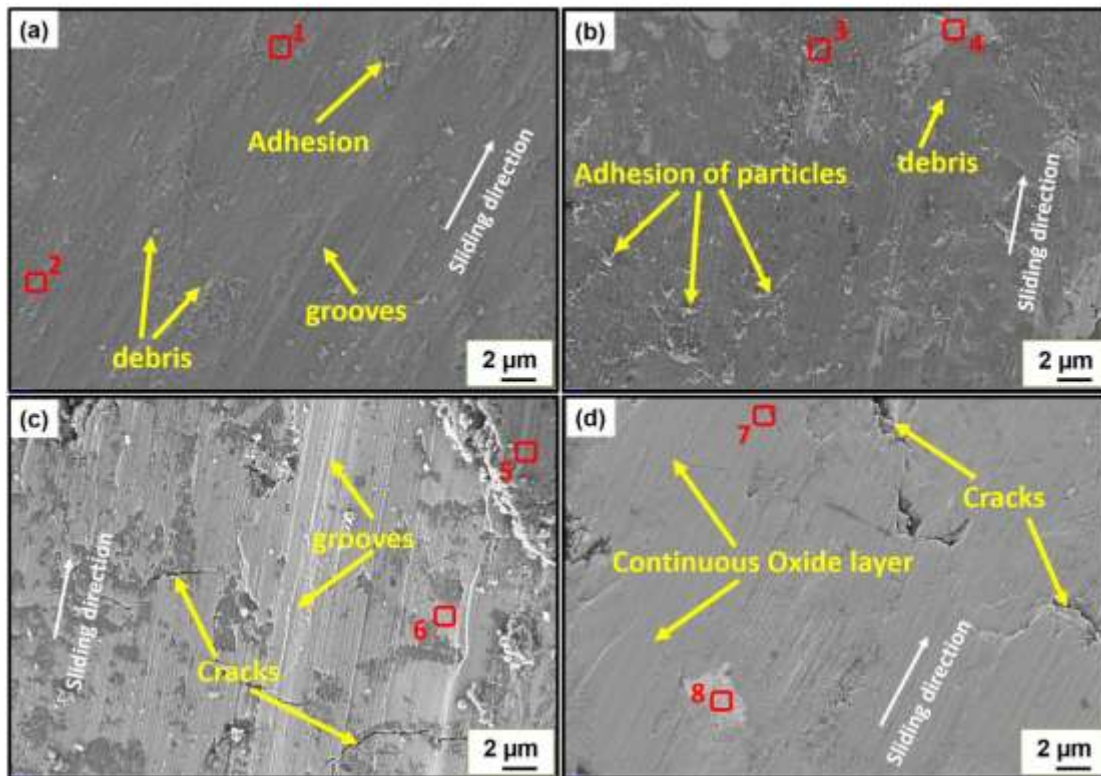


Figure 6.4 SEM images showing the wear mechanisms of CoCrNiTiMo HEA worn surfaces at a) RT, b) 200°C, c) 400°C, d) 600°C in secondary electron imaging mode.

Table 6.2 EDS analysis of specified points in Figure 6.4 showing the chemical compositions in at%

Sliding temperature	Point	Chemical composition (at %)						
		Co	Cr	Ni	Ti	Mo	O	Al
RT	1	11.24	14.09	12.65	12.48	9.36	27.46	12.71
	2	26.65	20.23	25.95	3.22	11.93	11.43	0.6
200 °C	3	12.2	12.41	11.77	12.31	6.65	30.43	14.23
	4	21.04	21.7	19.8	18.09	8.90	10.35	0.13
400 °C	5	12.78	10.98	11.51	10.25	5.53	44.77	4.19
	6	14.72	15.36	13.48	15.7	5.4	30.28	5.06
600 °C	7	9.23	3.28	11.16	12.54	8.82	54.07	0.9
	8	12.11	17.12	10.22	15.07	8.78	36.20	0.49

Unlike CoCrNiTiMo<sub>0.5</sub> HEA coatings, the CoCrNiTiMo<sub>1.5</sub> HEA coatings exhibited a dominant adhesive wear mechanism at room temperature. The adhesive wear can be quantified from the spalling pits on the worn surface (Figure 6.5a). Many debris

particles can also be seen on the worn surface, along with the grooves aligned in the sliding direction. Additionally, the EDS data from Table 6.3 shows an increased presence of Al on the dark regions of the worn surface, confirming the adhesion of Al from the Al<sub>2</sub>O<sub>3</sub> counter face.

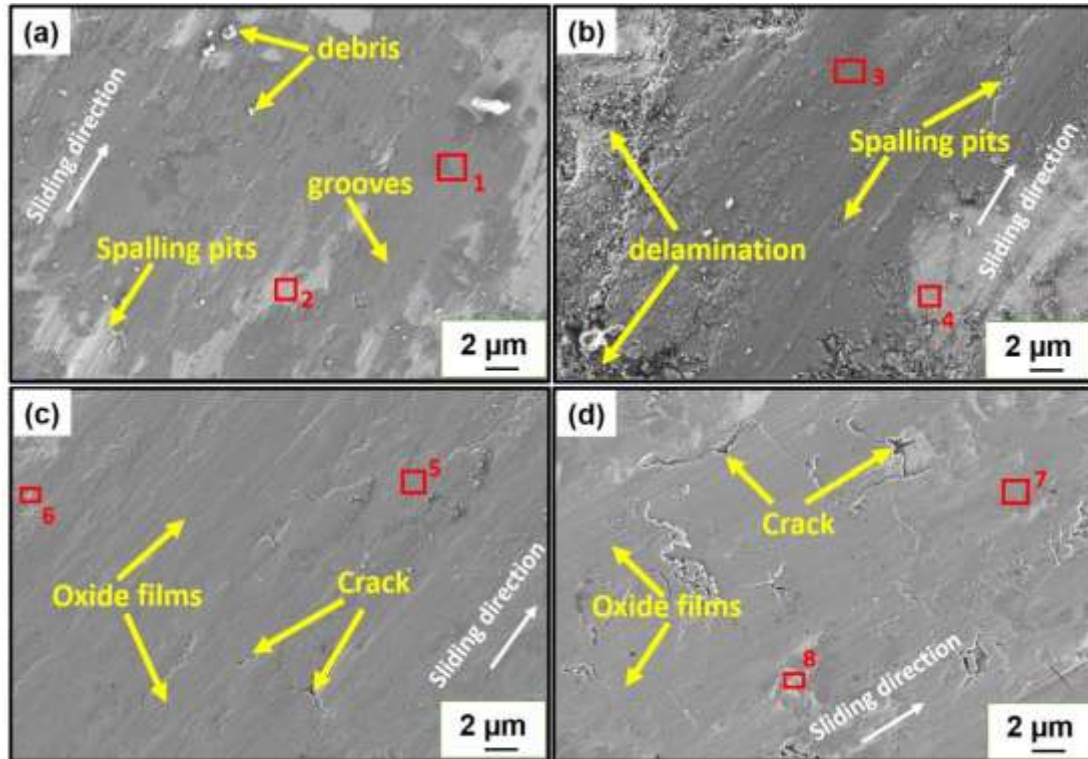


Figure 6.5 SEM images showing the wear mechanisms of CoCrNiTiMo<sub>1.5</sub> HEA worn surfaces at a) RT, b) 200°C, c) 400°C, and d) 600°C in secondary electron mode.

Table 6.3 EDS analysis of specified points in Figure 6.5 showing the chemical compositions in at%

Sliding temperature	Point	Chemical composition (at %)						
		Co	Cr	Ni	Ti	Mo	O	Al
RT	1	12.36	9.40	11.41	12.14	13.8	32.18	8.71
	2	18.03	16.51	14.92	19.73	22.06	8.47	0.28
200 °C	3	7.76	12.91	13.62	8.28	11.9	39.79	5.74
	4	15.84	19.77	15.33	19.34	18.91	9.38	1.44
400 °C	5	8.52	7.16	8.55	7.69	12.72	46.25	9.11
	6	23.57	6.16	23.63	6.85	25.39	14.32	0.07
600 °C	7	11.40	8.68	9.87	6.57	9.46	49.70	4.32
	8	13.37	14.26	12.51	15.44	12.72	31.45	0.24

The material adhesion from the counter face is significantly reduced at a test temperature of 200°C. Few delamination sites can be witnessed on the worn surface, implying the presence of fatigue wear. The debris particles were significantly high near the pulled-out regions. However, the intensity of fatigue is minimal, as can be seen in Figure 6.5b. Several grooves were spread over the worn surface, indicating minor abrasive wear and dominant fatigue wear mechanism.

The wear test at 400°C is mainly characterized by the formation of continuous oxide layers and occasional cracks over the surface. Therefore, the material removal mechanism at 400°C is due to the dominant oxidative wear and minor fatigue. Furthermore, at 600°C, the cracks increased in number, but the wear rate was controlled due to the pronounced oxide layer on the surface. The EDS data from Table 6.3 also shows the increased oxygen concentrations over the entire surface. The dark areas were mainly enriched with oxygen content, whereas the grey areas had a near-homogeneous distribution of all the constituent elements with minor oxide inclusions.

#### **6.1.4 X-Ray diffraction**

To quantify the phases formed on the worn surfaces of CoCrNiTiMo<sub>0.5</sub> HEA coatings at different temperatures, x-ray diffraction analysis has been done and shown in Fig. 6.6. It can be observed that the CoCrNiTiMo<sub>0.5</sub> HEA coatings retained the BCC phase and NiTiO<sub>3</sub> spinel formed during the HVOF spray deposition. However, an intermetallic Co<sub>3</sub>Ti (PDF# 03-065-4116) can also be seen on the worn surface at room temperature. The hard Co<sub>3</sub>Ti intermetallic, which possesses high strength and thermal stability, is responsible for enhancing the wear properties of CoCrNiTiMo<sub>0.5</sub> HEA. No new phases can be seen on the worn surface up to a temperature of 400°C. However, an increase in the spinel intensity can be seen for the wear test at 400°C, which decreases the specific wear rate. At 600°C, the wear test reveals the presence of NiMoO<sub>4</sub> tribofilms (PDF# 01-086-0361), accounting for further reduction in the wear rate.

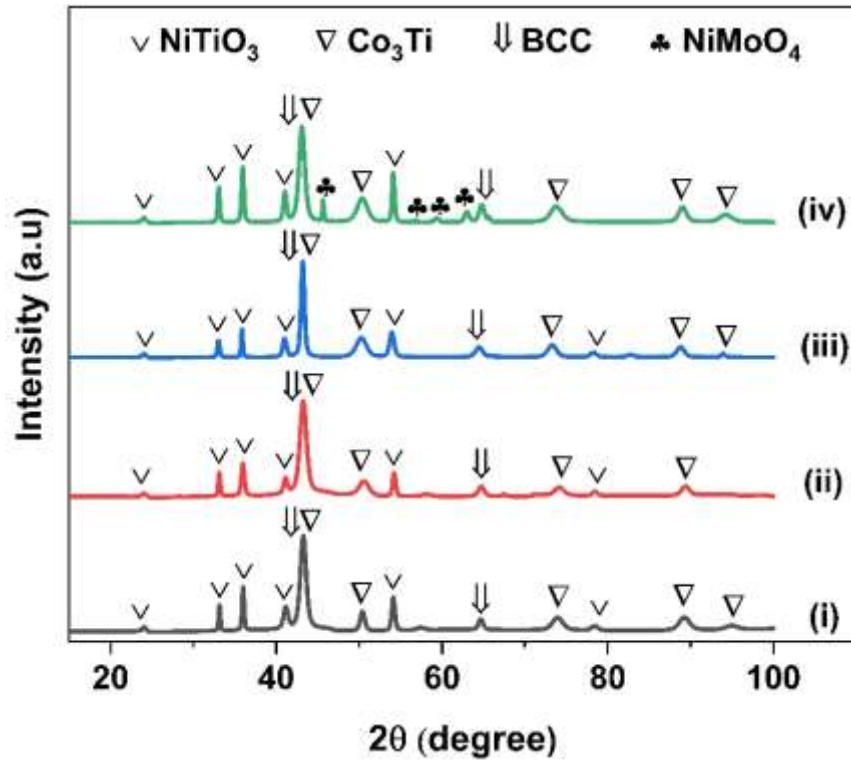


Figure 6.6 XRD analysis of CoCrNiTiMo<sub>0.5</sub> HEA Coatings after wear testing at (i) RT, (ii) 200°C, (iii) 400°C, and (iv) 600°C.

Figure 6.7 provides a clear illustration of the specific phases that were developed on the surface of CoCrNiTiMo HEAs under different temperatures. It can be seen that few of the phases formed during the coating deposition have undergone transformation and resulted in the formation of BCC phase (PDF# 01-088-2323), Mo<sub>1.24</sub>Ni<sub>0.76</sub> (PDF# 00-047-1129) and NiTiO<sub>3</sub> (PDF# 01-076-0334) at wear test conducted at room temperature. No additional phases can be seen at the 200 °C and 400 °C test temperatures. Nevertheless, the peaks have exhibited enhanced sharpness, suggesting a rise in crystallite size with temperature. Additionally, the oxide phases depicted an increment in the peak intensities at elevated temperature conditions. The wear testing at 600 °C, demonstrates the existence of hard Co<sub>3</sub>Mo (PDF# 03-065-3519) and oxide phases including CoMoO<sub>4</sub> (PDF# 00-021-0868), TiO<sub>2</sub> (PDF# 01-076-0319), NiO (PDF# 01-089-7130). The genesis of these oxide tribofilms at high temperatures is accountable for the substantial drop in specific wear rates and frictional coefficients (Chen et al. 2019a; Löbel et al. 2020).

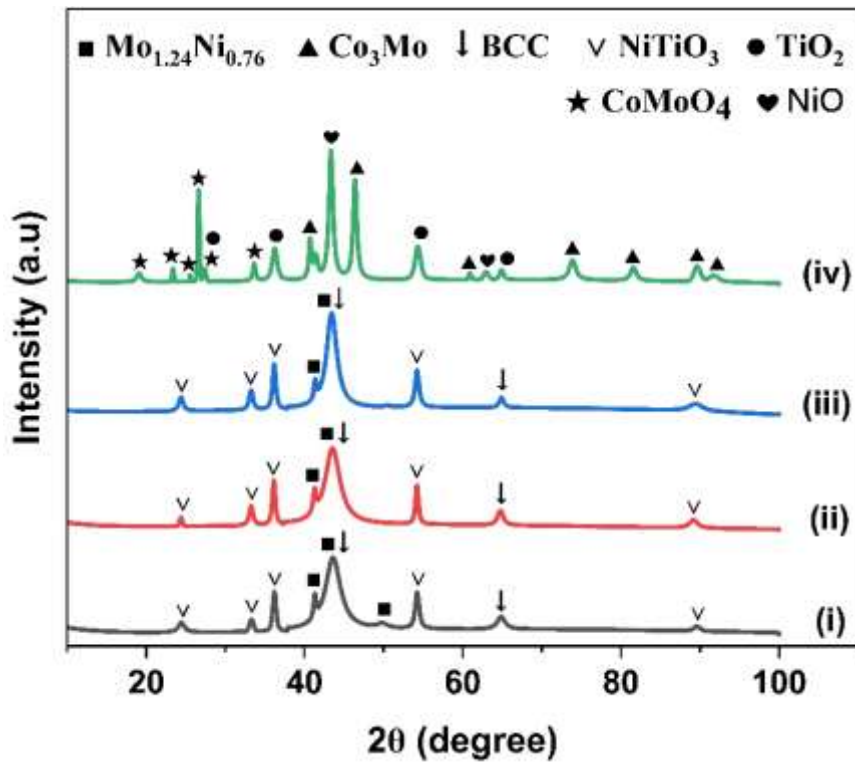


Figure 6.7 XRD analysis of CoCrNiTiMo HEA Coatings after wear testing at (i) RT, (ii) 200°C, (iii) 400°C, and (iv) 600°C.

Figure 6.8 shows the XRD analysis for CoCrNiTiMo<sub>1.5</sub> HEA coatings at different temperatures. The Co<sub>3</sub>Ti intermetallic formed in the case of CoCrNiTiMo<sub>0.5</sub> HEA has been replaced with Mo<sub>1.24</sub>Ni<sub>0.76</sub>. The formation of Mo<sub>1.24</sub>Ni<sub>0.76</sub> induces high wear resistance and thermal stability to the coating. The BCC phase and the NiTiO<sub>3</sub> spinel, formed during the HVOF spray, have been retained after the wear test at room temperature. As the temperature increases to 200°C, no new phases can be seen in the XRD. However, with a further increase in temperature to 400°C, the Mo<sub>1.24</sub>Ni<sub>0.76</sub> phase disappeared, and additional oxide phases such as MoO<sub>2</sub> (PDF# 00-050-0739) and Co<sub>3</sub>O<sub>4</sub> (PDF# 00-009-0418) can be seen. Furthermore, as the temperature rises to 600°C, an increased intensity in the MoO<sub>2</sub> peaks can be seen, enhancing the wear resistance of CoCrNiTiMo<sub>1.5</sub> HEA at high temperatures.

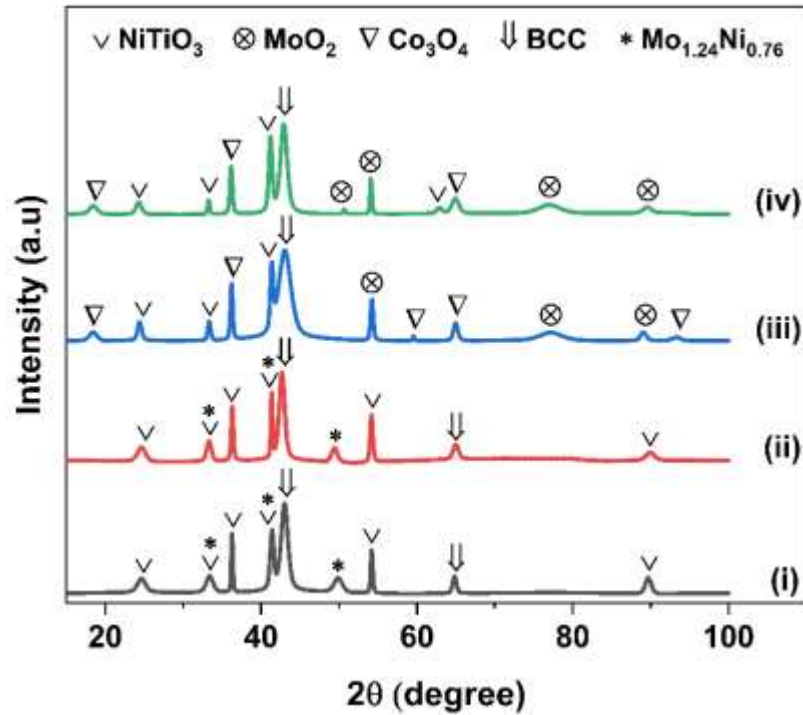


Figure 6.8 XRD analysis of CoCrNiTiMo<sub>1.5</sub> HEA Coatings after wear testing at (i) RT, (ii) 200°C, (iii) 400°C, and (iv) 600°C.

### 6.1.5 Raman Spectroscopy

Several researchers have employed Raman spectroscopy to discern the emergence of oxide phases (Guo et al. 2019; Miao et al. 2021). Accordingly, to validate the oxide phases reported in the XRD studies, Raman spectroscopy was conducted on the worn surfaces of CoCrNiTiMo<sub>x</sub> HEA coatings (Figure 6.9).

The worn surfaces of CoCrNiTiMo<sub>0.5</sub> HEAs confirmed the presence of NiTiO<sub>3</sub> (190 cm<sup>-1</sup>, 290 cm<sup>-1</sup>, 345 cm<sup>-1</sup>, and 706 cm<sup>-1</sup>) (Chellasamy i Thangadurai 2017) and NiMoO<sub>4</sub> (704 cm<sup>-1</sup>, 809 cm<sup>-1</sup>, and 960 cm<sup>-1</sup>). Likewise, the worn surfaces of CoCrNiTiMo HEA confirmed the CoMoO<sub>4</sub> (356 cm<sup>-1</sup>, 675 cm<sup>-1</sup>, 804 cm<sup>-1</sup>, 864 cm<sup>-1</sup> and 924 cm<sup>-1</sup>) (Xu et al. 2016), TiO<sub>2</sub> (144 cm<sup>-1</sup>, 197 cm<sup>-1</sup>) (Hashem et al. 2018), and NiO (511 cm<sup>-1</sup>, 1051 cm<sup>-1</sup>) (Qiu et al. 2022) oxide phases. Furthermore, the worn surfaces of CoCrNiTiMo<sub>1.5</sub> HEAs after wear testing at 600 °C showed the presence of Co<sub>3</sub>O<sub>4</sub> (194 cm<sup>-1</sup>, 522 cm<sup>-1</sup>, and 692 cm<sup>-1</sup>) (Iliev 2014) and NiTiO<sub>3</sub> (190 cm<sup>-1</sup>, 290 cm<sup>-1</sup>, and 345 cm<sup>-1</sup>). The Raman analysis results align well with the XRD results, presented in section 6.1.4, indicating a consistent correlation between the two analytical methods.

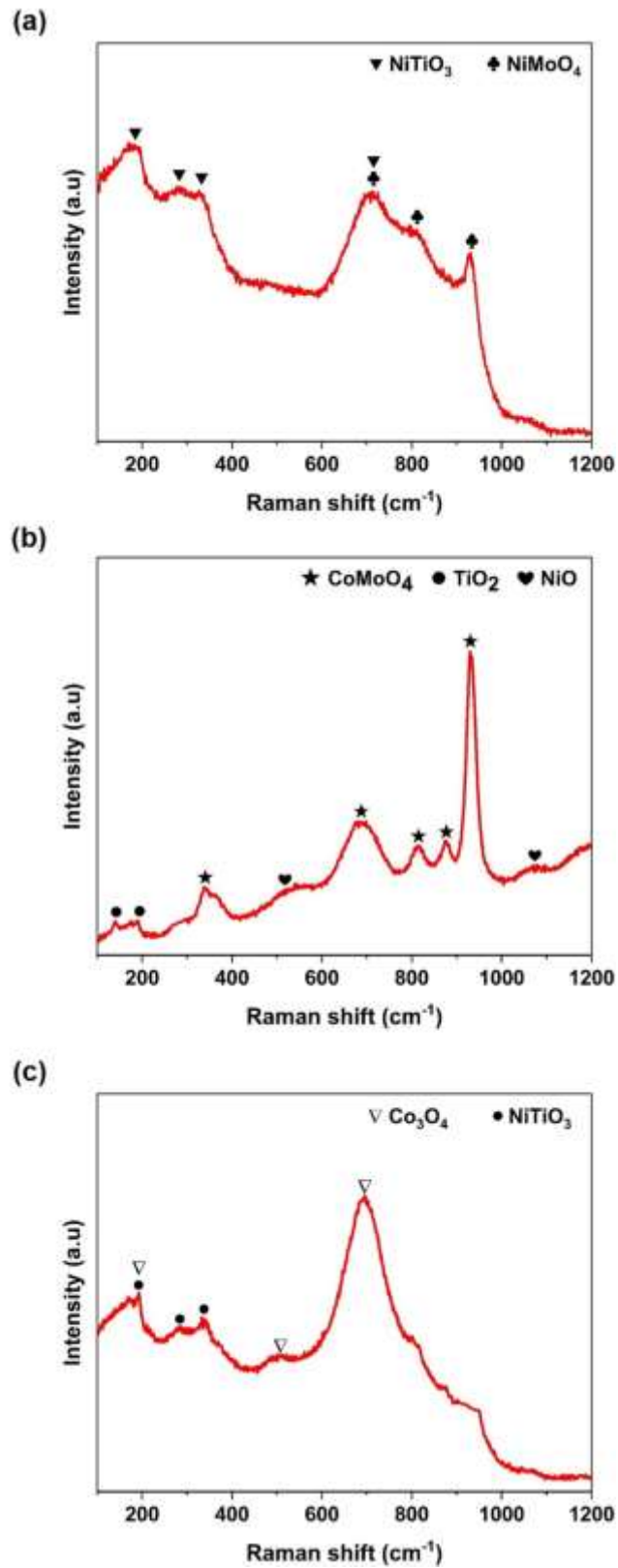


Figure 6.9 Raman spectroscopy of (a) CoCrNiTiMo<sub>0.5</sub> (b) CoCrNiTiMo, and (c) CoCrNiTiMo<sub>1.5</sub> HEA coating's after wear testing at 600 °C.

## 6.2 High Temperature tribological behaviour of CoCrNiTiW<sub>x</sub> HEA Coatings

### 6.2.1 Frictional coefficient plots

The friction coefficient plots of CoCrNiTiW<sub>0.5</sub>, CoCrNiTiW, and CoCrNiTiW<sub>1.5</sub> HEA coatings at different temperatures under dry sliding conditions, with respect to sliding time, can be seen in Figure 6.10. It can be observed that the frictional coefficients continuously increase at the initial stages with respect to time, before reaching a steady state. This state can be referred to as the Run-in state. The sharp increase in the frictional coefficients at the early stages can be attributed to rough surface asperities and high adhesive forces at the beginning (Cheng et al. 2020). As the sliding progresses with time, the surface asperities slowly wear out, and the contact area of the surface increases, thereby leading to steady friction coefficients. It can also be observed from Figure 6.10a that the attainment of a steady state is prolonged for wear tests at high temperatures. The steady-state for CoCrNiTiW<sub>0.5</sub> HEA coating at room temperature was attained early, i.e., around 180 s. However, the steady states for wear tests of 200 °C, 400 °C, and 600 °C were achieved after 550 s, 1320 s and 1500 s, respectively. At high temperatures, the sliding action causes the oxide layer to continuously form and break down, which results in delaying the steady state (Jin et al. 2022; Miao et al. 2021). Due to this, the run-in state is prolonged until a stable oxide layer is formed.

It was observed that CoCrNiTiW HEA coating required comparatively less run-in time to reach a steady state. The run-in times for CoCrNiTiW HEA at RT and 600 °C were found to be 131 s and 820 s, respectively, as depicted in Figure 6.10c. Further, it can be visualized that the run-in times for CoCrNiTiW<sub>1.5</sub> HEA at room temperature and 600 °C were 120 s and 1150 s, respectively (Figure 6.10e). However, a pronounced fluctuation in the steady-state friction coefficients can be seen for CoCrNiTiW<sub>1.5</sub> HEA at room temperature. Similar frictional behaviour has been reported for a few hard BCC HEAs, such as AlCoCrFeNi (Joseph et al. 2019) and AlCoCrCuFeNi (Wu et al. 2006), under dry sliding conditions at room temperature. The fluctuations in friction coefficients at room temperature is mainly attributed to the entrapped debris particles in between the coated surface and counterface, leading to three-body abrasion.

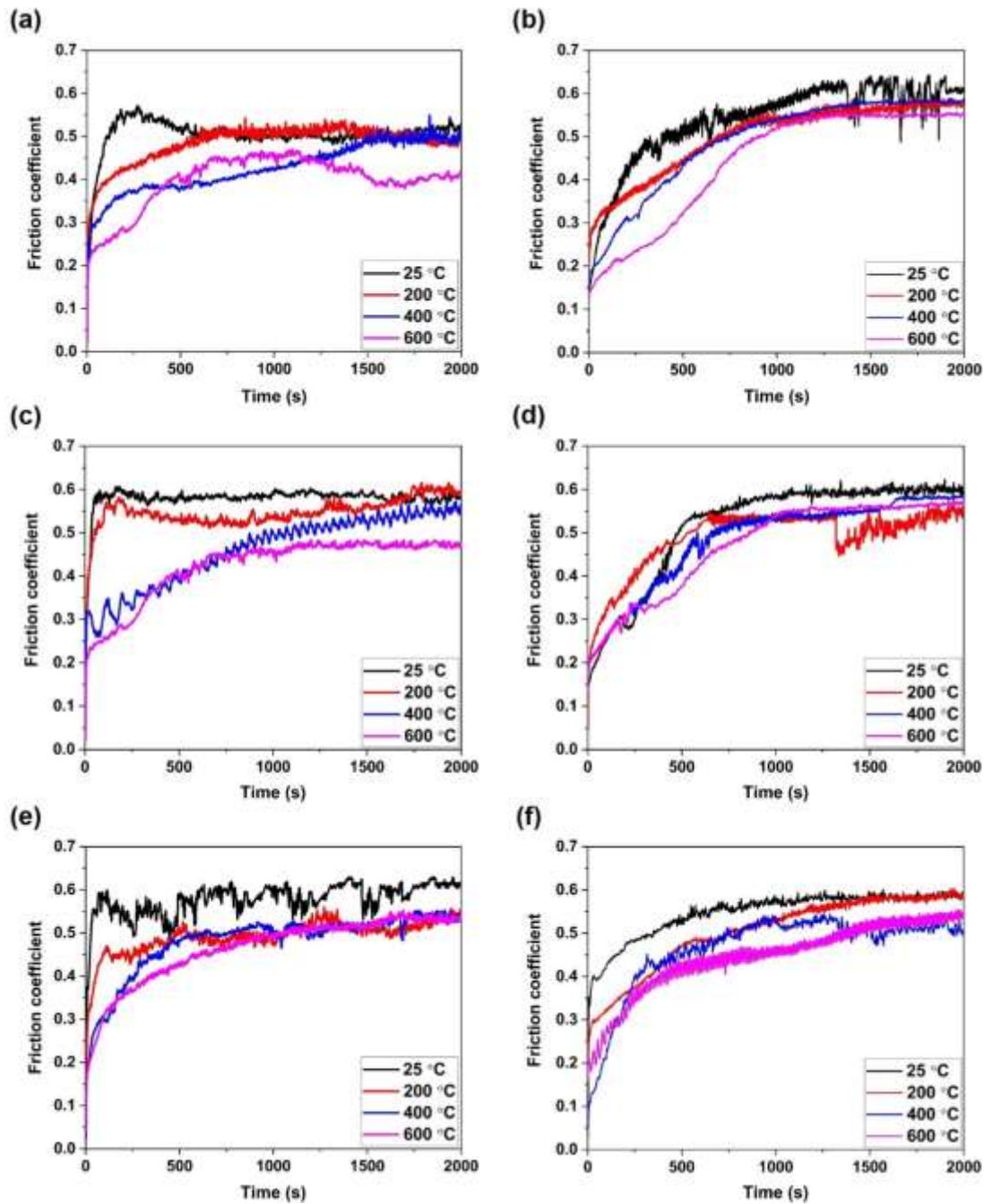


Figure 6.10 Frictional coefficient plots of (a) CoCrNiTiW<sub>0.5</sub>, (c) CoCrNiTiW and (e) CoCrNiTiW<sub>1.5</sub>, at different temperatures under a load of 2 kg. (b), (d), (f) represents the frictional plots of CoCrNiTiW<sub>0.5</sub>, CoCrNiTiW and CoCrNiTiW<sub>1.5</sub> HEA coatings respectively, at a load of 4kg.

Localized fracture of the surface layers also accounts for the fluctuations in frictional coefficients. For instance, the accumulation of wear debris on the worn surface

increases the frictional coefficients, while the breakdown of surfaces reduce the coefficient values. Fluctuations within a range are apparent at room temperature, irrespective of the loading condition. However, at higher normal loads, the increase in the contact area of the sliding pair, enables the trapped debris particles to escape from the contacting surfaces. This leads to a reduction in the three-body abrasive wear and eventually results in lesser fluctuations in the frictional forces. Figure 6.10f shows a smoother curve for CoCrNiTiW<sub>1.5</sub> HEA at a normal load of 4kg, unlike the fluctuations witnessed at a load of 2kg. Nevertheless, minute deviation in the frictional behaviour can be witnessed for CoCrNiTiW<sub>0.5</sub> HEA under room temperature conditions at a load of 4kg (Figure 6.10b). The noticeable fluctuations in the terminal stage of frictional plot is anticipated to the increased accumulation and adhesion of debris particles. Similar variations can also be noticed in the frictional behaviour of CoCrFeNiNb<sub>x</sub> HEA's (Yu et al. 2019b) at room temperatures.

It can also be inferred from Figure 6.10 that the average steady-state frictional coefficients were higher at room temperature. The frictional coefficients of CoCrNiTiW<sub>0.5</sub> HEA dropped from  $0.504 \pm 0.015$  to  $0.397 \pm 0.005$ , with the increment in temperature from RT to 600 °C (Figure 6.10a). Likewise, the frictional coefficients of CoCrNiTiW HEA coatings under normal loading of 2kg decreased from  $0.579 \pm 0.026$  to  $0.422 \pm 0.005$ . Further, the CoCrNiTiW<sub>1.5</sub> HEA exhibited a drop in the frictional coefficients from  $0.578 \pm 0.025$  to  $0.471 \pm 0.004$ . The drop in the frictional coefficients is attributed to the formation of oxide layers at elevated temperatures, which acts as a solid lubricant and reduces the interaction between the coating and counterface (Li et al. 2022; Miao et al. 2021; Pole et al. 2020). Higher frictional coefficients were recorded for CoCrNiTiW<sub>1.5</sub> HEA, when compared to CoCrNiTiW<sub>0.5</sub>, due to the increase in hardness of the HEA with the addition of W. Figure 6.10b,d&f shows the frictional coefficient plots of the HEA's at a normal load of 4kg. The rise in the load results in a slight increment in the average steady-state friction coefficient. The CoCrNiTiW<sub>0.5</sub> HEA reported an increase in the frictional coefficient from  $0.504 \pm 0.015$  to  $0.535 \pm 0.019$  at room temperature. The frictional coefficients of CoCrNiTiW<sub>0.5</sub> and CoCrNiTiW<sub>1.5</sub> HEAs at a normal load of 4kg also follow the decreasing trend with respect to an increase in wear test temperatures.

### 6.2.2 Specific wear rate

Figure 6.11 shows the specific wear rates of CoCrNiTiW<sub>0.5</sub>, CoCrNiTiW, and CoCrNiTiW<sub>1.5</sub> HEA coatings and substrate material at different temperatures and loading conditions. It can be observed from Figure 6.11a that the substrate reported a specific wear rate of  $51.93 \pm 3.7 \times 10^{-6} \text{ mm}^3/\text{N-m}$  at room temperature under a normal load of 2kg. However, the development of HEA coatings resulted in a significant reduction in wear rates. The CoCrNiTiW<sub>0.5</sub>, CoCrNiTiW and CoCrNiTiW<sub>1.5</sub> HEA coatings reported specific wear rates of  $22.7 \pm 2.6 \times 10^{-6} \text{ mm}^3/\text{N-m}$ ,  $15.8 \pm 3.7 \times 10^{-6} \text{ mm}^3/\text{N-m}$ , and  $11.86 \pm 3.5 \times 10^{-6} \text{ mm}^3/\text{N-m}$  respectively, showing a reduction in wear rates by 56.3 %, 69.5% and 77.2 % respectively. The significant drop in the specific wear rates of the deposited coatings is attributed to the emergence of hard BCC solid solution phase and intermetallic phases Co<sub>3</sub>Ti and Cr<sub>7</sub>Ni<sub>3</sub> phases. The effect of W addition results in an increase in the hardness of the HEA and eventually enhances the wear performance. From Figure 6.11, CoCrNiTiW<sub>1.5</sub> HEA demonstrated superior wear resistance compared to other HEA compositions at any given temperature.

With an increase in the temperature from room temperature to 600 °C, the HEA coatings reported a fall in the specific wear rates. The specific wear rate of CoCrNiTiW<sub>0.5</sub> HEA coating dropped by 73.6 % from  $22.7 \pm 2.6 \times 10^{-6} \text{ mm}^3/\text{N-m}$  to  $5.99 \pm 1.9 \times 10^{-6} \text{ mm}^3/\text{N-m}$ , while CoCrNiTiW<sub>1.5</sub> dropped by 78.8% from  $11.86 \pm 3.5 \times 10^{-6} \text{ mm}^3/\text{N-m}$  to  $2.51 \pm 1.5 \times 10^{-6} \text{ mm}^3/\text{N-m}$ . The equimolar CoCrNiTiW HEA coating experienced a 76.3% drop in the wear rates from  $15.8 \pm 3.7 \times 10^{-6} \text{ mm}^3/\text{N-m}$  to  $3.73 \pm 2.1 \times 10^{-6} \text{ mm}^3/\text{N-m}$ . The substantial drop in the wear rates is attributed to the development of a compact oxide layer, which acts as a solid lubricant and limits the interaction of the coated surfaces with the counter face (Chen et al. 2019a; Löbel et al. 2020).

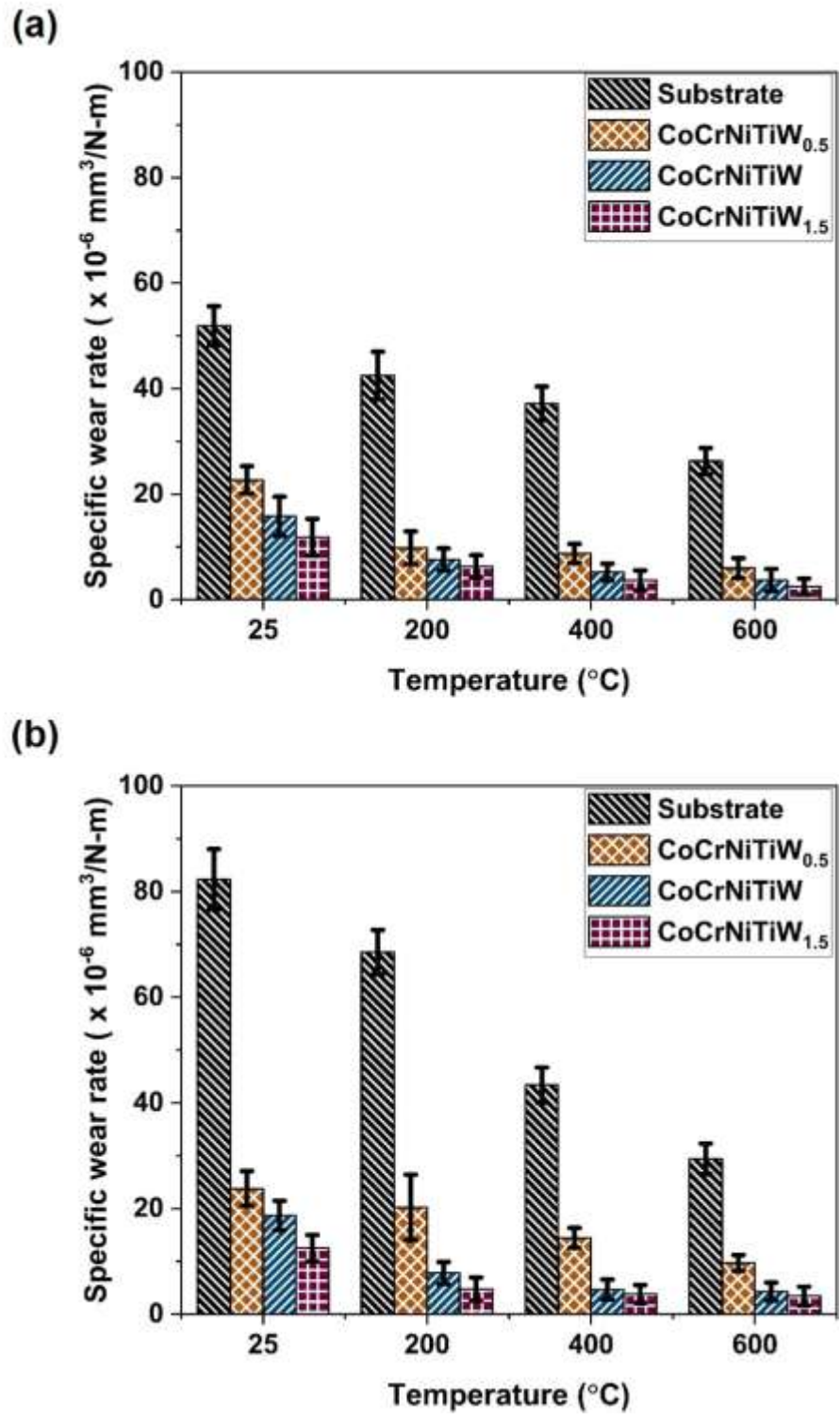


Figure 6.11 Specific wear rates of the substrate and CoCrNiTiW<sub>x</sub> HEA coatings at (a) 2kg load and (b) 4kg load.

The influence of normal load on the wear rate of CoCrNiTiW<sub>x</sub> HEA coatings can also be analysed from Figure 6.11a&b. On rising the load from 2kg to 4kg, the specific wear rates of both the coatings and maraging steel increased reasonably. However, the influence of normal load is significant on the wear rate of substrate, with specific wear rates surging from  $51.93 \pm 3.7 \times 10^{-6} \text{ mm}^3/\text{N-m}$  to  $82.3 \pm 5.6 \times 10^{-6} \text{ mm}^3/\text{N-m}$ . The amount of frictional heat produced at the contact interface plastically deforms the softer material and increases the contact area, resulting in higher wear rates (Medabalimi et al. 2021). Conversely, the CoCrNiTiW<sub>0.5</sub> HEA coating reported a limited increment in the specific wear rate from  $22.7 \pm 2.6 \times 10^{-6} \text{ mm}^3/\text{N-m}$  to  $23.78 \pm 2.5 \times 10^{-6} \text{ mm}^3/\text{N-m}$ . Similarly, the CoCrNiTiW<sub>1.5</sub> HEA coating showed a minimal rise from  $11.86 \pm 3.5 \times 10^{-6} \text{ mm}^3/\text{N-m}$  to  $12.52 \pm 2.5 \times 10^{-6} \text{ mm}^3/\text{N-m}$ . The CoCrNiTiW HEA coating rose from  $15.8 \pm 3.7 \times 10^{-6} \text{ mm}^3/\text{N-m}$  to  $18.71 \pm 2.8 \times 10^{-6} \text{ mm}^3/\text{N-m}$ .

Moreover, the increment in the specific wear rates of CoCrNiTiW<sub>0.5</sub> were more pronounced at 200 °C and 400 °C, with a increment in the load from 2kg to 4kg. This phenomenon can be ascribed to the modest thermal softening on the surface, with an increase in the load and temperature (Löbel et al. 2020). At higher loads, the high contact pressure of the sliding pairs increases the interface temperature, leading to thermal softening on the surface. However, the effect of thermal softening is minimal for CoCrNiTiW and CoCrNiTiW<sub>1.5</sub> HEAs, owing to the presence of higher molar fractions of Tungsten. Tungsten, a refractive metal possessing higher melting point and microhardness significantly enhances the wear performance.

### **6.2.3 Wear mechanisms**

The worn surfaces of CoCrNiTiW<sub>0.5</sub> HEA coatings at various test temperatures have been analysed using the secondary electron mode in SEM and presented in Figure 6.12. Figure 6.12a shows the adhesion of particles detached from the worn surface and alumina counterface. The authors identified the adhesion of debris particles from the surface as localized welding and the adhesion of transferred particles from the alumina counterface as transfer layers. The distinction has been made by identifying the composition of the adhered particles on the worn surface using EDS analysis. The CoCrNiTiW<sub>0.5</sub> micrographs after wear testing at room temperature is characterized by the presence of transfer layers adhered to the worn surface (Figure 6.12a). It has been

observed from the friction coefficient graphs in Figure 6.10 that the frictional forces were comparatively higher at the room temperatures. The continuous contact between the sliding pairs and the absence of lubricant eventually led to the material transfer and adhesion between the sliding surfaces. The plastic deformation and localized welding of the worn debris particles to the surface of the coatings can also be seen. The localized welding of loose debris particles can still be witnessed on the worn surface of CoCrNiTiW<sub>0.5</sub> HEA after wear testing at 200 °C (Figure 6.12b). However, the worn surface was found to be smoother than that at room temperature, with a reduction in the adhesion of transfer layers and size of the debris particles.

The worn surface of CoCrNiTiW<sub>0.5</sub> HEA at 400 °C was found to be smoother, with dark oxide patches scattered over the surface (Figure 6.12c). This resulted in the reduction of loose debris particles on the surface. However, a few cracks and deformation of the surface can also be witnessed, confirming the presence of minor fatigue wear. Fatigue wear is mainly characterized by the poor cohesion of the splats, leading to delamination and pull-out of the weakly bonded splats (Singh et al. 2019). Abrasive grooves can also be seen widely on the worn surface, owing to the smooth oxide patches. Therefore the wear at 400 °C is due to the combination of oxidative, fatigue and abrasive wear mechanisms. The amount of Al transferred from the counter surface was greatly decreased.

The worn surface at 600 °C was characterized by the presence of a continuous oxide layer (Figure 6.12d). The surface has become smoother, with a reduction in the size and quantity of the debris particles. The formation of a continuous oxide layer acted as a solid lubricant and reduced the direct contact between the coated surface and the Al<sub>2</sub>O<sub>3</sub> counter disc, resulting in the drop of frictional coefficients and specific wear rates, as mentioned in Figure 6.10 & Figure 6.11. Further, oxide tribofilms suppresses the adhesion between the friction pairs and results in the reduction of surface roughness (Cheng et al. 2020). Ploughing grooves can also be occasionally seen at specific sites. A significant decrease in the delaminated regions on the surface eventually led to a drop in the worn debris particles scattered on the surface. The peeled-off oxide debris accumulates and sinter on the worn surface of the coatings after repeated cycles, eventually forming oxide tribofilms (Li et al. 2022). The EDS analysis on the dark

region (point 7) showed the presence of significant contributions from Ti, Ni, Cr and O<sub>2</sub>. Therefore, the wear mechanism at 600°C, is dominated significantly by oxidative wear.

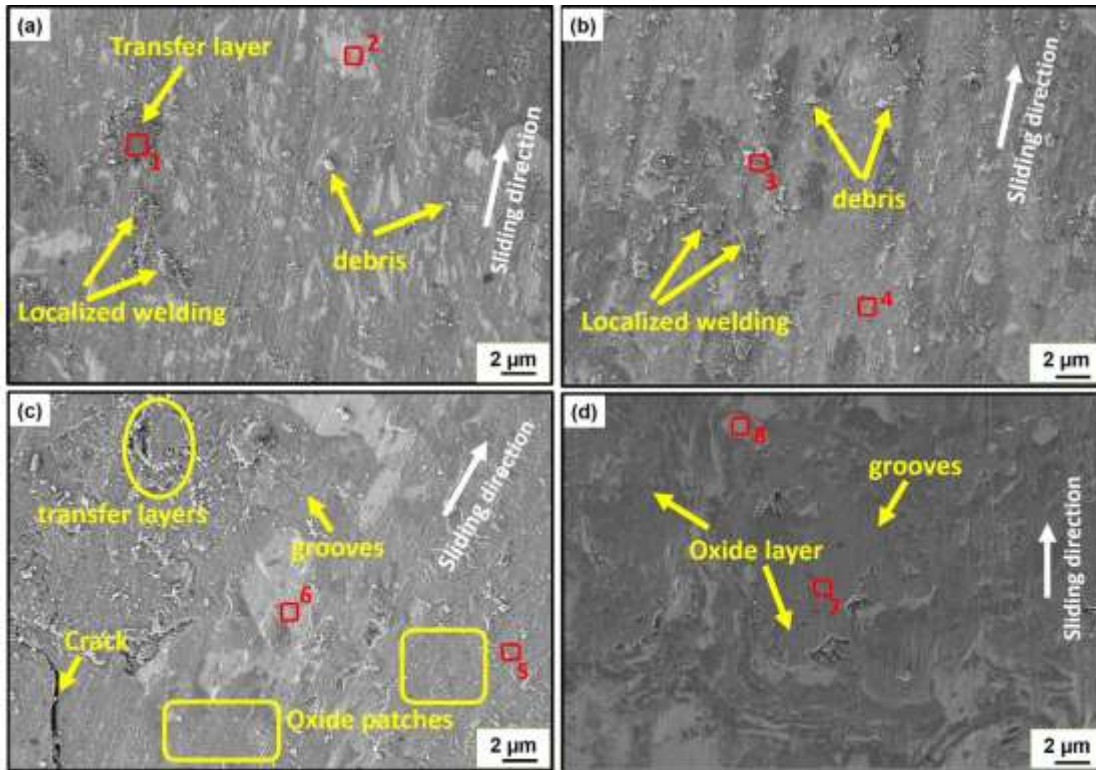


Figure 6.12 SEM images showing the wear mechanisms of CoCrNiTiW<sub>0.5</sub> HEA worn surfaces at a) RT b) 200 °C c) 400 °C d) 600 °C in Secondary electron imaging mode.

Table 6.4 EDS analysis of specified points in Figure 6.12 showing the chemical compositions in at%.

Sliding temperature	Point	Chemical composition (at %)						
		Co	Cr	Ni	Ti	W	O	Al
RT	1	13.69	11.90	12.86	11.13	6.28	32.72	11.41
	2	24.14	20.39	16.40	21.61	5.46	11.57	0.43
200°C	3	10.65	8.33	10.52	9.90	7.51	39.15	13.94
	4	20.58	21.23	18.81	14.24	10.03	12.6	0.51
400°C	5	12.19	10.76	11.33	9.54	4.49	46.89	4.81
	6	17.38	19.77	15.76	18.64	6.04	21.01	1.40
600°C	7	1.23	9.86	5.33	17.53	1.62	63.17	1.25
	8	25.36	18.77	25.08	2.05	10.09	18.19	0.45

The worn surfaces of CoCrNiTiW coatings can be analyzed from Figure 6.13. It's noticeable from the SEM micrographs that many flattened debris particles were seen to be adhered to the surface of the sample at room temperature conditions, corroborating the adhesive wear mechanism. At 200 °C, the worn surface displays minor cracks, shallow pits, and adhered particles. The EDS analysis also supports the adhesive wear mechanisms, owing to the increased presence of Aluminum transferred from the counter face. Oxides can also be revealed on the worn surfaces at 200 °C; however, the observed oxides possess a rough surface.

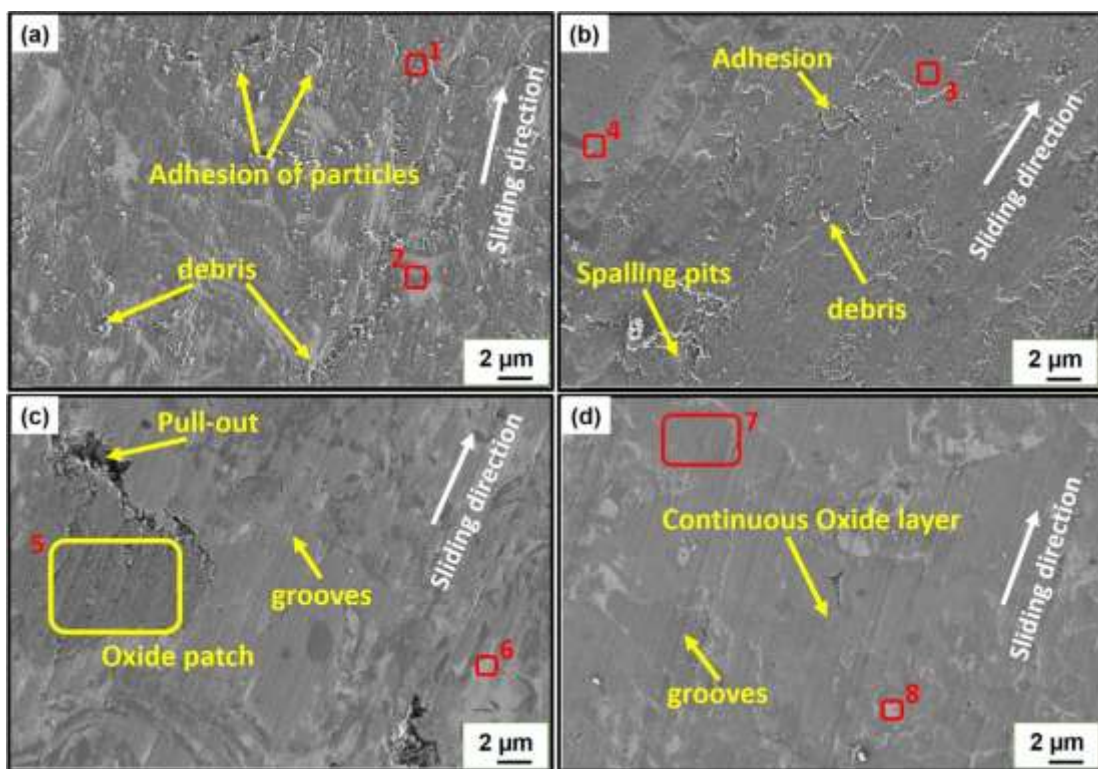


Figure 6.13 SEM images showing the wear mechanisms of CoCrNiTiW HEA worn surfaces at a) RT b) 200°C c) 400°C d) 600°C in Secondary electron imaging mode.

At 400 °C, the worn surface reveals the presence of discontinuous oxide patches spread over the surface. The EDS analysis also highlights the increased presence of O<sub>2</sub> and a reduction in the Al content. The oxide patches were enriched with Cr and oxide content, confirming the presence of corresponding metal oxides. Additionally, shallow grooves and a few pull-out sites can be witnessed, substantiating the presence of abrasive and fatigue wear mechanisms. At 600 °C, the worn surface exhibits a smoother surface

characterized by a continuous oxide film. The EDS analysis emphasizes increased oxygen content on the worn surface, signifying oxidative wear.

Table 6.5 EDS analysis of specified points in Figure 6.13 showing the chemical compositions in at%.

Sliding temperature	Point	Chemical composition (at %)						
		Co	Cr	Ni	Ti	W	O	Al
RT	1	12.12	10.8	11.20	11.99	8.90	32.38	12.62
	2	16.51	20.67	15.05	25.06	11.42	10.69	0.59
200°C	3	10.02	10.66	9.78	13.15	7.95	37.45	10.99
	4	24.82	12.09	21.30	9.38	17.70	14.17	0.55
400°C	5	3.74	28.91	1.94	14.54	5.53	44.83	0.51
	6	15.47	5.33	25.85	3.11	27.93	22.20	0.12
600°C	7	10.64	13.05	2.90	24.27	1.42	47.63	0.09
	8	19.54	5.19	17.86	2.75	6.30	48.33	0.02

On the other hand, for CoCrNiTiW<sub>1.5</sub> HEA coatings, the transfer layers adhered to the worn surface increased in number and size after wear testing at RT, as can be seen in Figure 6.14a. Few shallow pits and loose debris particles can also be located on the surface, confirming the presence of dominant adhesive wear mechanism. The EDS analysis on the adhered particles (points 1&3) reveals significant contributions from Al and O<sub>2</sub>, highlighting the presence of Al<sub>2</sub>O<sub>3</sub> adhered from the counter face. Table 6.6 presents the EDS analysis results for all the labelled points in Figure 6.14.

For wear tests conducted at 200 °C, minor cracks with shallow pits can be seen on the worn surface of CoCrNiTiW<sub>1.5</sub> HEA. The coating material experiences pull-outs at the corners, which confirms that the wear mechanism is due to fatigue. The worn surface contains innumerable debris particles, indicating the fragments of the delaminated coatings (Mahade et al. 2022). The dark patches representing the formation of oxides exhibited a rough surface. Oxides formed on surfaces at lesser wear test temperatures usually have a rough surface. Furthermore, the surface is only partially covered with oxides, as confirmed from the EDS data (Löbel et al. 2020).

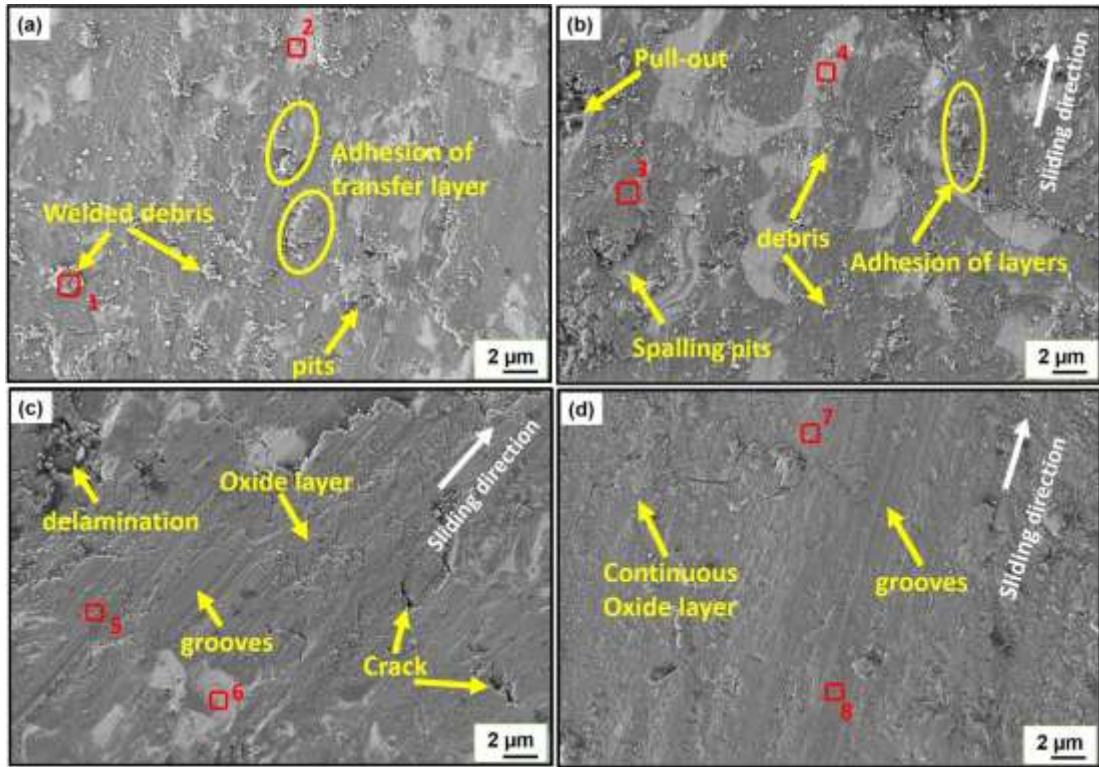


Figure 6.14 SEM images showing the wear mechanisms of CoCrNiTiW<sub>1.5</sub> HEA worn surfaces at a) RT b) 200°C c) 400°C d) 600°C in Secondary electron imaging mode.

Table 6.6 EDS analysis of specified points in Figure 6.14 showing the chemical compositions in at%.

Sliding temperature	Point	Chemical composition (at %)						
		Co	Cr	Ni	Ti	W	O	Al
RT	1	11.02	12.02	10.27	12.13	7.78	36.49	10.29
	2	14.50	20.40	15.08	17.09	16.28	15.23	1.42
200°C	3	9.75	7.10	9.80	8.75	6.46	45.20	12.94
	4	18.58	19.23	17.81	7.24	20.03	15.6	1.51
400°C	5	9.55	8.34	7.59	8.31	7.70	52.9	5.5
	6	28.86	1.84	20.67	1.45	26.09	18.98	2.1
600°C	7	6.40	6.76	5.10	2.47	8.37	66.95	3.94
	8	12.82	12.10	8.95	20.5	13.21	31.21	1.21

The worn morphology of the CoCrNiTiW<sub>1.5</sub> HEA at 400 °C exhibited pronounced dark oxide patches spread over the entire worn surface (Figure 6.14c). Ploughing grooves can also be seen in the sliding direction, confirming the presence of abrasive wear. The EDS analysis on the dark region (point 5) confirms the presence of oxide scales.

Further, the worn surface at 600 °C depicts a continuous oxide layer spread across the entire surface, confirming the oxidative wear mechanism.

It can be inferred from Fig. 6.12 & Fig. 6.14, that even though the mechanisms contributing to the wear rates of all the HEA's were similar, a noticeable distinction can be observed in terms of intensity of the observed mechanisms. For example, Figure 6.14a demonstrates the presence of multiple adhered particles on the surface, as opposed to Figure 6.12a, highlighting the intensity of adhesive wear. Similarly, at the test temperature of 600 °C, the surface of CoCrNiTiW<sub>1.5</sub> HEA exhibits a pronounced oxide layer, as compared to the oxide patches on CoCrNiTiW<sub>0.5</sub> HEA. The higher wear resistance of CoCrNiTiW<sub>1.5</sub> HEA can be attributed to the increment in W molar fraction. As reported in table 3.2, there is a significant variation in the atomic percentages of W in CoCrNiTiW<sub>0.5</sub> (11.12%), CoCrNiTiW (20%), and CoCrNiTiW<sub>1.5</sub> (27.28%). Tungsten is a refractive metal possessing high density and microhardness. The increment in the molar fraction of W, accounted for a rise in density from 7.93 g/cm<sup>3</sup> (CoCrNiTiW<sub>0.5</sub>) to 10.17 g/cm<sup>3</sup> (CoCrNiTiW<sub>1.5</sub>). The microhardness values also reported a significant increment by 18.77% from 863 HV<sub>0.3</sub> to 1025 HV<sub>0.3</sub>, with a rise in the W molar fraction from 0.5 to 1.5.

#### **6.2.4 X-Ray diffraction**

In order to understand the wear characteristics of CoCrNiTiW<sub>0.5</sub>, CoCrNiTiW and CoCrNiTiW<sub>1.5</sub> HEAs at different temperatures and identify the formation of phases, X-ray diffraction studies have been performed on the worn surfaces of the HEA coatings. Figure 6.15 clearly depicts the distinct phases that have emerged in the CoCrNiTiW<sub>0.5</sub> HEAs under different wear test temperatures. It is evident that the Cr<sub>2</sub>O<sub>3</sub>, BCC and Co<sub>3</sub>Ti phases that were formed during the coating development stage have remained intact even after the wear test conducted at room temperature. No further changes were observed during the wear test conducted at room temperature. Similarly, the wear test conducted at a temperature of 200 °C does not indicate the existence of any new phases. However, the peaks have become sharper, indicating an increase in the crystallite size with temperature.

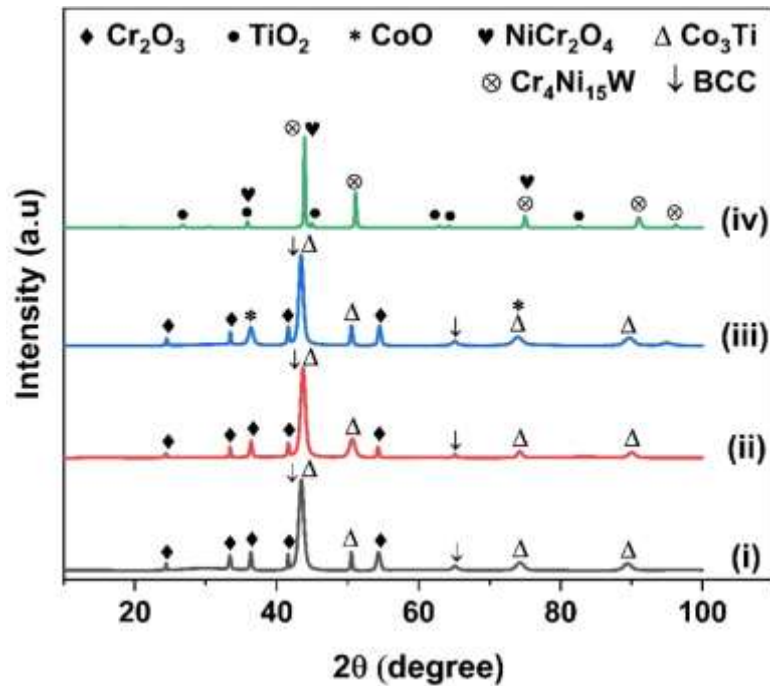


Figure 6.15 X-ray diffraction of worn surfaces of CoCrNiTiW<sub>0.5</sub> HEA coatings after wear testing at (i) RT, (ii) 200 °C, (iii) 400 °C, and (iv) 600 °C.

Moreover, the intensity of oxide peaks is enhanced at higher test temperatures. As the test temperature increases to 400 °C, the Cr<sub>2</sub>O<sub>3</sub> peaks intensify, and an additional CoO phase can be seen. On further increasing the wear temperature to 600 °C, new oxide peaks such as TiO<sub>2</sub> (PDF# 01-076-0319), NiCr<sub>2</sub>O<sub>4</sub> spinel (PDF# 01-075-0198), and a hard Cr<sub>4</sub>Ni<sub>15</sub>W intermetallic (PDF# 03-065-5108) can be observed. The formation of additional oxide phases at elevated temperatures improves the tribological performance of the alloy.

The CoCrNiTiW HEA coatings demonstrated the presence of two BCC solid solutions and NiTiO<sub>3</sub> spinel at room temperature (Figure 6.16). The phases observed at room temperature have been retained at 200 °C. However, the wear test at 400 °C unveiled the disappearance of NiTiO<sub>3</sub> spinel, resulting in the formation of a new oxide phase, CrWO<sub>3</sub> (PDF# 01-074-1694). Subsequently, the elevated temperature wear test performed at 600 °C reported the formation of an intermetallic NiW (PDF# 00-047-1172), BCC phase (PDF# 00-004-0806), CoWO<sub>4</sub> (PDF# 01-072-0479), WO<sub>3</sub> (PDF# 01-088-0550), and TiO<sub>2</sub> (PDF# 01-076-0319) oxides.

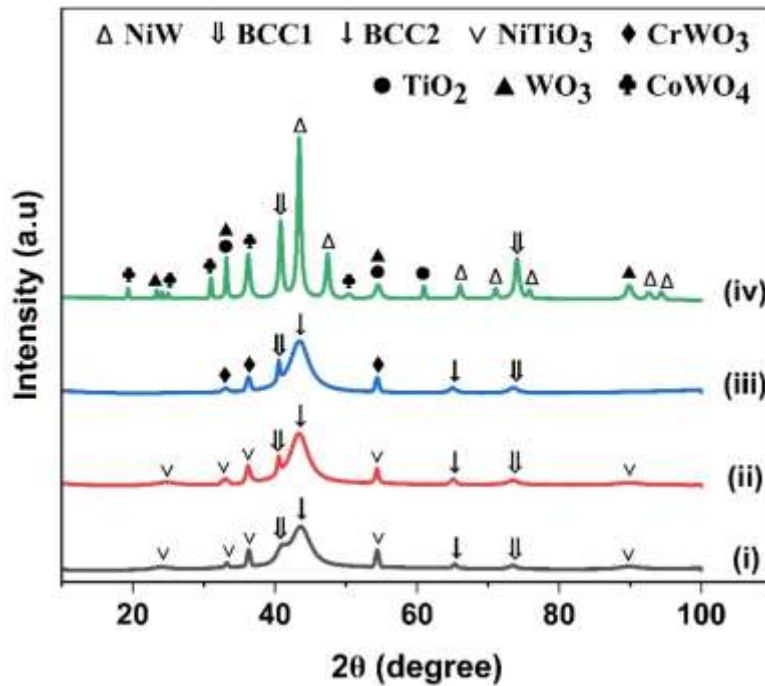


Figure 6.16 X-ray diffraction of worn surfaces of CoCrNiTiW HEA coatings after wear testing at (i) RT, (ii) 200 °C, (iii) 400 °C, and (iv) 600 °C.

Additionally, the CoCrNiTiW<sub>1.5</sub> HEA maintained the formation of NiTiO<sub>3</sub>, BCC, and Cr<sub>7</sub>Ni<sub>3</sub> phases from the coating process, even after undergoing wear testing at room temperature (Figure 6.17). At a testing temperature of 200 °C, the Cr<sub>7</sub>Ni<sub>3</sub> phase underwent a transformation to form Cr<sub>2</sub>Ti phase. The CoO phase formed during the wear testing of CoCrNiTiW<sub>0.5</sub> at 400 °C can also be witnessed in the case of CoCrNiTiW<sub>1.5</sub>. The broadening of the peak observed in the wear test at 400 °C typically indicates changes in the microstructure or properties of the coating due to the elevated temperature. Elevated temperatures can cause phase transformations in the coating material, leading to changes in hardness and toughness. The broadening of the peak may indicate the presence of multiple phases or the formation of new phases with different properties. Further, the broadening of peaks can also indicate a reduction in the crystallite size and increment in the micro strain within the coating. High micro strain can make the coating more prone to crack formation under wear conditions. In Fig. 6.17, it is observed that that the wear test at 400 °C, reveals the presence of 3 different phases between 40 – 45 °C, and the obvious peak broadening is attributed to

the presence of these phases. The presence of additional oxide phase at elevated temperature has a positive influence on the wear performance.

The wear test conducted at 600 °C revealed the presence of a hard  $\text{Ni}_{17}\text{W}_3$  phase (PDF# 03-065-4828), along with several oxide phases, including  $\text{WO}_3$  (PDF# 01-088-0550),  $\text{NiWO}_4$  (PDF# 01-072-1189), and  $\text{CoCr}_2\text{O}_4$  (PDF# 01-078-0711). The presence of higher molar fractions of W in  $\text{CoCrNiTiW}_{1.5}$  enabled the formation of dense oxides enriched with tungsten, which eventually resulted in improved wear resistance.

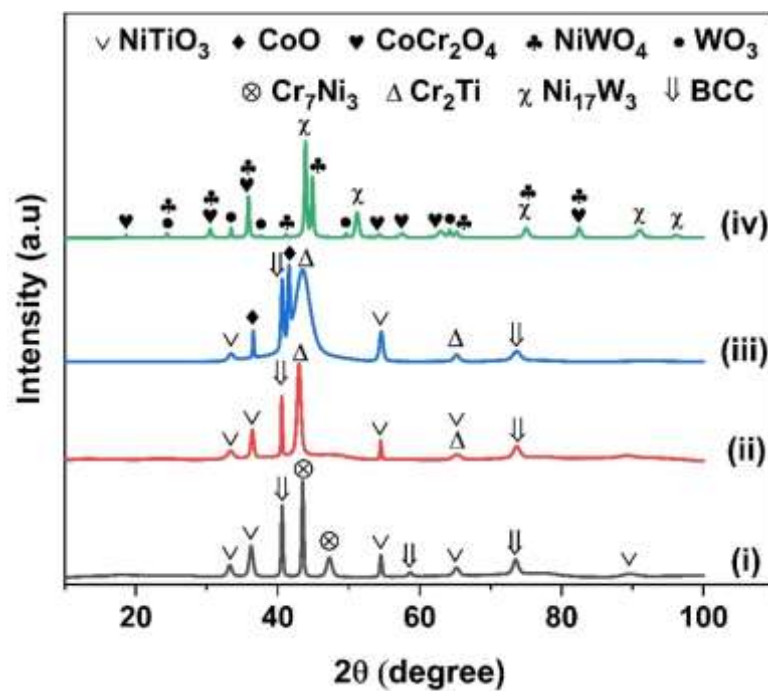


Figure 6.17 X-ray diffraction of worn surfaces of  $\text{CoCrNiTiW}_{1.5}$  HEA coatings after wear testing at (i) RT, (ii) 200 °C, (iii) 400 °C, and (iv) 600 °C.

### 6.2.5 Raman Spectroscopy

Raman spectroscopy is an effective tool to characterize the worn surfaces and identify the formed oxide phases (Chen et al. 2019a; Guo et al. 2019; Miao et al. 2021). Therefore to substantiate the formation of oxide phases, Raman spectroscopy is performed on the surfaces of  $\text{CoCrNiTiW}_{0.5}$ ,  $\text{CoCrNiTiW}$  and  $\text{CoCrNiTiW}_{1.5}$  HEA coatings after wear testing at 600 °C (Figure 6.18). Raman spectroscopy reported the presence of  $\text{TiO}_2$  ( $399\text{ cm}^{-1}$ ,  $511\text{ cm}^{-1}$ ) (Hashem et al. 2018) and  $\text{NiCr}_2\text{O}_4$  ( $181\text{ cm}^{-1}$ ,  $511\text{ cm}^{-1}$ , and  $686\text{ cm}^{-1}$ ) (Wang et al. 2003) on the worn surfaces of  $\text{CoCrNiTiW}_{0.5}$  coatings.

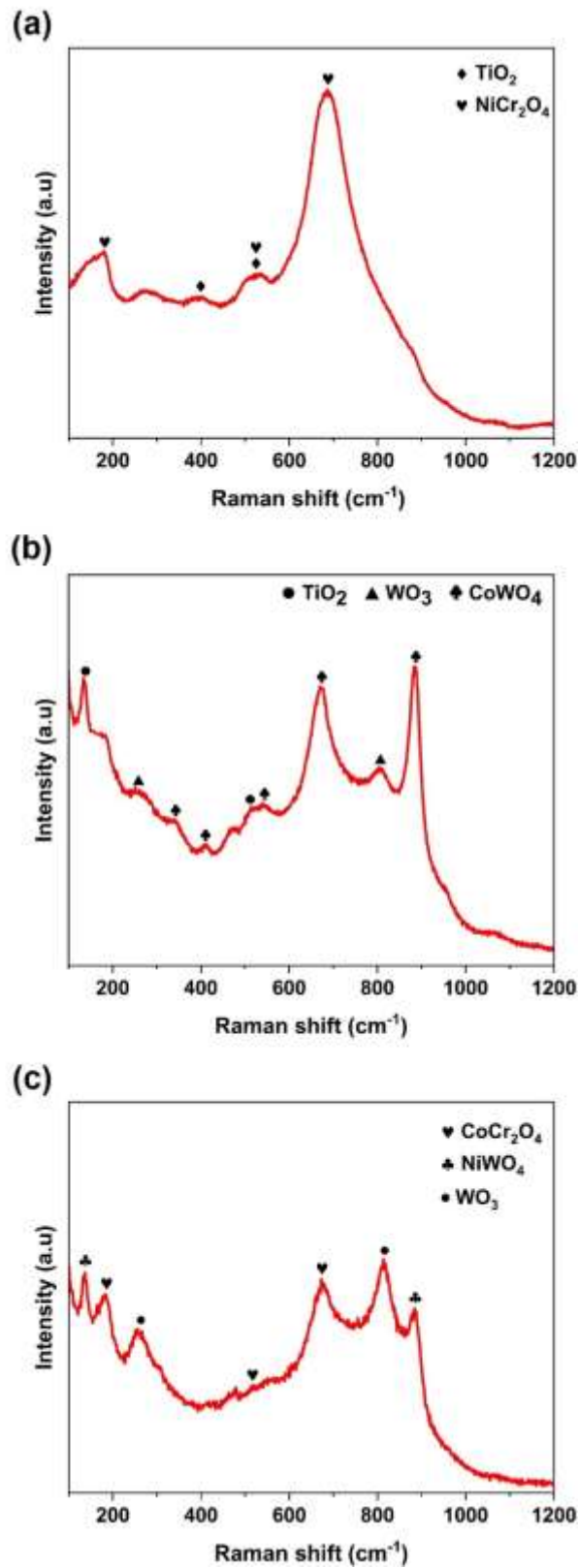


Figure 6.18 Raman spectroscopy of (a) CoCrNiTiW<sub>0.5</sub> (b) CoCrNiTiW, and (c) CoCrNiTiW<sub>1.5</sub> HEA coating's after wear testing at 600 °C.

Similarly, the worn surfaces of CoCrNiTiW HEA after wear testing at 600 °C showed the presence of CoWO<sub>4</sub> (340 cm<sup>-1</sup>, 408 cm<sup>-1</sup>, 536 cm<sup>-1</sup>, 686 cm<sup>-1</sup> and 881 cm<sup>-1</sup>) (Alharthi et al. 2021), WO<sub>3</sub> (256 cm<sup>-1</sup>, 801 cm<sup>-1</sup>) (Díaz-Reyes et al. 2013), and TiO<sub>2</sub> (144 cm<sup>-1</sup>, 513 cm<sup>-1</sup>) (Hashem et al. 2018) oxides. Further, the CoCrNiTiW<sub>1.5</sub> HEA revealed the presence of CoCr<sub>2</sub>O<sub>4</sub> (192 cm<sup>-1</sup>, 520 cm<sup>-1</sup>, 680 cm<sup>-1</sup>) (Sethi et al. 2017), NiWO<sub>4</sub> (140 cm<sup>-1</sup>, 891 cm<sup>-1</sup>) (Lima et al. 2020), and WO<sub>3</sub> (256 cm<sup>-1</sup>, 801 cm<sup>-1</sup>) phases (Díaz-Reyes et al. 2013). The observed Raman spectroscopy findings were in good agreement with the XRD phases reported in section 6.2.4. The presence of different oxide phases on the worn surfaces at 600 °C, as identified in Figure 6.18, led to the drop in frictional coefficients and specific wear rates (Jin et al. 2022; Nguyen et al. 2022).

### **6.3 Wear mechanisms of substrate**

The worn surface morphologies of maraging steel substrate at different temperatures were presented in Figure 6.19. It is evident that the worn surfaces were characterized by the presence of grooves and debris particles, irrespective of the test temperatures, demonstrating the dominant abrasive wear mechanism. Abrasion of the relatively softer maraging steel is apparent when sliding against the hard alumina counterface and the ploughed particles were seen to be scattered all over the surface as debris particles. The abrasive grooves were clear and well aligned in the sliding direction. Further at a test temperature of 600 °C, along with the abrasive grooves minor oxide patches can be observed on the worn surface.

The specific wear rates of the substrate is substantially higher, when compared to the wear rates of HEA coatings. The substrate reported a wear rate of  $51.93 \pm 3.7 \times 10^{-6}$  mm<sup>3</sup>/N-m at room temperature under a normal load of 2kg. While the CoCrNiTiMo and CoCrNiTiW HEA coatings exhibited specific wear rates of  $17.34 \pm 2.8 \times 10^{-6}$  mm<sup>3</sup>/N-m and  $15.8 \pm 3.7 \times 10^{-6}$  mm<sup>3</sup>/N-m, resulting in a reduction of 66.6% and 69.5% respectively. The specific wear rates of the substrate at different temperatures and loads can be visualized from Figure 6.11.

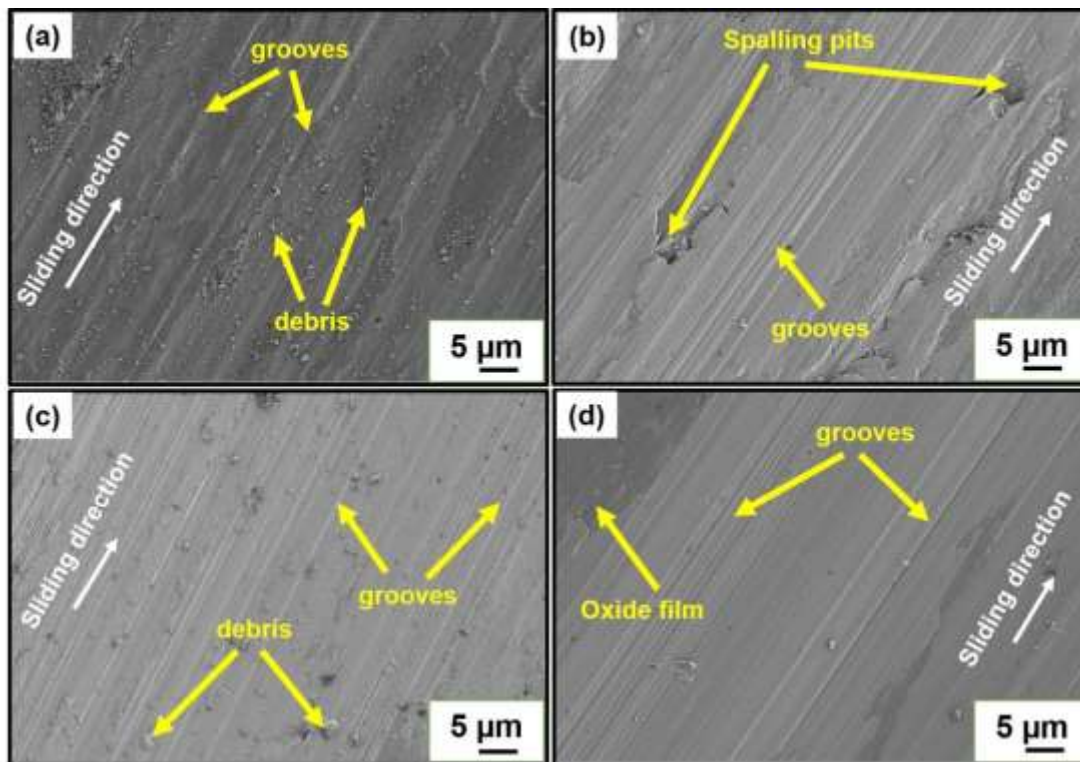


Figure 6.19 SEM images showing the wear mechanisms of maraging steel substrate after wear testing at (a) RT, (b) 200 °C (c) 400 °C, and (d) 600 °C.

#### 6.4 Summary

The tribological performance of  $\text{CoCrNiTiMo}_x$  and  $\text{CoCrNiTiW}_x$  HEA coatings at different temperatures and loading conditions is extensively investigated and compared with that of the uncoated substrate. The HEA coatings exhibited higher wear resistance at any given temperature, when compared to the substrate. Further, the deposited  $\text{CoCrNiTiMo}_x$  and  $\text{CoCrNiTiW}_x$  HEA coatings exhibited a substantial reduction in the wear rates as the wear test temperature rose from RT to 600°C. The  $\text{CoCrNiTiMo}$  HEA coating's specific wear rate dropped by 70.5%, from  $17.34 \pm 2.8 \times 10^{-6} \text{ mm}^3/\text{N}\cdot\text{m}$  to  $5.1 \pm 1.6 \times 10^{-6} \text{ mm}^3/\text{N}\cdot\text{m}$ . Likewise, the  $\text{CoCrNiTiW}$  coating experienced a 76.3% drop in the wear rates from  $15.8 \pm 3.7 \times 10^{-6} \text{ mm}^3/\text{N}\cdot\text{m}$  to  $3.73 \pm 2.1 \times 10^{-6} \text{ mm}^3/\text{N}\cdot\text{m}$ .

Further, the frictional coefficients of  $\text{CoCrNiTiMo}$  and  $\text{CoCrNiTiW}$  HEA coatings reduced from  $0.529 \pm 0.014$  to  $0.451 \pm 0.006$  and  $0.579 \pm 0.026$  to  $0.422 \pm 0.005$  respectively, with an increment in the wear testing temperature from RT to 600 °C. The decrement in the COF values at elevated temperatures was accredited to the development of oxide tribofilms. Specifically, the  $\text{CoCrNiTiMo}$  exhibited the

development of  $\text{CoMoO}_4$ ,  $\text{TiO}_2$ , and  $\text{NiO}$ , while the  $\text{CoCrNiTiW}$  coating displayed the emergence of  $\text{WO}_3$ ,  $\text{CoWO}_4$ , and  $\text{TiO}_2$  at  $600\text{ }^\circ\text{C}$ . Similar decreasing trend in the frictional and wear behaviour has been witnessed in the case of other non-equiatomic HEA compositions including  $\text{CoCrNiTiMo}_{0.5}$ ,  $\text{CoCrNiTiMo}_{1.5}$ ,  $\text{CoCrNiTiW}_{0.5}$ , and  $\text{CoCrNiTiW}_{1.5}$  HEAs. The effect of variation in the molar fractions of Molybdenum and Tungsten on the tribological performance, phase formation and wear mechanisms of the HEA coatings is extensively investigated in the current chapter. The results indicate a clear distinction in the performance of  $\text{CoCrNiTiW}_{0.5}$ ,  $\text{CoCrNiTiW}$  and  $\text{CoCrNiTiW}_{1.5}$  HEA coatings. The increase in the molar fraction of Mo and W leads to a significant increment in the hardness and wear resistance of the HEAs under investigation.



## CHAPTER 7

### CONCLUSIONS AND FUTURE WORK

#### 7.1 Conclusions

In the present study, CoCrNiTiMo<sub>x</sub> (x=0.5,1,1.5) and CoCrNiTiW<sub>x</sub> (x=0.5,1,1.5) HEA coatings were deposited on maraging steel using HVOF technique. The deposited coatings were characterized with respect to their microstructural and mechanical performance. The tribological behavior of the HEA coatings were extensively investigated at different temperatures and the following conclusions were arrived.

- CoCrNiTiMo<sub>x</sub> (x=0.5,1,1.5) and CoCrNiTiW<sub>x</sub> (x=0.5,1,1.5) HEAs were processed by ball milling the constituent metal powders, resulting in the formation of 2 BCC solid solutions. The effect of ball milling time and speed on the alloying rate was studied in detail by varying the milling times and speed. After thorough characterization, the powders milled for 10 h was used as the feedstock for thermal spray deposition, owing to the morphology and particle size of the powders.
- The deposited HEA coatings retained the BCC solid solution phases formed during the milling stage. However, additional oxide including NiTiO<sub>3</sub> spinel, Cr<sub>2</sub>O<sub>3</sub> and TiO<sub>2</sub> and intermetallic phases including MoNi, Co<sub>2</sub>Mo<sub>3</sub>, Co<sub>3</sub>Ti, Cr<sub>7</sub>Ni<sub>3</sub> were formed owing to the high temperatures and velocities experienced during the HVOF spray deposition.
- The microstructural analysis of the HEA coatings unveiled a compact lamellar structure characterized by robust mechanical bonding to the substrate. The porosities of CoCrNiTiMo<sub>0.5</sub>, CoCrNiTiMo, and CoCrNiTiMo<sub>1.5</sub> HEA coatings were found to be  $1.1 \pm 0.3\%$ ,  $1.12 \pm 0.05 \%$ , and  $1.32 \pm 0.2\%$  respectively. While the porosities of CoCrNiTiW<sub>0.5</sub>, CoCrNiTiW, and CoCrNiTiW<sub>1.5</sub> HEA coatings were found to be  $1.31 \pm 0.32 \%$ ,  $1.19 \pm 0.03 \%$  and  $1.25 \pm 0.37 \%$  respectively.
- The mechanical performance of the deposited HEA coatings revealed superior values, when compared to other conventional coatings. The microhardness of

CoCrNiTiMo<sub>0.5</sub>, CoCrNiTiMo, and CoCrNiTiMo<sub>1.5</sub> HEA coatings were found to be 841±62 HV<sub>0.3</sub>, 927 ± 45 HV<sub>0.3</sub> and 952±23 HV<sub>0.3</sub>, respectively. On the other hand, the microhardness of CoCrNiTiW<sub>0.5</sub>, CoCrNiTiW, and CoCrNiTiW<sub>1.5</sub> HEA coatings were found to be 863±52 HV<sub>0.3</sub>, 951 ± 38 HV<sub>0.3</sub> and 1025±39 HV<sub>0.3</sub>, respectively. Further, it can be witnessed that the as-sprayed HEA coatings exhibited a steady increment in the microhardness values with an increment in the molar fraction of Mo and W.

- The fracture toughness of CoCrNiTiMo<sub>0.5</sub>, CoCrNiTiMo, and CoCrNiTiMo<sub>1.5</sub> HEA coatings, as determined by using Evans and Wilshaw's equation, were found to be 2.89 ± 0.31 (Mpa m<sup>1/2</sup>), 3.26 ± 0.25 (Mpa m<sup>1/2</sup>) and 3.79 ± 0.35 (Mpa m<sup>1/2</sup>) respectively. Likewise, the fracture toughness of CoCrNiTiW<sub>0.5</sub>, CoCrNiTiW, and CoCrNiTiW<sub>1.5</sub> HEA coatings, were found to be 3.22 ± 0.26 (Mpa m<sup>1/2</sup>), 3.54 ± 0.32 (Mpa m<sup>1/2</sup>) and 3.87 ± 0.3 (Mpa m<sup>1/2</sup>) respectively.
- The frictional coefficients of CoCrNiTiMo HEA coatings dropped from 0.529 ± 0.014 to 0.451 ± 0.006, while CoCrNiTiW HEA dropped from 0.579 ± 0.026 to 0.422 ± 0.005, with a rise in temperature from RT to 600 °C. Similar drop in the frictional coefficients is witnessed for other non-equimolar compositions including CoCrNiTiMo<sub>0.5</sub>, CoCrNiTiMo<sub>1.5</sub>, CoCrNiTiW<sub>0.5</sub>, and CoCrNiTiW<sub>1.5</sub> HEA coatings
- Likewise, the specific wear rate of CoCrNiTiMo HEA coating dropped by 70.5%, declining from 17.34 ± 2.8 x10<sup>-6</sup> mm<sup>3</sup>/N-m to 5.1 ± 1.6 x10<sup>-6</sup> mm<sup>3</sup>/N-m, while CoCrNiTiW dropped by 76.3%, decreasing from 15.8 ± 3.7 x10<sup>-6</sup> mm<sup>3</sup>/N-m to 3.73 ± 2.1 x10<sup>-6</sup> mm<sup>3</sup>/N-m, with an increase in the temperature from RT to 600 °C.
- The decrement in the friction coefficients and specific wear rates of as-sprayed HEA coatings at elevated temperatures was accredited to the development of oxide tribofilms. Specifically, the CoCrNiTiMo exhibited the development of CoMoO<sub>4</sub>, TiO<sub>2</sub>, and NiO, while the CoCrNiTiW coating displayed the emergence of WO<sub>3</sub>, CoWO<sub>4</sub>, and TiO<sub>2</sub> at 600 °C.

- The as-sprayed HEA coating's wear mechanisms transformed from a dominant abrasive and adhesive wear at room temperature to significant oxidative wear with minor fatigue at a temperature of 600°C.

## 7.2 Scope of future work

The following works can be taken up, to gain more insights into the mechanical and functional performance of the HEA coatings.

- The processing of HEA compositions including other refractory elements can be explored for their suitability in different engineering applications.
- The deposition of CoCrNiTiMo<sub>x</sub> and CoCrNiTiW<sub>x</sub> HEA coatings using other thermal spray techniques, specifically cold spray and plasma spray can be explored. Further the mechanical and tribological performance of the coatings can be thoroughly investigated and compared with the existing studies.
- Mechanical properties of the coatings including the scratch behaviour, young's modulus, Nano hardness of the coatings can be investigated further. Moreover, the residual stresses developed during the coating deposition is determined to understand their influence on the mechanical properties of the coatings.
- The suitability of CoCrNiTiMo<sub>x</sub> and CoCrNiTiW<sub>x</sub> HEA coatings in marine applications can be explored by studying their aqueous corrosion performance.
- The oxidation resistance of CoCrNiTiMo<sub>x</sub> and CoCrNiTiW<sub>x</sub> HEA coatings at elevated temperatures can be investigated to determine their suitability in different high temperature applications.
- Further, the HEA coatings investigated in the current study can be post processed using microwave fusing and other heat treatment techniques to enhance the mechanical and tribological performance.



## REFERENCES

- Alharthi, F. A., Alanazi, H. S., Alsyahi, A. A., i Ahmad, N. (2021). «Hydrothermal synthesis, characterization and exploration of photocatalytic activities of polyoxometalate: Ni-cowo4 nanoparticles». *Crystals*, 11(5).
- Aliyu, A., i Srivastava, C. (2019). «Microstructure and corrosion properties of MnCrFeCoNi high entropy alloy-graphene oxide composite coatings». *Materialia*, 5(November 2018), 100249.
- Aliyu, A., i Srivastava, C. (2021). «Corrosion behavior and protective film constitution of AlNiCoFeCu and AlCrNiCoFeCu high entropy alloy coatings». *Surfaces and Interfaces*, 27(June), 101481.
- Alvi, S., i Akhtar, F. (2019). «High temperature tribology of CuMoTaWV high entropy alloy». *Wear*, 426-427(September 2018), 412-419.
- Argade, G. R., Joshi, S. S., Ayyagari, A. V., Mukherjee, S., Mishra, R. S., i Dahotre, N. B. (2019). «Tribocorrosion performance of laser additively processed high-entropy alloy coatings on aluminum». *Appl. Phys. A Mater. Sci. Process.*, 125(4), 1-9.
- Atashin, S., Wen, J. Z., i Varin, R. A. (2015). «Investigation of milling energy input on structural variations of processed olivine powders for CO<sub>2</sub>sequestration». *J. Alloys Compd.*, 618, 555-561.
- Ayyagari, A., Barthelemy, C., Gwalani, B., Banerjee, R., Scharf, T. W., i Mukherjee, S. (2018). «Reciprocating sliding wear behavior of high entropy alloys in dry and marine environments». *Mater. Chem. Phys.*, 210, 162-169.
- babu, C. S., Sivaprasad, K., Muthupandi, V., i Szpunar, J. A. (2014). «Characterization of Nanocrystalline AlCoCrCuNiFeZn High Entropy Alloy Produced by Mechanical Alloying». *Procedia Mater. Sci.*, 5, 1020-1026.
- Bolelli, G., Colella, A., Lusvarghi, L., Puddu, P., Rigon, R., Sassatelli, P., i Testa, V. (2019). «Properties of HVOF-sprayed TiC-FeCrAl coatings». *Wear*, 418-419(November 2018), 36-51.

Bureš, R., Hadraba, H., Fáberová, M., Kollár, P., Fúzer, J., i Roupcová, P. (2017). «FeSiBAlNiMo High Entropy Alloy Prepared by Mechanical Alloying». 131(4), 771-773.

Cai, Z., Wang, Y., Cui, X., Jin, G., Li, Y., Liu, Z., i Dong, M. (2017). «Surface & Coatings Technology Design and microstructure characterization of FeCoNiAlCu high-entropy alloy coating by plasma cladding: In comparison with thermodynamic calculation». *Surf. Coat. Technol.*, 330(October), 163-169.

Cantor, B., Chang, I. T. H., Knight, P., i Vincent, A. J. B. (2004). «Microstructural development in equiatomic multicomponent alloys». *Mater. Sci. Eng. A*, 375-377(1-2 SPEC. ISS.), 213-218.

Chellasamy, V., i Thangadurai, P. (2017). «Structural and electrochemical investigations of nanostructured NiTiO<sub>3</sub> in acidic environment». 11(2), 162-170.

Chen, C. L., i Suprianto. (2020). «Microstructure and mechanical properties of AlCuNiFeCr high entropy alloy coatings by mechanical alloying». *Surf. Coatings Technol.*, 386(1), 125443.

Chen, J., Zhou, H., Zhao, X., Chen, J., An, Y., i Yan, F. (2015a). «Microstructural Characterization and Tribological Behavior of HVOF Sprayed NiMoAl Coating from 20 to 800 °C». *J. Therm. Spray Technol.*, 24(3), 348-356.

Chen, J., Zhou, X., Wang, W., Liu, B., Lv, Y., i Yang, W. (2018). «A review on fundamental of high entropy alloys with promising high e temperature properties». *J. Alloys Compd.*, 760, 15-30.

Chen, L., Bobzin, K., Zhou, Z., Zhao, L., Öte, M., Königstein, T., Tan, Z., i He, D. (2019a). «Wear behavior of HVOF-sprayed Al<sub>0.6</sub>TiCrFeCoNi high entropy alloy coatings at different temperatures». *Surf. Coatings Technol.*, 358(November 2018), 215-222.

Chen, L., Zhang, X., Wang, Y., Hao, X., i Liu, H. (2019b). «Microstructure and elastic constants of AlTiVMoNb refractory high- entropy alloy coating on Ti6Al4V by laser cladding Microstructure and elastic constants of AlTiVMoNb refractory high-entropy alloy coating on Ti6Al4V by laser cladding».

Chen, M., Lan, L., Shi, X., Yang, H., Zhang, M., i Qiao, J. (2019c). «The tribological properties of Al<sub>0.6</sub>CoCrFeNi high-entropy alloy with the  $\sigma$  phase precipitation at elevated temperature». *J. Alloys Compd.*, 777, 180-189.

Chen, Y. L., Hu, Y. H., Hsieh, C. A., Yeh, J. W., i Chen, S. K. (2009). «Competition between elements during mechanical alloying in an octonary multi-principal-element alloy system». *J. Alloys Compd.*, 481(1-2), 768-775.

Chen, Z., Chen, W., Wu, B., Cao, X., Liu, L., i Fu, Z. (2015b). «Materials Science & Engineering A Effects of Co and Ti on microstructure and mechanical behavior of Al 0.75 FeNiCrCo high entropy alloy prepared by mechanical alloying and spark plasma sintering». *Mater. Sci. Eng. A*, 648, 217-224.

Cheng, H., Fang, Y., Xu, J., Zhu, C., Dai, P., i Xue, S. (2020). «Tribological properties of nano/ultrafine-grained FeCoCrNiMnAl<sub>x</sub> high-entropy alloys over a wide range of temperatures». *J. Alloys Compd.*, 817, 153305.

Das, S., i Robi, P. S. (2021). «Processing and characterization of W<sub>23</sub>Mo<sub>23</sub>V<sub>17</sub>Cr<sub>8</sub>Ta<sub>7</sub>Fe<sub>22</sub> and WMoVCrTa refractory high entropy alloys». *Int. J. Refract. Met. Hard Mater.*, 100(July), 105656.

Díaz-Reyes, J., Castillo-Ojeda, R., Galván-Arellano, M., i Zaca-Moran, O. (2013). «Characterization of WO<sub>3</sub> thin films grown on silicon by HFMOD». *Adv. Condens. Matter Phys.*, 2013.

Dong, Y., Lu, Y., Jiang, L., Wang, T., i Li, T. (2014). «Effects of electro-negativity on the stability of topologically close-packed phase in high entropy alloys». *Intermetallics*, 52, 105-109.

Dwivedi, A., Koch, C. C., i Rajulapati, K. V. (2016). «On the single phase fcc solid solution in nanocrystalline Cr-Nb-Ti-V-Zn high-entropy alloy». *Mater. Lett.*, 183, 44-47.

Evans, A. G., i Wilshaw, T. R. (1976). «Quasi-static solid particle damage in brittle solids-I. Observations analysis and implications». *Acta Metall.*, 24(10), 939-956.

Fu, Y., Huang, C., Du, C., Li, J., Dai, C., Luo, H., i Liu, Z. (2021). «Evolution in

microstructure , wear , corrosion , and tribocorrosion behavior of Mo-containing high-entropy alloy coatings fabricated by laser cladding». 191(July).

Fu, Z., Chen, W., Wen, H., Zhang, D., Chen, Z., Zheng, B., Zhou, Y., i Lavernia, E. J. (2016). «Acta Materialia Microstructure and strengthening mechanisms in an FCC structured alloy». *Acta Mater.*, 107, 59-71.

Fu, Z., Chen, W., Xiao, H., Zhou, L., Zhu, D., i Yang, S. (2013). «Fabrication and properties of nanocrystalline Co<sub>0.5</sub>FeNiCrTi<sub>0.5</sub> high entropy alloy by MA-SPS technique». *Mater. Des.*, 44, 535-539.

Geng, Y., Chen, J., Tan, H., Cheng, J., Yang, J., i Liu, W. (2020). «Vacuum tribological behaviors of CoCrFeNi high entropy alloy at elevated temperatures». *Wear*, 456-457(December 2019), 203368.

Ghassemali, E., Sonkusare, R., Biswas, K., i Gurao, N. P. (2017). «In-situ study of crack initiation and propagation in a dual phase AlCoCrFeNi high entropy alloy». *J. Alloys Compd.*, 710, 539-546.

Gu, Z., Xi, S., Mao, P., i Wang, C. (2020). «Microstructure and wear behavior of mechanically alloyed powder Al<sub>x</sub>Mo<sub>0.5</sub>NbFeTiMn<sub>2</sub> high entropy alloy coating formed by laser cladding». *Surf. Coatings Technol.*, 401(August), 126244.

Guo, H., Wang, Y., Hao, E., Li, B., An, Y., Chen, J., Zhou, H., Yan, P., i Wu, Z. (2019). «CoMoCrSi coatings prepared by high-velocity oxygen fuel spraying: Microstructure and mechanical properties at elevated temperatures up to 800 °c». *Mater. Res. Express*, 6(12).

Guo, S. (2015). «Phase selection rules for cast high entropy alloys: An overview». *Mater. Sci. Technol. (United Kingdom)*, 31(10), 1223-1230.

Guo, S., i Liu, C. T. (2011). «Phase stability in high entropy alloys : Formation of solid-solution phase or amorphous phase».

Gupta, R., Srivastava, S., Kumar, N. K., i Panthi, S. K. (2016). «High leaded tin bronze processing during multi-directional forging: Effect on microstructure and mechanical properties». *Mater. Sci. Eng. A*, 654, 282-291.

- Harith, M., Sidik, I., Amir, N., i Kamal, S. (2018). «Wear Mechanism of Wear Resistant HVOF Thermal Spray Coating : Chromium Carbide Nickel Chrome on 304 AISI Steel». 06017.
- Hashem, A. M., Ghany, A. E. A., Indris, S., Ehrenberg, H., Mauger, A., i Julien, C. M. (2018). «Anatase TiO<sub>2</sub> nanoparticles for lithium-ion batteries». *Ionics (Kiel)*, 24, 2925–2934.
- Hou, L., Hui, J., Yao, Y., Chen, J., i Liu, J. (2019). «Effects of Boron Content on microstructure and mechanical properties of AlFeCoNiB<sub>x</sub> High Entropy Alloy Prepared by vacuum arc melting». *Vacuum*, 164(March), 212-218.
- Hsu, W. L., Yang, Y. C., Chen, C. Y., i Yeh, J. W. (2017a). «Thermal sprayed high-entropy NiCo<sub>0.6</sub>Fe<sub>0.2</sub>Cr<sub>1.5</sub>SiAlTi<sub>0.2</sub> coating with improved mechanical properties and oxidation resistance». *Intermetallics*, 89(June), 105-110.
- Hsu, W., Murakami, H., Yeh, J., Yeh, A., i Shimoda, K. (2017b). «Surface & Coatings Technology». *Surf. Coat. Technol.*, 316, 71-74.
- Huang, Y., Hu, Y., Zhang, M., Mao, C., Tong, Y., Zhang, J., Li, K., i Wang, K. (2022). «On the enhanced wear resistance of laser-clad CoCrCuFeNiTi<sub>x</sub> high-entropy alloy coatings at elevated temperature». *Tribol. Int.*, 174(June), 107767.
- Hung, S., Wang, C., Chen, Y., Lee, J., i Li, C. (2019). «Surface & Coatings Technology Thermal and corrosion properties of V-Nb-Mo-Ta-W and V-Nb-Mo-Ta-W-Cr- B high entropy alloy coatings». *Surf. Coat. Technol.*, 375(August), 802-809.
- Iliev, M. N. (2014). «The Raman spectra of Co<sub>3</sub>O<sub>4</sub>». (November 2000), 3-6.
- Jiang, Y. Q., Li, J., Juan, Y. F., Lu, Z. J., i Jia, W. L. (2019). «Evolution in microstructure and corrosion behavior of AlCoCr<sub>x</sub>FeNi high-entropy alloy coatings fabricated by laser cladding». *J. Alloys Compd.*, 775, 1-14.
- Jin, B., Zhang, N., Guan, S., Zhang, Y., i Li, D. (2018a). «Surface & Coatings Technology entropy alloy coatings ( b ) ( c )». 349(February), 867-873.
- Jin, B., Zhang, N., Guan, S., Zhang, Y., i Li, D. (2018b). «Microstructure and properties of laser re-melting FeCoCrNiAl<sub>0.5</sub>Si<sub>x</sub> high-entropy alloy coatings». *Surf. Coatings*

*Technol.*, 349(June), 867-873.

Jin, B., Zhang, N., Yu, H., Hao, D., i Ma, Y. (2020). «Al<sub>x</sub>CoCrFeNiSi high entropy alloy coatings with high microhardness and improved wear resistance». *Surf. Coatings Technol.*, 402(August), 126328.

Jin, C., Li, X., Li, H., Li, Q., i Wang, H. (2022). «Tribological performance of a TiZrNbMo<sub>0.6</sub> refractory high entropy alloy at elevated temperatures». *J. Alloys Compd.*, 920, 165915.

José, F., Antão, N., Coelho Da, R. M., Doctor, S., Rosado, M. S., Dias, S., Emília, M., Rosa, E., i Dias, S. (2019). «HEAs: High Entropy Alloys for advanced systems and engines». (April).

Joseph, J., Haghdadi, N., Annasamy, M., Kada, S., Hodgson, P. D., Barnett, M. R., i Fabijanic, D. M. (2020). «On the enhanced wear resistance of CoCrFeMnNi high entropy alloy at intermediate temperature». *Scr. Mater.*, 186, 230-235.

Joseph, J., Haghdadi, N., Shamlaye, K., Hodgson, P., Barnett, M., i Fabijanic, D. (2019). «The sliding wear behaviour of CoCrFeMnNi and Al<sub>x</sub>CoCrFeNi high entropy alloys at elevated temperatures». *Wear*, 428-429(November 2018), 32-44.

Kang, B., Lee, J., Jin, H., i Hyung, S. (2018). «Materials Science & Engineering A Ultra-high strength WNbMoTaV high-entropy alloys with fine grain structure fabricated by powder metallurgical process». *Mater. Sci. Eng. A*, 712(December 2017), 616-624.

Kim, H., Nam, S., Roh, A., Son, M., Ham, M. H., Kim, J. H., i Choi, H. (2019). «Mechanical and electrical properties of NbMoTaW refractory high-entropy alloy thin films». *Int. J. Refract. Met. Hard Mater.*, 80(January), 286-291.

Koch, C. C. (2017). «Nanocrystalline high-entropy alloys». 3435-3444.

Kumar, A., Dhekne, P., Swarnakar, A. K., i Chopkar, M. (2019). «Phase evolution of CoCrCuFeNiSi<sub>x</sub> high-entropy alloys prepared by mechanical alloying and spark plasma sintering Phase evolution of CoCrCuFeNiSi<sub>x</sub> high-entropy alloys prepared by mechanical alloying and spark plasma sintering».

Kuptsov, K. A., Antonyuk, M. N., Sheveyko, A. N., Bondarev, A. V., Ignatov, S. G., Slukin, P. V., Dwivedi, P., Fraile, A., Polcar, T., i Shtansky, D. V. (2023). «High-entropy Fe-Cr-Ni-Co-(Cu) coatings produced by vacuum electro-spark deposition for marine and coastal applications». *Surf. Coatings Technol.*, 453(September 2022), 129136.

Lee, C., Chou, Y., Kim, G., Gao, M. C., An, K., Brechtel, J., Zhang, C., Chen, W., Poplawsky, J. D., Song, G., Ren, Y., Chou, Y. C., i Liaw, P. K. (2020). «Lattice-Distortion-Enhanced Yield Strength in a Refractory High-Entropy Alloy». *Adv. Mater.*, 32(49), 1-9.

Lekatou, A. G., Sioulas, D., i Grimanelis, D. (2023). «Corrosion and wear of coatings fabricated by HVOF-spraying of nanostructured and conventional WC–10Co–4Cr powders on Al7075-T6». *Int. J. Refract. Met. Hard Mater.*, 112(October 2022), 106164.

Li, K., Liang, J., i Zhou, J. (2022). «Microstructure and elevated temperature tribological performance of the CoCrFeNiMo high entropy alloy coatings». *Surf. Coatings Technol.*, 449(October), 128978.

Li, T., Liu, Y., Liu, B., Guo, W., i Xu, L. (2017). «Microstructure and wear behavior of FeCoCrNiMo<sub>0.2</sub> high entropy coatings prepared by air plasma spray and the high velocity oxy-fuel spray processes». *Coatings*, 7(9), 5-8.

Li, X., Wei, D., Vitos, L., i Lizárraga, R. (2020). «Micro-mechanical properties of new alternative binders for cemented carbides: CoCrFeNiW<sub>x</sub> high-entropy alloys». *J. Alloys Compd.*, 820, 0-7.

Li, Y., i Shi, Y. (2021). «Microhardness, wear resistance, and corrosion resistance of Al<sub>x</sub>CrFeCoNiCu high-entropy alloy coatings on aluminum by laser cladding». *Opt. Laser Technol.*, 134(7089), 106632.

Liang, H., Miao, J., Gao, B., Deng, D., Wang, T., Lu, Y., Cao, Z., Jiang, H., Li, T., i Kang, H. (2020). «Microstructure and tribological properties of AlCrFe<sub>2</sub>Ni<sub>2</sub>W<sub>0.2</sub>Mo<sub>0.75</sub> high-entropy alloy coating prepared by laser cladding in seawater, NaCl solution and deionized water». *Surf. Coatings Technol.*, 400(July),

126214.

Liang, H., Qiao, D., Miao, J., Cao, Z., Jiang, H., i Wang, T. (2021). «Anomalous microstructure and tribological evaluation of AlCrFeNiW0.2Ti0.5 high-entropy alloy coating manufactured by laser cladding in seawater». *J. Mater. Sci. Technol.*, 85, 224-234.

Liao, L., Gao, R., Yang, Z. H., Wu, S. T., i Wan, Q. (2022). «A study on the wear and corrosion resistance of high-entropy alloy treated with laser shock peening and PVD coating». *Surf. Coatings Technol.*, 437(December 2021).

Lima, N. A., Alencar, L. D. S., Siu-li, M., Carlos, A. C., Mesquita, A., Peko, J. M., i Bernardi, M. I. B. (2020). «NiWO<sub>4</sub> powders prepared via polymeric precursor method for application as ceramic luminescent pigments». 9(1), 55-63.

Lin, J., Wang, Z., Lin, P., Cheng, J., Zhang, X., i Hong, S. (2015). «Effects of post annealing on the microstructure, mechanical properties and cavitation erosion behavior of arc-sprayed FeNiCrBSiNbW coatings». *Mater. Des.*, 65, 1035-1040.

Liu, H., Gao, Q., Dai, J., Chen, P., Gao, W., Hao, J., i Yang, H. (2022a). «Microstructure and high-temperature wear behavior of CoCrFeNiW<sub>x</sub> high-entropy alloy coatings fabricated by laser cladding». *Tribol. Int.*, 172(April), 107574.

Liu, H., Sun, S., Zhang, T., Zhang, G., Yang, H., i Hao, J. (2021). «Effect of Si addition on microstructure and wear behavior of AlCoCrFeNi high-entropy alloy coatings prepared by laser cladding». *Surf. Coatings Technol.*, 405(October 2020), 126522.

Liu, W. H., Lu, Z. P., He, J. Y., Luan, J. H., Wang, Z. J., Liu, B., Liu, Y., Chen, M. W., i Liu, C. T. (2016). «Ductile CoCrFeNiMox high entropy alloys strengthened by hard intermetallic phases». *Acta Mater.*, 116, 332-342.

Liu, X., Lv, F., Li, H., Wang, Y., Lu, X., i Zhao, D. (2022b). «Microstructure and High-Temperature Tribological Behavior of Plasma-Sprayed FeCoCrAlNi High Entropy Alloy Coatings Under Higher Load Condition». *J. Therm. Spray Technol.*, 31(4), 1276-1284.

Lizárraga, R., Holmström, E., i Vitos, L. (2018). «Alloying effect of tungsten on the

structural and magnetic properties of CoCrFeNiW high entropy alloys». *Phys. Rev. Mater.*, 2(9), 1-7.

Löbel, M., Lindner, T., i Lampke, T. (2020). «High-temperature wear behaviour of AlCoCrFeNiTi<sub>0.5</sub> coatings produced by HVOF». *Surf. Coatings Technol.*, 403(August), 126379.

Löbel, M., Lindner, T., Mehner, T., i Lampke, T. (2017). «Microstructure and wear resistance of AlCoCrFeNiTi high-entropy alloy coatings produced by HVOF». *Coatings*, 7(9).

Löbel, M., Lindner, T., Mehner, T., Rymer, L.-M., Björklund, S., Joshi, S., i Lampke, T. (2021). «Microstructure and Corrosion Properties of AlCrFeCoNi High-Entropy Alloy Coatings Prepared by HVAF and HVOF». *J. Therm. Spray Technol.*

Ma, S. G., i Zhang, Y. (2012). «Effect of Nb addition on the microstructure and properties of AlCoCrFeNi high-entropy alloy». *Mater. Sci. Eng. A*, 532, 480-486.

Mahade, S., Awe, S. A., Björklund, S., Lukáč, F., Mušálek, R., i Joshi, S. (2022). «Sliding wear behavior of a sustainable Fe-based coating and its damage mechanisms». *Wear*, 500-501(April).

Maulik, O., i Kumar, V. (2015). «Materials Characterization». *Mater. Charact.*, 110, 116-125.

Medabalimi, S. R., Ramesh, M. R., i Kadoli, R. (2021). «Developing partially oxidized NiCr coatings using the combined flame spray and plasma spray process for improved wear behaviour at high temperature». *Wear*, 478-479(March), 203885.

Meghwal, A., Anupam, A., Murty, B. S., i Berndt, C. C. (2020). *Thermal Spray High-Entropy Alloy Coatings : A Review. J. Therm. Spray Technol.*, Springer US.

Meghwal, A., Anupam, A., Schulz, C., Hall, C., Murty, B. S., Kottada, R. S., Vijay, R., Munroe, P., Berndt, C. C., i Ang, A. S. M. (2022). «Tribological and corrosion performance of an atmospheric plasma sprayed AlCoCr<sub>0.5</sub>Ni high-entropy alloy coating». *Wear*, 506-507(March), 204443.

Miao, J., Liang, H., Zhang, A., He, J., Meng, J., i Lu, Y. (2021). «Tribological behavior

of an AlCoCrFeNi<sub>2.1</sub> eutectic high entropy alloy sliding against different counterfaces». *Tribol. Int.*, 153(August 2020), 106599.

Mohanty, S., Maity, T. N., Mukhopadhyay, S., Sarkar, S., Gurao, N. P., Bhowmick, S., i Biswas, K. (2017). «Powder metallurgical processing of equiatomic AlCoCrFeNi high entropy alloy: Microstructure and mechanical properties». *Mater. Sci. Eng. A*, 679(September 2016), 299-313.

Moravcik, I., Cizek, J., Gavendova, P., Sheikh, S., Guo, S., i Dlouhy, I. (2016). «Effect of heat treatment on microstructure and mechanical properties of spark plasma sintered AlCoCrFeNiTi<sub>0.5</sub> high entropy alloy». *Mater. Lett.*, 174, 53-56.

Mridha, S., Samal, S., Khan, P. Y., i Biswas, K. (2013). «Processing and Consolidation of Nanocrystalline Cu-Zn-Ti-Fe-Cr High-Entropy Alloys via Mechanical Alloying».

Muangtong, P., Rodchanarowan, A., Chaysuwan, D., Chanlek, N., i Goodall, R. (2020). «The corrosion behaviour of CoCrFeNi-x (x = Cu, Al, Sn) high entropy alloy systems in chloride solution». *Corros. Sci.*, 172(October 2019), 108740.

Murali, M., Babu, S. P. K., Krishna, B. J., i Vallimanalan, A. (2016). «Synthesis and characterization of AlCoCrCuFeZn<sub>x</sub> high-entropy alloy by mechanical alloying». *Prog. Nat. Sci. Mater. Int.*, 26(4), 380-384.

Nagy, P., Rohbeck, N., Roussely, G., Sortais, P., Lábár, J. L., Gubicza, J., Michler, J., i Pethő, L. (2020). «Processing and characterization of a multibeam sputtered nanocrystalline CoCrFeNi high-entropy alloy film». *Surf. Coatings Technol.*, 386(July 2019), 125465.

Nair, R. B., Ngan, S., i McDonald, A. (2023). «Dry abrasive wear and solid particle erosion assessments of high entropy alloy coatings fabricated by cold spraying». *Mater. Today Commun.*, 34(January).

Naser-zoshki, H., i Vahdati-khaki, J. (2020). «Design of a low density refractory high entropy alloy in non-equiatomic W–Mo–Cr–Ti–Al system». *Vacuum*, 109614.

Ndumia, J. N., Kang, M., Gbenontin, B. V., Lin, J., Liu, J., i Nyambura, S. M. (2023). «Evaluation of thermal shock failure mechanism of arc-sprayed Fe-based coatings

- deposited on different substrates». *Surf. Coatings Technol.*, 474(October), 130081.
- Nguyen, C., Tieu, A. K., Deng, G., Wexler, D., Vo, T. D., Wang, L., i Yang, J. (2022). «Tribological performance of a cost-effective CrFeNiAl<sub>0.3</sub>Ti<sub>0.3</sub> high entropy alloy based self-lubricating composite in a wide temperature range». *Tribol. Int.*, 174(April), 107743.
- Niu, Z., Xu, J., Wang, T., Wang, N., Han, Z., i Wang, Y. (2019). «Microstructure, mechanical properties and corrosion resistance of CoCrFeNiW<sub>x</sub> (x = 0, 0.2, 0.5) high entropy alloys». *Intermetallics*, 112(April), 106550.
- Obeydavi, A., Shafyei, A., Rezaeian, A., Kameli, P., i Lee, J. (2020). «Microstructure , mechanical properties and corrosion performance of Fe<sub>44</sub>Cr<sub>15</sub>Mo<sub>14</sub>Co<sub>7</sub>C<sub>10</sub>B<sub>5</sub>Si<sub>5</sub> thin film metallic glass deposited by DC magnetron sputtering». *J. Non. Cryst. Solids*, 527(November 2019), 119718.
- Pal, S., Nair, R. B., i McDonald, A. (2023). «Effect of tungsten and vanadium additions on the dry abrasive wear and solid particle erosion of flame-sprayed AlCoCrFeMo high entropy alloy coatings». *Int. J. Refract. Met. Hard Mater.*, 114(November 2022).
- Parthasarathi, N. L., i Duraiselvam, M. (2010). «High temperature tribological properties of NiCrBSiCFe plasma-sprayed coating on austenitic stainless steel substrate». *J. Alloys Compd.*, 505(2), 824-831.
- Patel, P., Alidokht, S. A., Sharifi, N., Roy, A., Harrington, K., Stoyanov, P., Chromik, R. R., i Moreau, C. (2022). «Microstructural and Tribological Behavior of Thermal Spray CrMnFeCoNi High Entropy Alloy Coatings». *J. Therm. Spray Technol.*, 31(4), 1285-1301.
- Pole, M., Sadeghilaridjani, M., Shittu, J., Ayyagari, A., i Mukherjee, S. (2020). «High temperature wear behavior of refractory high entropy alloys based on 4-5-6 elemental palette». *J. Alloys Compd.*, 843, 156004.
- Pouliat, A., Georgatis, E., Lekatou, A., i Karantzalis, A. (2017). «Dry-Sliding Wear Response of MoTaWNbV High Entropy Alloy». *Adv. Eng. Mater.*, 19(2), 1-10.
- Prasad, C. D., Joladarashi, S., Ramesh, M. R., Srinath, M. S., i Channabasappa, B. H.

(2019). «Effect of microwave heating on microstructure and elevated temperature adhesive wear behavior of HVOF deposited CoMoCrSi-Cr<sub>3</sub>C<sub>2</sub> coating». *Surf. Coatings Technol.*, 374(April 2018), 291-304.

Purushotham, N., Santhy, K., Suresh Babu, P., Sivakumar, G., i Rajasekaran, B. (2023). «In Situ High-Temperature X-ray Diffraction Study on Atmospheric Plasma and Detonation Sprayed Ni-5 wt.%Al Coatings». *J. Therm. Spray Technol.*

Qin, G., Xue, W., Fan, C., Chen, R., Wang, L., Su, Y., Ding, H., i Guo, J. (2018). «Materials Science & Engineering A Effect of Co content on phase formation and mechanical properties of ( AlCoCrFeNi ) 100- x Co x high-entropy alloys». *Mater. Sci. Eng. A*, 710(October 2017), 200-205.

Qiu, J., Nguyen, T. H., Kim, S., Lee, Y. J., Song, M. T., Huang, W. J., Chen, X. B., Nguyen, T. M. H., i Yang, I. S. (2022). «Two-dimensional correlation spectroscopy analysis of Raman spectra of NiO nanoparticles». *Spectrochim. Acta - Part A Mol. Biomol. Spectrosc.*, 280(March), 121498.

Qiu, X. (2020). «Microstructure and mechanical properties of CoCrFeNiMo high-entropy alloy coatings». *J. Mater. Res. Technol.*, 9(3), 5127-5133.

Rogal, Ł., Szklarz, Z., Bobrowski, P., Kalita, D., Garzeł, G., i Tarasek, A. (2019). «Microstructure and Mechanical Properties of Al – Co – Cr – Fe – Ni Base High Entropy Alloys Obtained Using Powder Metallurgy». *Met. Mater. Int.*, 25(4), 930-945.

Roy, A., Sreeramagiri, P., Babuska, T., Krick, B., Ray, P. K., i Balasubramanian, G. (2021). «Lattice distortion as an estimator of solid solution strengthening in high-entropy alloys». *Mater. Charact.*, 172(January), 110877.

Salemi, F., Abbasi, M. H., i Karimzadeh, F. (2016). «Synthesis and thermodynamic analysis of nanostructured CuNiCoZnAl high entropy alloy produced by mechanical alloying». *J. Alloys Compd.*, 685, 278-286.

Sathiaraj, G. D., i Bhattacharjee, P. P. (2015). «Effect of starting grain size on the evolution of microstructure and texture during thermo-mechanical processing of CoCrFeMnNi high entropy alloy». *J. Alloys Compd.*, 647, 82-96.

- Senkov, O. N., Wilks, G. B., Scott, J. M., i Miracle, D. B. (2011). «Intermetallics Mechanical properties of Nb 25 Mo 25 Ta 25 W 25 and V 20 Nb 20 Mo 20 Ta 20 W 20 refractory high entropy alloys». *Intermetallics*, 19(5), 698-706.
- Sethi, A., Byrum, T., McAuliffe, R. D., Gleason, S. L., Slimak, J. E., Shoemaker, D. P., i Cooper, S. L. (2017). «Magnons and magnetodielectric effects in CoCr<sub>2</sub>O<sub>4</sub>: Raman scattering studies». *Phys. Rev. B*, 95(17), 1-9.
- Sha, M., Jia, C., Qiao, J., Feng, W., Ai, X., i Jing, Y. (2019). «Microstructure and Properties of High-Entropy Al».
- Shivam, V. (2020). «Phase Evolution and Thermal Stability of Mechanically Alloyed AlCrFeCoNiZn High-Entropy Alloy». *Trans. Indian Inst. Met.*, 73(3), 821-830.
- Shivam, V., Shadangi, Y., Basu, J., i Mukhopadhyay, N. K. (2019). «Alloying behavior and thermal stability of mechanically alloyed nano AlCoCrFeNiTi high-entropy alloy». *J. Mater. Res.*, 34(5), 787-795.
- Shivam, V., Shadangi, Y., Basu, J., i Mukhopadhyay, N. K. (2020). «Evolution of phases , hardness and magnetic properties of AlCoCrFeNi high entropy alloy processed by mechanical alloying». *J. Alloys Compd.*, 832, 154826.
- Shun, T. T., Chang, L. Y., i Shiu, M. H. (2012). «Microstructures and mechanical properties of multiprincipal component CoCrFeNiTi<sub>x</sub> alloys». *Mater. Sci. Eng. A*, 556, 170-174.
- Siao, A., Ang, M., Berndt, C. C., Sesso, M., i Anupam, A. (2015). «Comparison of Plasma Sprayed High Entropy Alloys with Conventional Bond Coat Materials Comparison of Plasma Sprayed High Entropy Alloys with Conventional Bond Coat Materials». (May).
- Singh, G., Kaur, M., i Upadhyaya, R. (2019). «Wear and Friction Behavior of NiCrBSi Coatings at Elevated Temperatures». *J. Therm. Spray Technol.*, 28(5), 1081-1102.
- Sriharitha, R., Murty, B. S., i Kottada, R. S. (2013). «Phase formation in mechanically alloyed Al<sub>x</sub>CoCrCuFeNi (x = 0.45, 1, 2.5, 5 mol) high entropy alloys». *Intermetallics*, 32, 119-126.

Srivastava, M., Jadhav, M., Chethan, Chakradhar, R. P. S., Muniprakash, M., i Singh, S. (2019). «Synthesis and properties of high velocity oxy-fuel sprayed FeCoCrNi2Al high entropy alloy coating». *Surf. Coatings Technol.*, 378(June), 124950.

Suprianto, i Chen, C. L. (2023). «Study of Cu Effect and In-situ Yttria Dispersoids on Microstructure Evolution of Mechanically Alloyed CoFeNiCrCu High Entropy Alloys». *Met. Mater. Int.*, 29(2), 420-428.

Suryanarayana, C. (2001). «Mechanical alloying and milling». 46.

Suryanarayana, C. (2019). «Mechanical Alloying: A Novel Technique to Synthesize Advanced Materials». *Research*, 2019(May), 1-17.

Suryanarayana, C., Ivanov, E., i Boldyrev, V. V. (2001). «The science and technology of mechanical alloying». 306, 151-158.

Takeuchi, A., i Inoue, A. (2005). «Classification of Bulk Metallic Glasses by Atomic Size Difference , Heat of Mixing and Period of Constituent Elements and Its Application to Characterization of the Main Alloying Element». 46(12).

Thürlová, H., i Průša, F. (2022). «Influence of the Al Content on the Properties of Mechanically Alloyed CoCrFeNiMnXAl<sub>20-X</sub> High-Entropy Alloys». *Materials (Basel)*, 15(22).

Tian, L. (2016). «Microstructure and Wear Behavior of Atmospheric Plasma-Sprayed AlCoCrFeNiTi High-Entropy Alloy Coating». *J. Mater. Eng. Perform.*, 25(12), 5513-5521.

Tian, L., Fu, M., i Xiong, W. (2018). «Microstructural Evolution of AlCoCrFeNiSi High-Entropy Alloy Powder during Mechanical».

Tian, L., Wang, J., Zhang, Q., Li, R., i Liu, C. (2019a). «Microstructure characterization of AlCoCrFeNiTi high-entropy alloy coating produced by atmospheric plasma spraying  
Microstructure characterization of AlCoCrFeNiTi high-entropy alloy coating produced by atmospheric plasma spraying». *Mater. Res. Express*, 6(11), 116416.

Tian, L., Wang, J., Zhang, Q., Li, R., i Liu, C. (2019b). «Microstructure characterization of AlCoCrFeNiTi high-entropy alloy coating produced by atmospheric plasma spraying

Microstructure characterization of AlCoCrFeNiTi high-entropy alloy coating produced by atmospheric plasma spraying».

Tsai, M. H., i Yeh, J. W. (2014). «High-entropy alloys: A critical review». *Mater. Res. Lett.*, 2(3), 107-123.

Tsai, M., Yeh, J., Tsai, M., i Yeh, J. (2014). «High-Entropy Alloys : A Critical Review High-Entropy Alloys : A Critical Review». 3831.

Tüten, N., Canadinc, D., Motallebzadeh, A., i Bal, B. (2019). «Intermetallics Microstructure and tribological properties of TiTaHfNbZr high entropy alloy coatings deposited on Ti e 6Al e 4V substrates». *Intermetallics*, 105(November 2018), 99-106.

Ustinov, A. I., Demchenkov, S. A., Melnychenko, T. V., Skorodzievskii, V. S., i Polishchuk, S. S. (2021). «Effect of structure of high entropy CrFeCoNiCu alloys produced by EB PVD on their strength and dissipative properties». *J. Alloys Compd.*, 887, 161408.

Vaidya, M., Prasad, A., Parakh, A., i Murty, B. S. (2017). «Materials & Design In fl uence of sequence of elemental addition on phase evolution in nanocrystalline AlCoCrFeNi : Novel approach to alloy synthesis using mechanical alloying». *Mater. Des.*, 126(January), 37-46.

Vallimanalan, A., Babu, S. P. K., Muthukumaran, S., Murali, M., Gaurav, V., i Mahendran, R. (2019a). «Materials Today: Proceedings Corrosion behaviour of thermally sprayed Mo added AlCoCrNi high entropy alloy coating». *Mater. Today Proc.*, (xxxx), 9-11.

Vallimanalan, A., Babu, S. P. K., Muthukumaran, S., Murali, M., Mahendran, R., Gaurav, V., i Manivannan, S. (2019b). «Synthesis , characterisation and erosion behaviour of AlCoCrMoNi high entropy alloy coating Synthesis , characterisation and erosion behaviour of AlCoCrMoNi high entropy alloy coating».

Varalakshmi, S., Kamaraj, M., i Murty, B. S. (2008). «Synthesis and characterization of nanocrystalline AlFeTiCrZnCu high entropy solid solution by mechanical alloying». 460, 253-257.

Wang, C., Ji, W., i Fu, Z. (2014a). «Mechanical alloying and spark plasma sintering of CoCrFeNiMnAl high-entropy alloy». *Adv. Powder Technol.*, 25(4), 1334-1338.

Wang, G., Liu, Q., Yang, J., Li, X., Sui, X., Gu, Y., i Liu, Y. (2019). «Synthesis and thermal stability of a nanocrystalline MoNbTaTiV refractory high-entropy alloy via mechanical alloying». *Int. J. Refract. Met. Hard Mater.*, 84(June), 104988.

Wang, W., Qi, W., Xie, L., Yang, X., Li, J., i Zhang, Y. (s.d.). «Microstructure and Corrosion Behavior of (CoCrFeNi)<sub>95</sub>Nb<sub>5</sub> High-Entropy Alloy Coating Fabricated by Plasma Spraying».

Wang, W. R., Wang, W. L., i Yeh, J. W. (2014b). «Phases, microstructure and mechanical properties of Al<sub>x</sub>CoCrFeNi high-entropy alloys at elevated temperatures». *J. Alloys Compd.*, 589, 143-152.

Wang, Z., Saxena, S. K., Lazor, P., i O'Neill, H. S. C. (2003). «An in situ Raman spectroscopic study of pressure induced dissociation of spinel NiCr<sub>2</sub>O<sub>4</sub>». *J. Phys. Chem. Solids*, 64(3), 425-431.

Wu, J. M., Lin, S. J., Yeh, J. W., Chen, S. K., Huang, Y. S., i Chen, H. C. (2006). «Adhesive wear behavior of Al<sub>x</sub>CoCrCuFeNi high-entropy alloys as a function of aluminum content». *Wear*, 261(5-6), 513-519.

Xiao, J. K., Tan, H., Wu, Y. Q., Chen, J., i Zhang, C. (2020a). «Microstructure and wear behavior of FeCoNiCrMn high entropy alloy coating deposited by plasma spraying». *Surf. Coatings Technol.*, 385(October 2019), 125430.

Xiao, J. K., Wu, Y. Q., Chen, J., i Zhang, C. (2020b). «Microstructure and tribological properties of plasma sprayed FeCoNiCrSiAl<sub>x</sub> high entropy alloy coatings». *Wear*, 448-449(January).

Xiao, J., Tan, H., Wu, Y., Chen, J., i Zhang, C. (2020c). «Surface & Coatings Technology Microstructure and wear behavior of FeCoNiCrMn high entropy alloy coating deposited by plasma spraying». *Surf. Coat. Technol.*, 385(October 2019), 125430.

Xu, J., Gu, S., Fan, L., Xu, P., i Lu, B. (2016). «Electrospun Lotus Root-like

CoMoO<sub>4</sub>@Graphene Nanofibers as High-Performance Anode for Lithium Ion Batteries». *Electrochim. Acta*, 196, 125-130.

Xu, J., Peng, S., Li, Z., Jiang, S., Xie, Z. H., Munroe, P., i Lu, H. (2021). «Remarkable cavitation erosion–corrosion resistance of CoCrFeNiTiMo high-entropy alloy coatings». *Corros. Sci.*, 190(June), 109663.

Yang, X., i Zhang, Y. (2012). «Prediction of high-entropy stabilized solid-solution in multi-component alloys». *Mater. Chem. Phys.*, 132(2-3), 233-238.

Yang, Y., Ren, Y., Tian, Y., Li, K., Bai, L., Huang, Q., Shan, Q., Tian, Y., i Wu, H. (2022). «Microstructure and tribological behaviors of FeCoCrNiMoSix high-entropy alloy coatings prepared by laser cladding». *Surf. Coatings Technol.*, 432(December 2021), 128009.

Yin, S., Li, W., Song, B., Yan, X., Kuang, M., Xu, Y., Wen, K., i Lupoi, R. (2019). «Deposition of FeCoNiCrMn high entropy alloy (HEA) coating via cold spraying». *J. Mater. Sci. Technol.*, 35(6), 1003-1007.

You, X., Song, J., Lin, P., Zhang, X., Su, Y., Wang, H., Zhang, Y., i Hu, L. (2022). «Tribological properties and wear mechanisms of Ti<sub>x</sub>VNbTaW<sub>y</sub> RHEAs sliding against Si<sub>3</sub>N<sub>4</sub> ceramic balls: The effects of Ti and W contents». *Tribol. Int.*, 175(May), 107801.

Yu, W., Wang, Y., i Li, R. (2019a). «Property of AlCoCrFeNiTi High-Entropy Alloy Coatings Prepared by Mechanical Alloying and Laser Cladding».

Yu, Y., He, F., Qiao, Z., Wang, Z., Liu, W., i Yang, J. (2019b). «Effects of temperature and microstructure on the tribological properties of CoCrFeNiNbx eutectic high entropy alloys». *J. Alloys Compd.*, 775, 1376-1385.

Yurkova, D. V. H. A. I., i Bilyk, V. V. C. I. I. (2020). «Nanostructured AlNiCoFeCrTi high - entropy coating performed by cold spray». *Appl. Nanosci.*, (0123456789).

Zhang, A., Han, J., Meng, J., Su, B., i Li, P. (2016). «Rapid preparation of AlCoCrFeNi high entropy alloy by spark plasma sintering from elemental powder mixture». 181, 82-85.

Zhang, H. F., Yan, H. L., Yu, H., Ji, Z. W., Hu, Q. M., i Jia, N. (2020). «The effect of Co and Cr substitutions for Ni on mechanical properties and plastic deformation mechanism of FeMnCoCrNi high entropy alloys». *J. Mater. Sci. Technol.*, 48, 146-155.

Zhang, M., Zhou, X., Yu, X., i Li, J. (2017). «Synthesis and characterization of refractory TiZrNbWMo high-entropy alloy coating by laser cladding». *Surf. Coatings Technol.*, 311, 321-329.

Zhang, Y., Han, T., Xiao, M., i Shen, Y. (2019). «Optik E ff ect of Nb content on microstructure and properties of laser». 198(August).

Zhang, Y., Ting, T., Tang, Z., Gao, M. C., Dahmen, K. A., Liaw, P. K., i Ping, Z. (2014). «Progress in Materials Science Microstructures and properties of high-entropy alloys». *Prog. Mater. Sci.*, 61(October 2013), 1-93.

Zhang, Y., Zhou, Y. J., Lin, J. P., Chen, G. L., i Liaw, P. K. (2008). «Solid-solution phase formation rules for multi-component alloys». *Adv. Eng. Mater.*, 10(6), 534-538.

Zhou, Y. kuan, Kang, J. jie, Zhang, J., Zhu, S., Fu, Z. qiang, Zhu, L. na, i She, D. shun. (2022). «Effect of nitriding on microstructure and wear behavior of HVOF sprayed Al<sub>x</sub>CoCrFeNi (x= 0.4, 0.7, 1.0) high-entropy alloy coatings». *Intermetallics*, 151(September), 107709.

Zois, D., Lekatou, A., i Vardavoulias, M. (2009). «A microstructure and mechanical property investigation on thermally sprayed nanostructured ceramic coatings before and after a sintering treatment». *Surf. Coatings Technol.*, 204(1-2), 15-27.

## LIST OF PUBLICATIONS

	<b>Title of the paper</b>	<b>Authors (in the same order as in the paper. Underline the Research Scholar's name)</b>	<b>Name of the Journal/ Conference, Vol., No., Pages</b>	<b>Month, Year of Publication</b>	<b>Category</b>
1	Effect of Mechanical Alloying on the Microstructure of CoCrNiTiMo <sub>x</sub> High Entropy Alloy.	<u>Addepalli S.N.</u> , Joladarashi, S, Ramesh, M.R, S B Arya	Journal of Thermal Spray Technology, Volume 31, 1045–1055. <a href="https://doi.org/10.1007/s11666-021-01317-5">https://doi.org/10.1007/s11666-021-01317-5</a> (SCI Indexed)	January 2022	1
2	Phase Evolution and High-Temperature Wear Behavior of Non-equiatomc Metastable CoCrNiTiMo <sub>x</sub> HEA Coatings Fabricated by High-Velocity Oxy-Fuel Technique.	<u>Addepalli S.N.</u> , Joladarashi, S, Ramesh, M.R	Materials Today Communications Volume 35, 106310. <a href="https://doi.org/10.1016/j.mtcomm.2023.106310">https://doi.org/10.1016/j.mtcomm.2023.106310</a> (SCIE Indexed)	June 2023	1
3	Elevated temperature tribological performance of non-equiatomc CoCrNiTiW <sub>x</sub> high entropy alloy coatings developed by mechanical alloying and high-velocity oxy-fuel spray.	<u>Addepalli S.N.</u> , Joladarashi, S, Ramesh, M.R	Surface & Coatings Technology, Volume 476, 130267. <a href="https://doi.org/10.1016/j.surfcoat.2023.130267">https://doi.org/10.1016/j.surfcoat.2023.130267</a> (SCI Indexed)	December 2023	1
4	Microstructure, mechanical and high-temperature dry sliding wear performance of CoCrNiTiMo and CoCrNiTiW high entropy alloy coatings	<u>Addepalli S.N.</u> , <u>Joladarashi, S, Ramesh, M.R</u>	Materials Chemistry and Physics (SCI Indexed)	Under review	1

**Category\*.** 1. Journal paper, full paper reviewed 2. Journal paper, Abstract reviews  
3. Conference/Symposium paper, full paper reviewed 4. Conference/Symposium paper, abstract reviewed  
5. Others (including papers in Workshops, NITK Research Bulletins, Short notes etc.)

## **BIO-DATA**

- 1 **Name** . Syam Narayana Addepalli
- 2 **Fathers Name** . Venkata Shesha Charyulu
- 3 **Date of Birth** . 6<sup>th</sup> June 1993
- 4 **Nationality** . Indian
- 5 **Marital status** . Single
- 6 **Address** . Plot no 40/P, Crystal township,  
Shankarpally, Ranga reddy, 575 025  
Karnataka, India.
- 7 **Mobile number** . 9966599633
- 8 **Email id** . [syamprakash.199@gmail.com](mailto:syamprakash.199@gmail.com)
- 9 **Educational qualifications**

<b>Qualification</b>	<b>University/Board</b>	<b>Year of passing</b>
Ph.D. (Mechanical Engineering)	National Institute of Technology Karnataka	2023
M.Tech(Industrial design)	National Institute of Technology Rourkela	2016
B.Tech (Mechanical Engineering)	Jawaharlal Nehru Technological University Hyderabad	2014